UNIVERSITA' DI TORINO

DIPARTIMENTO DI CHIMICA

DOTTORATO DI RICERCA IN SCIENZE CHIMICHE E DEI MATERIALI

CICLO: 37°

TITOLO DELLA TESI: INNOVATIVE STRATEGIES FOR THE ENGINEERING OF SENSORS FOR SUSTAINABLE FOOD SYSTEMS

TESI PRESENTATA DA: TAYYABA NOOR

SUPERVISORE: PROF. PAOLA RIZZI

COORDINATORE DEL DOTTORATO: PROF. BARTOLOMEO CIVALLERI

ANNI ACCADEMICI: 3°

SETTORE SCIENTIFICO-DISCIPLINARE DI AFFERENZA*: IMAT-01/A - Scienza e tecnologia dei materiali

(*N.B. Nel caso di più settori disciplinari interessati, deve essere indicato quello più presente nella trattazione della tesi).

Progetto svolto grazie al sostegno finanziario del **Programma Operativo Nazionale Ricerca e Innovazione 2014-2020 (CCI 2014IT16M2OP005), Fondo Sociale Europeo, Azione I.1 "Dottorati Innovativi con caratterizzazione Industriale"**

Università degli Studi di Torino

PhD Program in Chemical and Material Sciences XXXVII Cycle

Innovative Strategies for the Engineering of Sensors for Sustainable Food Systems

Noor Tayyaba

Supervisor: Prof Paola Rizzi

PREFACE

This preface outlines an overview of the key topics explored in this PhD thesis, entitled ***"Innovative Strategies for the Engineering of Sensors for Sustainable Food Systems"***. The work has been submitted to the Doctoral School of the University of Torino as part of the requirements for the PhD degree in Chemical and Material Sciences. The research presented in this thesis was carried out during the XXXVII PhD cycle (January 2022 to December 2024) within the Metallurgy Research Group, under the supervision of Prof. Paola Rizzi and the guidance of Dr. Federico Scaglione at the Department of Chemistry, University of Torino, Turin, Italy.

This thesis addresses critical environmental challenges by focusing on the fabrication of nanostructured metals and their applications in environmental sensing and remediation. It aims to develop sustainable and cost-effective methods for producing nanoporous metals with exceptional sensitivity and selectivity for detecting biomolecules and possible toxic agents.

Chapter I provides a comprehensive introduction to nanoporous metals and the contents of the thesis, underlining the motivation behind this research and its importance. It also provides a brief overview of each chapter's content, including key objectives and findings.

Chapter II summarized the analytical and characterization techniques employed throughout the study.

Chapters III to VII present the main findings of the research by discussing the fabrication methods, results, and conclusions for each nanostructured metal investigated during this period.

Chapter VIII concludes the thesis with a summary of the overall research and suggesting the future directions.

This thesis supports sustainable solutions to environmental challenges. It encourages further progress in nanostructured materials and their applications with the aspiration that it will inspire further advancements in nanostructured metals and their real-world applications.

Acknowledgment

First and foremost, I would like to express my deepest gratitude to my supervisor, **Prof. Paola Rizzi**, for her invaluable guidance, encouragement, and unwavering support throughout my PhD journey. Her insights and expertise have been instrumental in shaping this research, providing me with direction and inspiration. I am also profoundly grateful to **Dr. Federico Scaglione** for his constant mentorship, invaluable discussions, and technical assistance, which played a crucial role in the successful completion of this work.

My heartfelt gratitude extends to my beloved parents, **Mr. and Mrs. Muhammad Ayub**, whose unconditional love, sacrifices, and endless support have been my greatest source of strength. Their encouragement and prayers have been the driving force behind my perseverance and success. Their unwavering faith in me has served as the foundation of both my academic and personal growth.

With immense love and respect, I dedicate this thesis to my beloved parents, **Mr. and Mrs. Muhammad Ayub**, as a tribute to their endless sacrifices and unwavering belief in my potential.

A special note of appreciation goes to my family, whose unwavering love, prayers, and encouragement have been the cornerstone of my strength. Their support has been indispensable in overcoming the challenges faced during this academic endeavour.

I am deeply grateful to my sisters for their steadfast companionship, unwavering encouragement, and belief in my abilities. Their support has been a source of motivation, helping me stay focused and resilient throughout this journey.

Finally, I extend my sincere gratitude to all those who contributed, directly or indirectly, to the completion of this thesis. Your support, guidance, and belief in my work have been invaluable in making this journey both fulfilling and successful.

Thank you all.

Table of Contents

CHAPTER I

1.1 Introduction

The rapid development of various industries in recent years has resulted in increased production and widespread use of synthetic dyes in textiles, food, and cosmetics. However, improper disposal of dye-containing effluent poses serious environmental and health problems. As a result, there is greater emphasis on identifying organic pollutants to protect the environment [1]. As a result, developing efficient and affordable methods to detect and degrade harmful dyes is crucial to preventing their release into ecosystems. Toxic dyes can be detected using several spectroscopic techniques, such as Raman spectroscopy, infrared spectroscopy, mass spectrometry, UV-visible spectroscopy, and electroanalytical methods. Among these, surface-enhanced Raman spectroscopy (SERS) is particularly notable for its high sensitivity and selectivity in identifying trace contaminants and analytes. Nanostructured metals are promising candidates for SERS-active substrates due to their tunable physical and chemical properties, high surface area-to-volume ratio, and localized surface plasmon resonance. These unique features make them highly suitable for SERS applications [2]. Nanostructured metals not only enhance Raman signals of target analytes but also enable innovative methods for environmental monitoring. Recent advancements in this field have broadened the application of these materials in sensing technologies, opening new possibilities for detecting toxic pollutants and dyes. Despite this progress, achieving cost-effective and efficient production of these nanomaterials remains a challenge.

Nanostructured metals can be synthesized through both top-down and bottom-up methods, offering precise control over structural morphology and allowing material properties to be customized for specific applications [3]. Top-down methods involve converting bulk materials into nanoscale structures using techniques such as chemical dealloying, lithography, and ball milling. Lithography is particularly significant for semiconductor fabrication, as it enables precise patterning by selectively removing parts of the substrate. Ball milling, on the other hand, reduces bulk materials into nanoscale powders through friction and impact from grinding balls. Among these methods, dealloying stands out for its simplicity and ability to produce nanoporous materials on a large scale under moderate conditions [4]. This technique involves selectively removing specific components from a precursor material, resulting in a bi-continuous nanoporous structure formed through self-organization. Though the concept dates back to the Inca civilization, it has recently gained attention as an effective method for synthesizing nanoporous metals like silver (Ag) and gold (Au), which are highly effective for analyte detection due to their large surface area and high stability [5]. In contrast, bottom-up approaches construct nanostructures from atomic or molecular building blocks, offering precise control over material properties. For example, electrodeposition allows for accurate manipulation of the shape, size, and composition of materials by depositing them onto a substrate from a metal-ion-rich solution [6]. Both synthesis approaches play essential roles in advancing technologies for sensors and energy devices, each with its unique benefits and limitations.

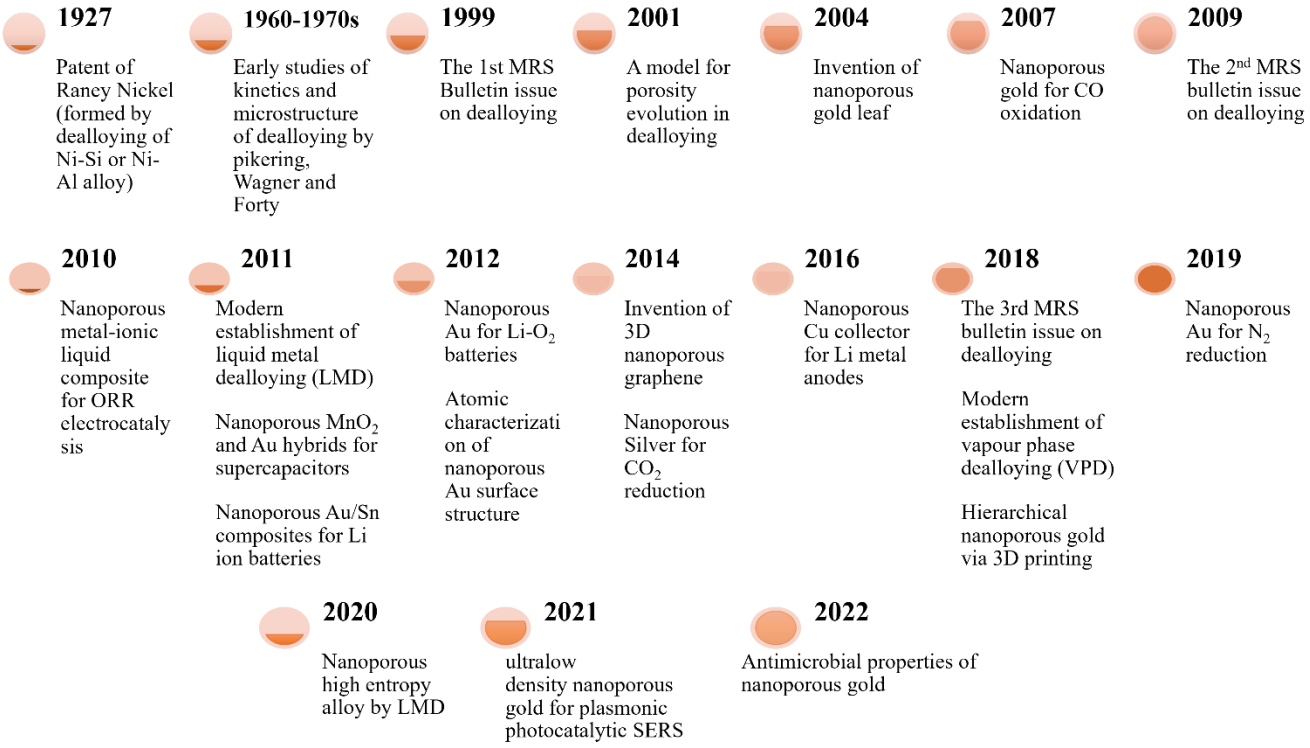

***Figure 1.1**: Histories of dealloyed materials [8]*

Furthermore, the dealloying topic was based on the three MRS Bulletin issues, released in 1999, 2009, and 2018, which present in-depth analyses of the subject. These MRS Bulletin issues seem to be a road map for dealloying research [7]. With the emergence of the "nano" idea, dealloying as a processing method has gotten a lot of interest. Many other porous metals have been formed due to dealloying, including Pt, Au, Cu, Ag, and Pd. It also plays a crucial role in producing nanoparticles with core shells for electrocatalysis, identifying the most efficient oxygen-reduction catalysts ever [7]. Moreover, 15 years ago, a successful model was introduced based on nano-porosity evolution. Since then, the subject has expanded rapidly, with research groups investigating dealloying and dealloyed materials worldwide. A brief timeline of the dealloying and dealloying materials is represented in Fig. 1.1 [8]. As research progresses, nanostructured metals emerge as promising candidates for developing innovations in cutting-edge technologies.

It was indicated from the literature review that np-metals with increased surface areas and reduced feature sizes offer enhanced performance in applications such as SERS, electrodes, and catalysis. Despite these advancements, improving synthesis procedures and understanding the basic mechanisms involved in dealloying still remains a difficult challenge [9]. The combination of the dealloying method with additives and surfactants has created a new way to develop tailored nanoporous metals that enhance their ability to detect various substances. The modified nanoporous metals may form complex structures that promote the formation of "hot spots" where the electromagnetic field enhancement is most prominent, significantly increasing

the sensitivity of dye detection [10]. However, research in this area is rapidly expanding, with a focus on creating novel nanostructured porous metals and alloys and investigating their distinct properties and performance. This is evidenced by the growing number of articles and reviews being published. Future studies will aim to create new types of nanostructured metals to expand the application of SERS substrates beyond conventional metals like gold (Au) and silver (Ag). This study will investigate non-noble metals, including copper (Cu), along with metal oxides that exhibit distinctive characteristics and reliable performance [11]. These advancements are anticipated to contribute in a detection system that is both more sustainable and efficient, thereby improving the sensitivity and accuracy of SERS applications. Furthermore, nanostructured metals have shown significant capability in degrading harmful dye molecules, making them appropriate for environmental monitoring.

Dyes represent complex compounds that can be classified based on their chemical structure and various applications. Azo dyes are an important class of synthetic dyes that play a major role in the dye market, accounting for around 70% of total dye production [12]. Thereby, in this thesis important azo dyes involving malachite green, methylene blue, and reactive red 195A, which are extensively employed in the textile industry because of their exceptional stability and resistance to light and chemicals were studied. These unique characteristics of these materials make them highly suitable for a range of industrial applications, such as textiles, pharmaceuticals, and aquaculture. Nonetheless, the potential toxicity and long-term environmental persistence present significant concerns [13]. Malachite green serves as an antifungal agent in aquaculture. However, its application has been limited due to potential carcinogenic risks [14]. Similarly, methylene blue is both a biological stain and a redox indicator but faces restrictions due to its inherent toxicity. In this research, a novel method has been proposed to mitigate these challenges by utilizing nanostructured metals as active substrates to detect and degrade harmful dyes precisely. The primary focus of this study is to develop and synthesize nanostructured metals, focusing on the fabrication of nanoporous gold (NPG), nanoporous copper (np-Cu), and electrodeposited porous copper (NPC). Alongside nanoporous metal synthesis, white cast iron powder (WCI-P) was also produced through a ball milling process, which plays a key role in degrading reactive red 195A dye. The main goal of this study is to fabricate nanoporous metals that are capable of detecting toxic dyes, particularly methylene blue and malachite green. The results obtained during the three-year PhD program are presented in the following chapters of this dissertation. The study is structured into three main parts. Each section offers a detailed and thorough discussion of these topics. Furthermore, the nanostructured metals in each chapter demonstrate great potential as cost-effective, efficient, stable, and sustainable alternatives for SERS and degradation applications. The subsequent paragraphs provide an overview of the content of each chapter, highlighting the main points discussed.

The 2nd chapter of this thesis focuses on the analytical tools and experimental methods used in the study. It provides a detailed overview of various characterization techniques, including surface-enhanced Raman spectroscopy (SERS) for detecting dyes such as malachite green and methylene blue. Additionally, it discusses scanning electron microscopy (SEM) combined with energy-dispersive X-ray spectroscopy (EDS), X-ray diffraction (XRD), and UV-visible

spectroscopy for evaluating dye degradation techniques used to characterize nanostructured metals. This chapter also highlights the working principles of each technique, clarifying how they support the research goals and findings presented in the dissertation.

In the 3rd chapter, a fast and efficient method of chemical dealloying coupled with a thiol-mediated compound is reported. As a thiol ligand, L-cysteine seems to be the best choice for controlling crystal growth by modifying the nucleation kinetics. This study used an $Au_{20}Cu_{48}Ag_7Pd_5Si_{20}$ alloy in an amorphous ribbon to demonstrate parts of the thiol-mediated chemical dealloying process. The as-spun Au-based amorphous ribbon was chemically dealloyed in HNO_3, HF, and L-cysteine solutions. The etching process was conducted at 70°C for 4 hours to examine the structural evolution of dealloying. For comparison, the standard NPG sample (NPG) was produced by dealloying in 10 M HNO_3 and 0.5 M HF without adding L-cysteine. For the L-cysteine-modified dealloying, three additional samples were fabricated and named 0.2 mM NPG, 0.4 mM NPG and 0.6 mM NPG. Following synthesis, the impact of surfactant on the structural morphology and crystallography was investigated using scanning electron microscopy in conjunction with energy-dispersive X-ray spectroscopy and X-ray diffraction analysis in a Bragg–Brentano geometry with monochromatic Cu Ka radiation.

In contrast, the 4th chapter demonstrates using NPG as an active SERS substrate for detecting malachite green dye. The resulting NPG has a highly porous structure with nanoscale ligaments that improve localized surface plasmon resonance (LSPR). A remarkable SERS performance was obtained using an NPG substrate to detect MGITC, resulting in a signal increase of 7.9×10^9. The SERS substrate had an incredibly low detection limit of 10^{-16} M. SERS analysis with the NPG substrate was versatile and fast for identifying MGITC.

The 5th chapter discussed the chemical dealloying of brass to synthesize the nanoporous copper (np-Cu). The effects of hydrochloric acid (HCl) concentration at various time and temperature conditions on the resulting structure were investigated to evaluate how these parameters impact the crystallographic structure and morphology of dealloyed brass bar.

The latter chapter, 6th details the formation of a three-dimensional porous copper film (NPC) through electrodeposition coupled with hydrogen dynamic bubbling technology (DHBT). Two types of NPC films are fabricated: one without additives and another incorporating cetyltrimethylammonium bromide (CTAB) as an additive. Comparative analysis is conducted on the effects of deposition time on the porous morphology, thickness, and SERS performance of both types of NPC films. The nanopore sizes were controlled by fine-tuning the deposition time, ranging from 26.8 to 73 μm without additives and from 12.8 to 24 μm with CTAB. The optimal NPC film without additives showed excellent SERS sensitivity at 180 s, while the film with CTAB demonstrated significant performance at 120 s for detecting methylene blue, a highly toxic dye with a detection threshold as low as 10^{-6} M.

In 7th chapter, an economical and efficient white cast iron powder (WCI-P) is presented with an innovative application for degrading azo dye, specifically the reactive red 195A (RR195A) in aqueous solutions. The WCI-P is produced by ball-milling solidified cast iron ribbons with a high surface area and distinct metastable properties. The study comprehensively assesses the

degradation efficiency of WCI-P under varying conditions, including dye concentration, temperature, and the reusability of the iron powder. The results indicate that 0.1 g of WCI-P can degrade RR195A dye in only 15 minutes. Additionally, increased temperature notably enhances degradation efficiency, emphasizing the role of thermal conditions in accelerating reaction rates. Remarkably, WCI-P maintained high degradation efficiency even after seven recycling cycles, underscoring its potential for sustainable wastewater treatment applications. This research introduces that white cast iron powder is an effective and economical solution for organic dye wastewater treatment, opening new directions for environmental remediation applications.

The 8th and final chapter summarize the major findings and discusses their implications for future research. The outcomes of this research are anticipated to have a significant impact on environmental chemistry by advancing nanostructured materials for SERS applications and dye degradation. By enhancing detection methods for toxic synthetic dyes, innovative degradation processes can be developed. This work aims to address critical issues in environmental monitoring and wastewater treatment, supporting a cleaner and safer environment. Through rigorous experiments and analyses. Furthermore, this research sets a foundation for future advancements in analytical chemistry and environmental remediation.

References

1. Liu, A.; Hu, G.; Wu, Y.; Guo, F. Life Cycle Environmental Impacts of Pyrometallurgical and Hydrometallurgical Recovery Processes for Spent Lithium-Ion Batteries: Present and Future Perspectives. *Clean Technol Environ Policy* **2024**, *26*, 381–400.

2. Zhang, Q.; Large, N.; Nordlander, P.; Wang, H. Porous Au Nanoparticles with Tunable Plasmon Resonances and Intense Field Enhancements for Single-Particle SERS. *J Phys Chem Lett* **2014**, *5*, 370–374.

3. Fujita, T.; Guan, P.; McKenna, K.; Lang, X.; Hirata, A.; Zhang, L.; Tokunaga, T.; Arai, S.; Yamamoto, Y.; Tanaka, N.; et al. Atomic Origins of the High Catalytic Activity of Nanoporous Gold. *Nat Mater* **2012**, *11*, 775–780, doi:10.1038/nmat3391.

4. Scaglione, F.; Rizzi, P.; Celegato, F.; Battezzati, L. Synthesis of Nanoporous Gold by Free Corrosion of an Amorphous Precursor. *J Alloys Compd* **2014**, *615*, S142–S147, doi:10.1016/j.jallcom.2014.01.239.

5. Scaglione, F.; Paschalidou, E.M.; Rizzi, P.; Bordiga, S.; Battezzati, L. Nanoporous Gold Obtained from a Metallic Glass Precursor Used as Substrate for Surface-Enhanced Raman Scattering. *Philos Mag Lett* **2015**, *95*, 474–482, doi:10.1080/09500839.2015.1093665.

6. Bommireddy, N.; Palathedath, S.K. Surfactant Mediated Electrodeposition of Copper Nanostructures for Environmental Electrochemistry: Influence of Morphology on Electrochemical Nitrate Reduction Reaction. *Journal of Solid State Electrochemistry* **2022**, *26*, 2733–2742.

7. Paschalidou, E.M.; Celegato, F.; Scaglione, F.; Rizzi, P.; Battezzati, L.; Gebert, A.; Oswald, S.; Wolff, U.; Mihaylov, L.; Spassov, T. The Mechanism of Generating Nanoporous Au by De-Alloying Amorphous Alloys. *Acta Mater* **2016**, *119*, 177–183, doi:10.1016/j.actamat.2016.08.025.

8. Wittstock, G.; Bäumer, M.; Dononelli, W.; Klüner, T.; Lührs, L.; Mahr, C.; Moskaleva, L. V; Oezaslan, M.; Risse, T.; Rosenauer, A. Nanoporous Gold: From Structure Evolution to Functional Properties in Catalysis and Electrochemistry. *Chem Rev* **2023**, *123*, 6716–6792.

9. Xiao, X.; Ou, W.; Du, P.; Lyu, F.; Diao, Y.; Lu, J.; Li, Y.Y. Ultrafine Nanoporous Gold via Thiol Compound-Mediated Chemical Dealloying. *Journal of Physical Chemistry C* **2020**, *124*, 10026–10031, doi:10.1021/acs.jpcc.0c01953.

10. Jing, Z.; Zhang, L.; Xu, X.; Zhu, S.; Zeng, H. Carbon-Assistant Nanoporous Gold for Surface-Enhanced Raman Scattering. *Nanomaterials* **2022**, *12*, doi:10.3390/nano12091455.

11. Chen, L.; Yu, J.; Fujita, T.; Chen, M. Nanoporous Copper with Tunable Nanoporosity for SERS Applications. *Adv Funct Mater* **2009**, *19*, 1221–1226.

12. Ahmadi, A.; Hajilou, M.; Zavari, S.; Yaghmaei, S. A Comparative Review on Adsorption and Photocatalytic Degradation of Classified Dyes with Metal/Non-Metal-Based Modification of Graphitic Carbon Nitride Nanocomposites: Synthesis, Mechanism, and Affecting Parameters. *J Clean Prod* **2023**, *382*, 134967.

13. Kansal, S.K.; Kaur, N.; Singh, S. Photocatalytic Degradation of Two Commercial Reactive Dyes in Aqueous Phase Using Nanophotocatalysts. *Nanoscale Res Lett* **2009**, *4*, 709–716.

14. Alderman, D.J. Malachite Green: A Review. *J Fish Dis* **1985**, *8*, 289–298.

Chapter II

EXPERIMENTAL AND CHARACTERIZATION TECHNIQUES

In this study, two different master alloys were produced using a Buehler electric arc furnace (Edmund Bühler GmbH, Bodelshausen, Germany). This process involved arc-melting of the high-purity elements ranging from 99.95% to 99.99% in an argon atmosphere, which was gettered with titanium. The compositions of the targeted alloy were expressed in atomic percentages: $Au_{20}Cu_{48}Ag_7Pd_5Si_{20}$ and $Fe_{82}C_{15}Si_3$. Following the arc-melting stage, the alloy ingots were rapidly solidified using a melt-spinning technique, also provided by Edmund Bühler GmbH, Bodelshausen, Germany, to produce ribbon forms.

2.1 Arc Melting Furnace:

The arc melting process is a common metallurgy method for the synthesis of a high-purity precursor alloy. This technique is based on an electric arc to generate intense heat, effectively melting materials with high melting points. It is particularly beneficial for producing metal and alloy ingots with uniform compositions and high precision, which are crucial for advanced material applications. In comparison to conventional melting processes, arc melting offers distinct advantages, as it helps to minimize both oxidation and contamination, yielding higher-quality materials [1].

2.1.1 Working Principle:

An electric arc is established between a tungsten electrode and the metals arranged in a crucible to synthesize these alloys. The tungsten electrode serves as the heat source and generates temperatures exceeding 2000°C, which melts the metals and allows them to combine into an alloy. However, the melting process is frequently repeated to improve the uniformity of the alloy. This repetition ensures that the melted metals are entirely mixed, resulting in a more homogeneous composition across the alloy. Furthermore, the chamber was evacuated to prevent melt oxidation. After evacuation, the chamber is filled with argon gas, which provides an extra layer of protection against contamination, maintaining the integrity of the alloy throughout the melting process. A descriptive diagram of an arc melting furnace is presented in Fig. 2.1.

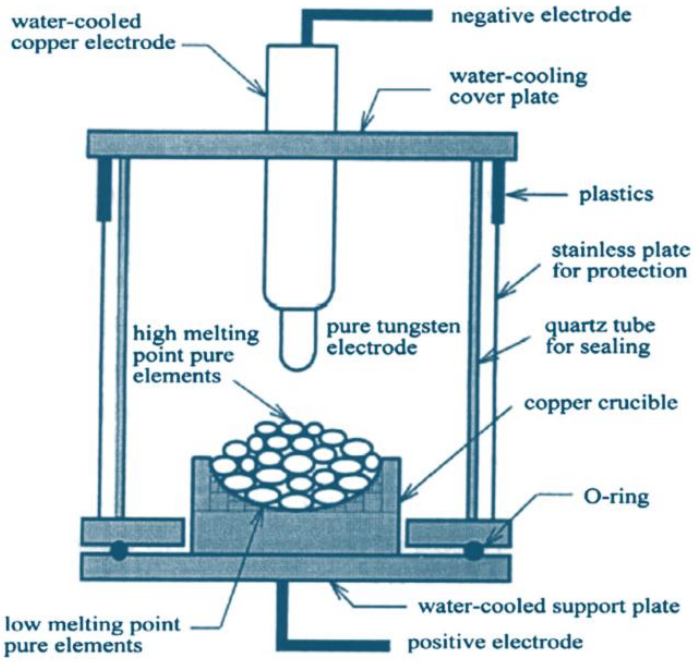

***Figure 2.1**: Arc Melting Furnace*

2.2 Rapid solidification

Rapid solidification techniques attract significant interest in materials science because they produce metals with unique microstructures and enhanced properties that cannot be achieved through conventional processing methods. The primary objective of rapid solidification is to facilitate high cooling rates during the solidification process, leading to the development of fine-grained microstructures, in contrast to the coarse-grained structures typically produced by conventional methods. This is accomplished through external cooling methods or by quenching liquid metal, resulting in temperatures reaching 10^5-10^8 K/s. Various rapid solidification methods, including melt spinning, spray forming, gas atomization, mechanical alloying, and powder metallurgy, are employed to obtain fine-grained microstructures/nanocrystalline microstructures demonstrating improved mechanical, chemical, and thermal properties.

2.2.1 Melt Spinning: A Key Technique in Rapid Solidification

Melt spinning is one of the prominent techniques used in rapid solidification, allowing the rapid cooling of molten liquid to produce metallic metastable solid solutions in the form of thin ribbons with unique microstructures and properties [2]. This process not only influences the final shape of the material but also plays a crucial role in determining its microstructural characteristics. This thesis focuses on $Au_{20}Cu_{48}Ag_7Pd_5Si_{20}$ amorphous ribbon as a precursor for NPG. The synthesis of the amorphous ribbon involves two main steps: the preparation of the master alloy, as detailed earlier, and the subsequent melt spinning of the alloy to produce the amorphous ribbon. The master alloy was placed in a quartz crucible and melted using induction heating. The molten liquid alloy was discharged by argon gas at a pressure of around 0.35 bar onto a copper wheel traveling at a velocity of 20 m/s in a vacuum. The chamber was maintained

at an argon pressure of approximately 1 bar. Solidification takes place on the molten spinning copper wheel, resulting in the formation of ribbons that can be easily detached from the wheel surface due to variations in thermal contraction. Two distinct morphologies are observable on the ribbon: the airside, characterized by its luminous, glossy, and flat appearance, and the wheel-side, which is opaque and irregular due to the entrapment of Ar gas bubbles between the ribbon's wheel side and the rotating wheel, leading to the formation of air cavities within the apparatus.

2.2.2 Working Principle of Melt Spinning

Melt spinning involves rapidly quenching liquid metal on a rotating copper wheel, as shown in Fig. 2.2. The high thermal conductivity of copper wheels allows rapid solidification of melted metal by rapidly removing its heat. Furthermore, the cooling rate and wheel speed play essential roles in determining the microstructure of the finished ribbon.

- **High Cooling Rates:**

As the ribbon rapidly cooled, it formed a fine-grained microstructure with a high density of dislocations. These small microstructures enhance the ribbon's mechanical properties, leading to improvements in strength and wear resistance. For example, if the system works as a glass former, it is possible to produce a metallic glass rather than undergoing crystallization.

- **Low Cooling Rates:**

On the other hand, melt-spun ribbons tend to grow coarser when the cooling rate decreases.

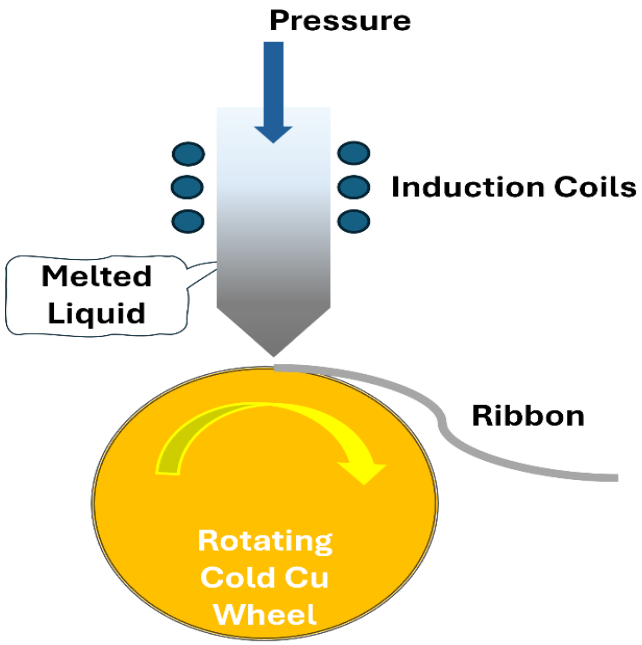

***Figure 2.2**: Schematic diagram of a single roller melt spinning apparatus*

2.3 Ball Milling

Ball milling is a flexible and commonly utilized technique in the production of materials for powder metallurgy. This process effectively reduces materials to fine powders by placing them in a rotating cylindrical chamber filled with small metallic or ceramic balls. As the cylinder turns, the balls move up and down, grinding the material into uniform particle sizes, as shown in Fig. 2.3.

2.3.1 Working Principle

The ball milling technique operates primarily on impact and attrition principles. Particle size reduction occurs as the balls near the top of the rotating cylinder's wall fall onto the material below. The milling process starts with placing the material and grinding medium into a cylindrical chamber. As the chamber rotates, centrifugal force raises the balls, which then drop, colliding with the material. This action produces impact and frictional forces, breaking particles into smaller sizes. Ball milling can be performed under wet or dry conditions, depending on the required properties of the final product [3]. As a fundamental method in material science, the ball milling method includes powder metallurgy and chemical synthesis, which are simple, basic, but effective approaches.

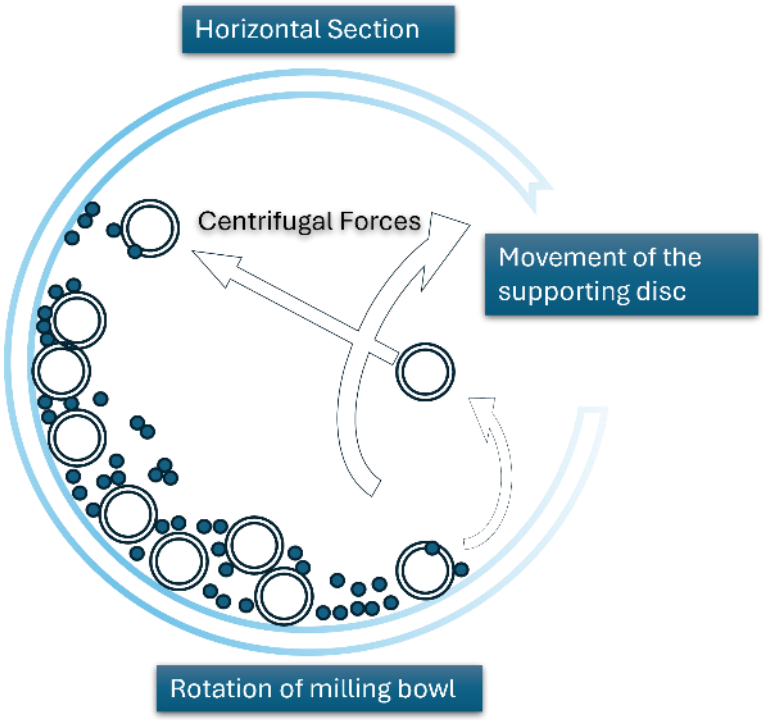

Figure 2.3: *Schematic illustration of a ball motion and powder mixture*

Characterization Techniques

This section summarizes the procedures used to characterize the samples during the research process. The techniques used are X-ray diffraction (XRD), scanning electron microscopy (SEM) with energy dispersive X-ray spectroscopy (EDS), surface-enhanced Raman spectroscopy, and an electrochemical setup.

2.4 X-ray Diffraction (XRD)

X-ray diffraction (XRD) is a powerful, non-destructive analytical technique used to determine the structural properties of powder, and solid, such as their crystal structure, phase composition, and orientation. The process begins with the production of X-rays in a cathode ray tube, where high-energy electrons bombard a target material and emit X-rays. These X-rays are filtered to produce monochromatic radiation, which is then focused on the sample. As X-rays interact with the crystal lattice, they scatter in a specific direction. The scattering of X-rays from a crystal lattice results in the observation of intensity peaks that depends on the constructive interference of monochromatic X-rays with a crystalline specimen. Furthermore, the process of phase identification involves comparing the X-ray diffraction patterns obtained from unknown samples with reference databases, allowing accurate characterization of the material's structure [3].

2.4.1 Working Principle

An XRD system comprises three primary parts: the X-ray source, a sample holder, and a detector, as shown in Fig. 2.4. The X-ray source helps to emit the X-rays that are directed toward the sample, where they interact with its crystalline phases. The detector captures the diffracted X-rays and produces a diffraction pattern. In addition, the angle of diffraction, denoted as 2θ, represents the angle between the incident and diffracted beams. The intensity of the diffracted X-rays is recorded by changing the angle, which allows the diffraction data to be compiled. The angle between the incident beam and the sample is variable, depending on the diffractometer's design and the sample's characteristics. However, to satisfy the Bragg condition for diffraction, this angle is typically aligned with that of the diffracted beam.

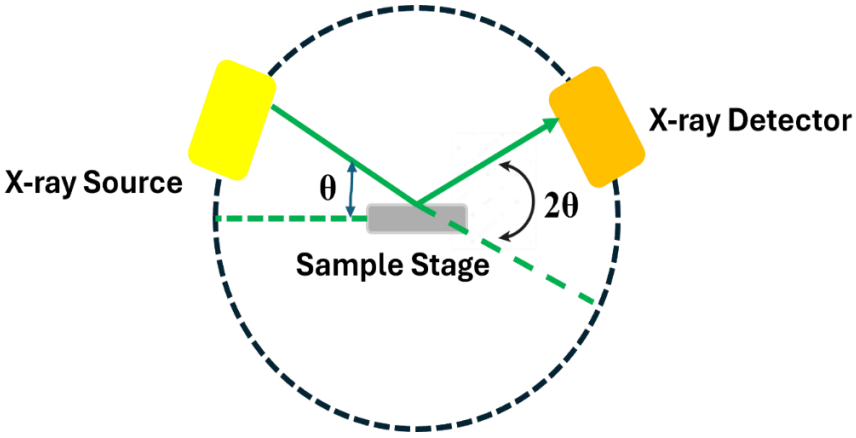

Figure 2.4: *Schematic representation of X-ray*

2.5 Scanning electron microscopy (SEM) combined with energy-dispersive X-ray spectroscopy (EDS)

Scanning electron microscopy coupled with energy-dispersive X-ray spectroscopy (SEM/EDS) is an effective analytical tool for investigating sample surface morphology. This technique employs a highly concentrated scanning electron beam to produce high-resolution surface images with a considerable depth of focus for detailed topographical analysis.

2.5.1 Working Principle

During SEM investigation, high-energy primary electrons ranging from 0.5 to 30 kV penetrate the sample surface, producing many low-energy secondary electrons. The intensity of these secondary electrons strongly depends on the material's surface roughness. Furthermore, as the primary electron beam scans the sample surface, the intensity of the secondary electron can be detected to create an image of the surface. Furthermore, when secondary electrons are released from a sample owing to interaction with an electron beam, they may be replaced by higher energy electrons, resulting in the emission of different X-rays. These X-rays are specific to the elements from which they are produced; therefore, the elemental composition of the sample surface may be identified [4]. This information is critical in determining the chemical makeup of a sample.

2.6 Electrochemical Setup

An electrochemical cell is a device that generates electrical energy via chemical processes or utilises electrical energy to initiate chemical reactions. This thesis employs a three-electrode electrochemical cell for electrodeposition, utilising the dynamic hydrogen bubbling method in its electrochemical setup. The electrochemical cell was linked to a MetroOhm Instruments PGSTAT302N Potentiostat. The data was analysed using the NOVA 2.0 software. Furthermore, a potentiostat serves as a device that accurately regulates and observes potential and current within an electrochemical cell. The potentiostat employs a combination of static and dynamic measurements to provide in-depth insights into the electrochemical characteristics and performance of materials. In order to better understand material stability and equilibrium properties such as steady-state current responses, static measurements were performed with a potentiostat that maintained a fixed potential or current. To investigate time-dependent behaviours and kinetics, dynamic measurement was used, which involves varying the potential or current over time.

2.6.1 Working principle (Three electrode cell)

A standard setup used for electrochemical experiments involves three electrodes for potentiostatic measurements to study the behavior of electrochemical systems [5]. This setup consists of three main components, as represented in Fig. 2.5:

- **Working electrode:** This is the sample being studied where the oxidation or reduction reaction of interest takes place, and its potential is controlled.

- **Counter electrode:** This platinum grid has a greater surface area compared to the working electrode. It aims to finish the electrical circuit by allowing current to pass through the cell. Furthermore, at the counter electrode, complementary reactions take place to maintain equilibrium with the processes occurring at the working electrode (WE). Under anodic conditions, the working electrode facilitates oxidation, while the counter electrode acts as a cathode for reduction, and the roles reverse in the opposite scenario. This ensures the current's flow and maintains the overall charge balance of the electrochemical cell.

- **Reference electrode:** A reference electrode made of Ag/AgCl and filled with a saturated KCl solution provides an accurate and precise reference potential.

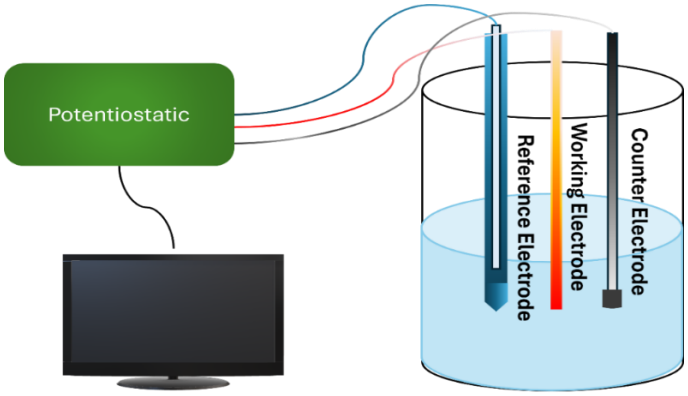

Figure 2.5: *Schematic representation of the three-electrode electrochemical setup*

2.7 Surface-enhanced Raman spectroscopy (SERS)

Surface-enhanced Raman spectroscopy (SERS) is an extremely sensitive analytical method used in various scientific fields, including biochemistry, catalysis, and materials science. Electromagnetic enhancement and charge transfer are the primary mechanisms by which the Raman scattering signal of molecules adsorbed onto metallic nanostructures experiences an enhancement. This signal is further amplified through the combined methods, allowing for the detection of analytes even at very low concentrations. The overview of the SERS mechanism is illustrated in Fig. 2.6. Furthermore, the efficiency of SERS is determined by the substrate properties and analyte surfaces. Au and Ag nanoparticles are effective SERS substrates because their plasmon resonance frequencies coincide with those of visible and near-infrared radiation, resulting in maximum signal enhancement [6]. SERS spectra are notably different from standard Raman spectra because of interactions between metal surfaces and molecules, allowing for greater sensitivity and overcoming standard Raman spectroscopy restrictions such as weak signals and fluorescence interference.

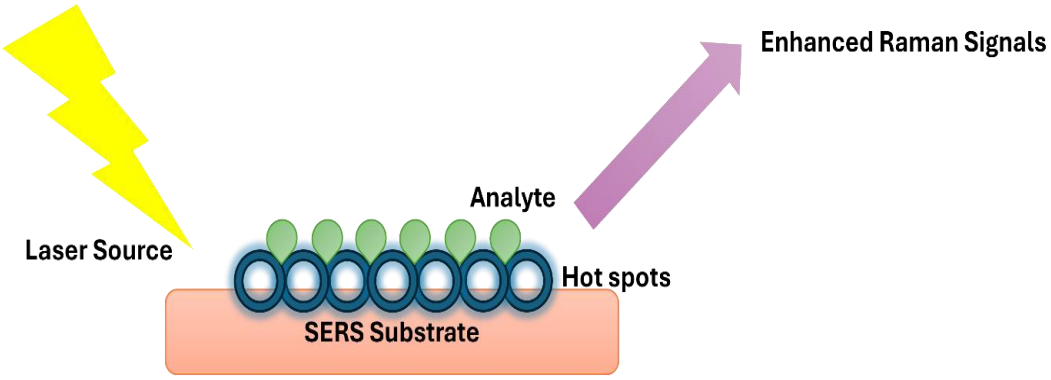

Figure 2.6: *Overview of surface-enhanced Raman spectroscopy*

2.7.1 Working Principle

Two main mechanisms enhance the signals of surface-enhanced Raman spectroscopy (SERS).

- **Electromagnetic enhancement**:

The main concept of electromagnetic enhancement in SERS involves transforming incoming energy into plasmons, representing the collective oscillations of electrons on a metal surface. These surface plasmons create localized optical fields. The strength of these optical fields is determined by different parameters such as the shape, size, arrangement of nanoparticles, their concentration, and the surrounding conditions. The substrate surface contributes to forming a nanoscale corrugated surface, which improves interaction with laser light and enhances signal quality. The roughness of this surface correlates with the resonance frequencies at which surface plasmons scatter light, influencing the formation of "hotspots" with lengthy lives. When a metal nanoparticle resonates at the same frequency as the excitation source, Localized Surface Plasmon Resonance (LSPR) occurs. The characteristics of surface plasmons and LSPR are essential for electromagnetic enhancement. The plasmon transfers energy to the analyte, facilitating scattering. The energy is subsequently returned to the plasmon through wavelength-shifted light, specifically amplified Raman signals caused by molecular vibrations. In contrast to the excitation field, the localized electric field between particles peaks in certain places. In contrast to the excitation field, the localized electric field between electrons reaches its optimal level in specific regions. Hotspots are generally found around sharp points and edges of plasmonic nanostructures, where the most significant Raman amplification occurs.

- **Charge transfer enhancement:**

In SERS, electrons move from the Fermi level of a metal substrate to either the highest occupied molecular orbital (HOMO) or the lowest unoccupied molecular orbital (LUMO) of an analyte molecule. The metal surface acts as the substrate for analyte detection, with resonant chemical amplification occurring only in the presence of hotspots. The level of amplification depends on the nature of the analyte, which must bind directly to the metal surface for effective detection. Unlike electromagnetic enhancement, non-resonant enhancement is independent of the excitation wavelength, resulting in a relatively lower degree of Raman signal amplification.

2.8 UV–visible spectroscopy

UV–Vis spectroscopy is an analytical technique that measures a material's absorption of ultraviolet or visible light. This approach can be used at specific wavelengths or across the spectrum, making it useful for various analytical applications. This approach is frequently used in quantitative and qualitative analyses, allowing researchers to quantify the concentration of chemicals and identify compounds based on their absorption properties. Measurements can be made quickly, making them easy to integrate into the experimental protocol [7]. A schematic diagram of a component of a UV–visible spectrometer is depicted in Fig. 2.7.

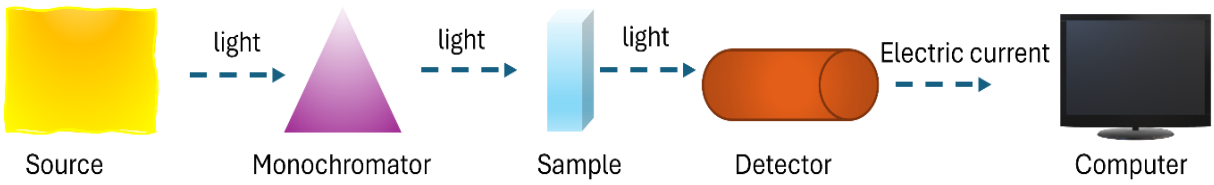

***Figure 2.7**: Schematic diagram of UV–visible spectroscopy*

- **Light Source:**
  The light source consists of tungsten/halogen and deuterium lamps, providing a continuous spectrum of visible and near-ultraviolet radiation from 200 to 800 nm.
- **Monochromator:**
  The output from the light source is directed onto the monochromator, which efficiently disperses the incoming light into its component wavelengths, similar to a prism, but with greater effectiveness.
- **Sample Holder:**
- A sample holder, also known as a cell or cuvette, is an optically flat and transparent container made of glass or quartz. It is designed to ensure optimal light transmission while preventing UV light interference, allowing for precise measurements.**Reference cells:**
  A reference cell is a separate cuvette containing only the solvent in which the sample is dissolved. It serves as a blank, providing a baseline for comparison and ensuring accurate spectroscopic measurements.
- **Detector:**
  After passing through the sample, the remaining light is detected and converted into an electronic signal. To determine the absorbance at various wavelengths, these signals can be analyzed via different software like Origin or Excel.

2.8.1 Working Principle

This technique studies the wave-like behavior of electrons within molecules, providing insights into their electronic structure. It enables materials to absorb, reflect, emit, or scatter light. Absorption occurs when the incident light energy matches the energy gap (ΔE) between a

molecule’s ground and excited states. A photon of sufficient energy is absorbed, and allow an electron to move from a lower-energy ground state to a higher-energy excited state. The link between energy and absorption is described by Planck's equation.

$$E = {}^{hc}/_{\lambda}$$

Where h denotes Planck's constant, while c represents the speed of light. Absorbance measurements are commonly used in quantitative analysis to ascertain the concentration of an unknown substance. This is achieved through the Beer-Lambert law, which explains how light intensity diminishes as it travels through different materials. However, absorbance is directly proportional to the sample concentration (c), molar absorptivity (ε), and the path length of the cuvette (l). This relationship is expressed by the following equation, .

$$A = \varepsilon cl$$

where absorbance represents the number of molecules in the sample that interact with light. A concentrated sample contains more molecules, which leads to a higher absorbance. Similarly, a longer route length allows light to pass through more of the sample, increasing the number of chemical reactions and thus absorbance.

References

1. Moss, A.R. Arc-Melting Processes for the Refractory Metals. *J. Less-Common Metals* 1959, *1*.

2. Jech, R.W.; Moore, T.J.; Glasgow, T.K.; Orth, N.W. Rapid Solidification via Melt Spinning: Equipment and Techniques. *JOM* 1984, *36*, 41–45.

3. Epp, J. X-Ray Diffraction (XRD) Techniques for Materials Characterization. In *Materials characterization using nondestructive evaluation (NDE) methods*; Elsevier, 2016; pp. 81–124.

4. Girão, A.V.; Caputo, G.; Ferro, M.C. Application of Scanning Electron Microscopy–Energy Dispersive X-Ray Spectroscopy (SEM-EDS). In *Comprehensive analytical chemistry*; Elsevier, 2017; Vol. 75, pp. 153–168 ISBN 0166-526X.

5. EC08, A.A.N. Basic Overview of the Working Principle of a Potentiostat/Galvanostat (PGSTAT)–Electrochemical Cell Setup. *Metrohm Autolab. BV* 2011, 1–3.

6. Sharma, B.; Frontiera, R.R.; Henry, A.-I.; Ringe, E.; Van Duyne, R.P. SERS: Materials, Applications, and the Future. *Materials today* 2012, *15*, 16–25.

7. Förster, H. UV/Vis Spectroscopy. *Characterization I: -/-* 2004, 337–426.

CHAPTER III

Unlocking the Potential of L-Cysteine in Chemical De-alloying

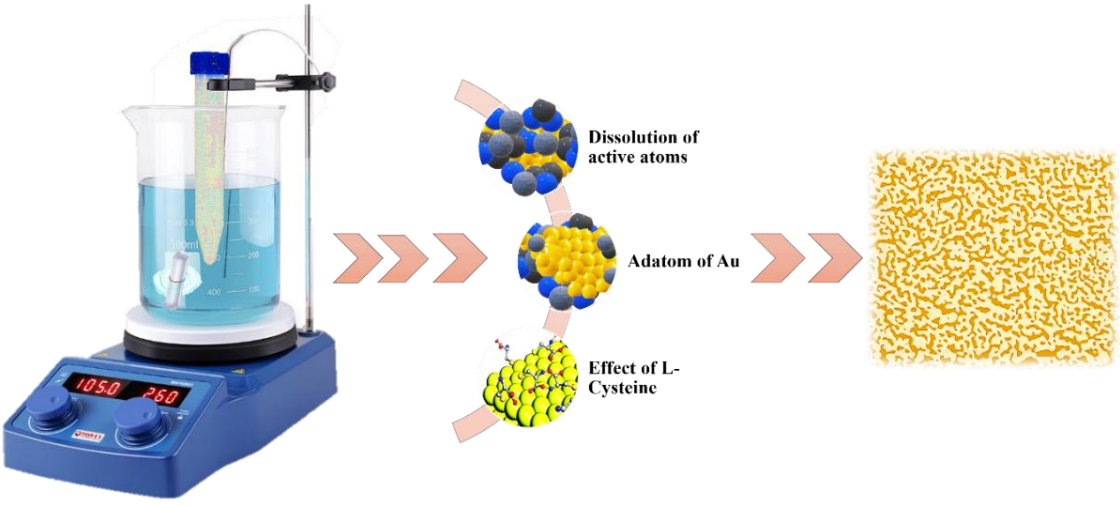

Chemical Dealloying Process Mechanism of Chemical Dealloying Ultrafine structure of NPG

3.1 Introduction

Nanoporous metals, especially NPG, have gained considerable attention due to their outstanding catalytic activity, plasmonic properties, and electrical conductivity. The development of NPG structures began in the 1960s to investigate alloy corrosion mechanisms at a molecular level. In the late 1990s and early 2000s, the potential of NPG was recognized owing to its advantageous properties, including a high surface area, abundant active sites, superior conductivity, ease of modification, tunable porosity, and favorable biocompatibility [1]. One of the earliest applications of nanoporous metals explored was in the field of catalysis. In 1987, Haruta et al. discovered that gold nanoparticles exhibited unexpected catalytic activity for CO oxidation at temperatures below room temperature. It was a very unexpected discovery, considering that gold had previously been considered inert and incapable of catalysis [2]. Since then, sub-nanometer gold has gained considerable interest, leading to extensive research in catalysis, sensors, microelectronics, and biological applications. These metals are mainly produced via dealloying, which selectively dissolves an alloy's more reactive component while keeping the nobler metal's self-arranged, bicontinuous nanoporous structure intact [3]. This technique has proven to be the most common and convenient among various approaches. The fabrication of NPG typically involves dealloying silver from gold-silver alloys, with nitric acid often used as the etching agent. The resulting NPG structures exhibit a three-dimensional sponge-like framework with nanoscale irregular pores, providing a high surface-to-volume ratio [4]. Despite significant progress, challenges remain in optimizing the synthesis of nanoporous materials and understanding the fundamental processes involved in dealloying.

Different mechanisms of dealloying process have been proposed to elucidate the dealloying process, which is briefly illustrated in the flow diagram. In the dissolution-redeposition mechanism as represented in Fig 3.1, both alloy surface components dissolve simultaneously during dealloying. The noble component precipitates near the dissolution site and is redeposited onto the matrix. While the main component remains in the solution. However, this simultaneous dissolution is impossible if the base component's potential is considerably lower than the anodic dissolution threshold [5]. Consequently, the dissolution-redeposition mechanism alone cannot fully explain situations where the primary constituent is released while the noble component becomes insoluble.

Pickering et al. [6] suggested that the dealloying process occurs through a volume diffusion process. In this model, active elements at the surface dissolve anodically, creating double vacancies. These vacancies then diffuse into the alloy due to concentration gradients, with active surface components dissolving preferentially. However, this model can be difficult since the diffusion rate of active elements toward the alloy surface is inadequate at room temperature to match the rate of the dealloying process. Forty et al. [7] summarize Ag_2Au and Au_2Cu system experiments and propose the surface diffusion model. The dissolution of active elements introduces randomness into the alloy system, while the surface distribution of noble components promotes an ordered structure. While noble component atoms diffused to form clusters on the surface to reduce surface energy, active component atoms dissolve into the electrolyte. The aggregation of Au atoms results in a thick Au layer, although Sieradzki and colleagues propose a percolation process driven by surface diffusion. The percolation model clearly explains the phenomenon of the dealloying process that causes the critical potential to appear. Before dealloying, the active component fraction in the alloy must be greater than a critical threshold, and a three-dimensional bimetallic/pore morphology is generated [8]. However, the experimental results and the theoretical simulation do not match with each other.

Erlebacher et al. [9] presented a phase separation process in 2001 and developed a model that facilitates the formation of NPG from Ag-Au alloy systems. This study suggested that the electrolyte-alloy interface served as the primary site where a physical mechanism impacted the formation of the porous structure. This interface was divided into three specific areas: the alloy region, the electrolyte region, and a thin atomic layer at the alloy/electrolyte boundary. The formation and progression of nanoporous structures through the selective dissolution of Ag and the self-diffusion of Au were explored through kinetic Monte Carlo simulations. The process initiates with the removal of an individual Ag atom from a close-packed (111) alloy surface, resulting in a terrace void. This void exposes Ag atoms with fewer lateral bonds, making them more susceptible to breakdown than those on the terrace.

Eventually, the entire terrace is stripped, leaving Ag atoms without lateral support. The remaining Au atoms then start to spread and cluster. Due to Au's stable chemical properties, these clusters help passivate adjacent alloy surfaces, forming distinct zones: one with passivated Au clusters and another with exposed, undealloyed material. More Au atoms were released to the surface as the Ag atoms was dissolved. therefore, the self-diffusion allowed Au atoms to penetrate the prior layer and emerge from the un-dealloyed substance. Initially, these

Au clusters formed Au-rich layers from the original Ag-Au alloy. The base was eroded, expanding the surface area that Au had to cover for passivation. This process led to pit formation and the development of porosity [10].

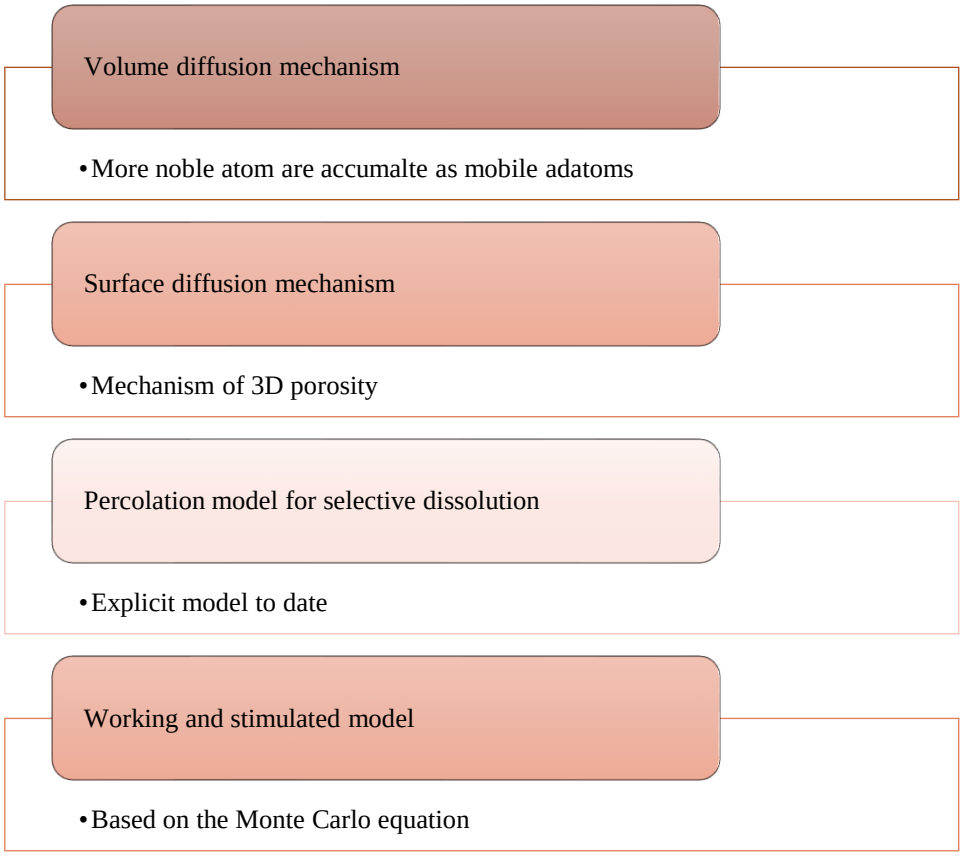

***Figure 3.1**: History of dealloying mechanisms*

On the other hand, the dealloying process requires at least binary or multicomponent alloys. As a result of the alloy's fewer noble metals being oxidized, the gold atoms assemble, and a complex NPG structure is produced. The resulting NPG exhibits a new 3D bicontinuous structure with ordered open pores and nanoscale interconnecting ligaments; due to these structural features, NPG possesses impressive properties, for instance, a high surface-to-volume ratio, mechanical strength, catalytical activity, electrical conductivity, efficient mass transfer, plentiful surface defects making it a multifunctional material, as shown in Fig 3.2 [11]. NPG's properties are influenced by nanopore size and residual components, and understanding these factors is crucial for advancing gold catalysis research [12].

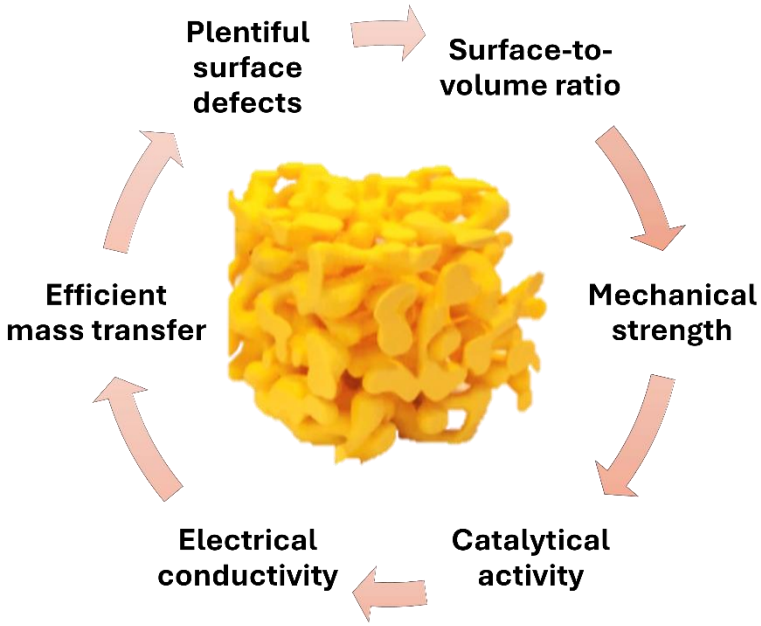

***Figure 3.2**: Visual representation of structural features and properties of NPG [11]*

Based on the fundamental principle of selectively removing the specific elements from an alloy, various dealloying methods have been developed, combined with interfacial atom diffusion or surface processes to form a continuous nanoporous structure. Considering the physicochemical properties of the alloy components involved in selective leaching, the main methods for producing nanoporous metals include the chemical dealloying method represented as CD, electrochemical dealloying method ECD, vapor phase dealloying method VPD, and liquid metal dealloying LMD method. Each method presents distinct advantages and limitations, as shown in Table 3.1. Electrochemical dealloying provides precise control over the process and enables tailoring the resultant material's properties by modifying dealloying potential and electrolyte composition [13]. However, this approach is largely restricted to noble metals, stable compounds, and transition metals that easily undergo passivation, generating chemical waste that raises environmental concerns. On the other hand, Liquid metal dealloying effectively produces bicontinuous porous structures by selectively dissolving components based on the enthalpy of mixing between the liquid metal and alloy. Still, this method encounters problems, including thermal coarsening, and frequently requires additional chemical corrosion treatment to attain the appropriate properties [14].

Vapor phase dealloying is remarkable for its environmental sustainability, producing less chemical waste than alternative procedures and allowing a variety of materials to create three-dimensional porous structures [15]. However, it requires sophisticated designs to sustain high vacuum and temperature conditions, restricting accessibility for some applications. Among these methods, chemical dealloying stands out for its simplicity and cost-effectiveness. It requires few tools and conditions and economical precursor materials that make it frequently employed. This approach facilitates straightforward structure, shape, and composition alterations by modifying precursor components and synthesis parameters. Moreover, it enables cost-effective mass production of nanoporous metals with stable architectures, including 3D NPG featuring changeable pore dimensions [3].

Table 3.1: Comparison of different dealloying methods

Strategies	CD/ ECD	LMD	VPD
DF for SD	Alloy components vary in chemical activity.	Variation in mixing enthalpy of alloy components & liquid metal.	Alloy components differ in saturated vapor pressure.
Dealloying Velocity	10 nm s^{-1}	1µm s^{-1}	-
Advantages	Simple procedure.	Suitable for both active and refractory metals.	Electrochemical activity, conductivity & miscibility are not constrained.
	Produce bicontinuous nanocomposite.	Fabricate bicontinuous nanocomposite materials.	Liquid-free components.
Limitations	Produce toxic waste.	Large pore/ligament size due to high temp. processing	Large pore/ligament size due to high temp. Processing
	Not suitable for active metals.	An extra etching operation is required to expose the porous structure.	Complex processing setup due to high temperature & vacuum conditions.
Kinetic of Dealloying	Controls by the reaction of interface dissolution.	Diffusion-limited flow determined the porosity	Transport becomes interface-limited rather than diffusion-limited at a threshold dealloying depth, leading to kinetics.
Examples	(Ag-Au system)	(Ta-Ti system)	(Mn-Zn system)

CD: chemical dealloying, ECD: Electrochemical dealloying, VPD: Vapor phase dealloying, LMD: liquid metal dealloying, DF: Driving force, SD: selective dissolution.

However, producing NPG with extremely small feature sizes poses significant challenges, especially in controlling the accumulation and diffusion of Au atoms at the interface of electrolytes or metals [16]. However, it is difficult to achieve pore sizes smaller than 10 nm with the traditional method of dealloying at room temperature. Due to the high diffusion rate of Au atoms at the metal or electrolyte surface.

To overcome these challenges, recent research has explored alternative strategies, such as pre-doping the alloys before treating them with precious metal atoms like platinum, utilizing low-temperature dealloying, and applying electrochemical dealloying method to enhance the dealloying rate of less noble metals, such as silver (Ag). Even with these developments, these techniques frequently demand the utilization of expensive precious metals, challenging methods, extra tools (such as potentiostats), or complicated and rigid procedures that limit

control over the final morphological size of nanostructured materials [17]. As a result, a simple and adaptable approach for producing ultrafine nanoporous metals is very desirable.

Furthermore, introducing surfactants in the dealloying process may significantly change the surface morphology of NPG. The capability of capping agents, including ligands, surfactants, polymers, and dendrimers, to control the formation of Au nanoparticles has been widely studied [18]. By selectively adsorbing chemical molecules onto specific crystal facets of Au, the internal surface of NPG can be modified. The method of surfactant modification during dealloying significantly improves the structural integrity of NPG while also increasing its catalytic activities. For example, employing surfactants such as pyrogallol or sodium citrate in the dealloying process can result in NPG highlighting modified surface structures demonstrating markedly enhanced catalytic performance relative to traditional NPG. Standard NPG is less porous than surface-modified NPG with enhanced electrocatalytic activity. By optimizing dealloying conditions with surfactants, it is possible to effectively control the nanoporous structure's size and morphology, paving the way for high-performance three-dimensional nanoporous catalysts suitable for various chemical and electrochemical applications [19].

In this chapter, a novel and sustainable production process is proposed to achieve an innovative NPG sensor with high catalytic activity and ultrafine ligament size by introducing L-cysteine with chemical dealloying techniques. As the thiol ligand modifies the kinetics of nucleation, L-Cysteine seems to meet best this requirement for controlling crystal growth. We employ an $Au_{20}Cu_{48}Ag_7Pd_5Si_{20}$ alloy that has been rapidly solidified into an amorphous ribbon to demonstrate parts of the thiol-mediated chemical dealloying process. The link between L-cysteine and gold was investigated by altering the concentration of L-cysteine in a solution containing the electrolytes. The influence of L-cysteine interactions and the diffusion of Au atoms at the electrolyte interface or alloy and on the shape of NPG was assessed. This process efficiently produces ultrafine NPG and is suited for large-scale manufacturing, offering an affordable route for developing high-performance nanoporous metal frameworks for tailored applications. In the second part of this chapter, NPG serves as an active substrate for detecting malachite green dye via SERS). The resultant NPG shows a highly porous architecture defined by nanoscale ligaments, significantly augmenting localized surface plasmon resonance (LSPR). This SERS substrate demonstrates a very low detection limit of 10^{-16} M, highlighting its effectiveness. Furthermore, the NPG substrate exhibits exceptional stability and repeatability in SERS studies. The sensitivity and selectivity of malachite green dye make it an ideal instrument for environmental monitoring and food safety assessment.

3.2 Material and Methods

A master alloy with the composition $Au_{20}Cu_{48}Ag_7Pd_5Si_{20}$ was produced using an arc-melting of pure elements ranging from 99.95% to 99.99%. This process was performed in a Ti-gettered argon atmosphere via an electric arc furnace of Buehler, Edmund Bühler GmbH, Bodelshausen, Germany. This particular composition resulted from an ideal amorphous precursor that demonstrates excellent glass-forming properties. The melt-spinning apparatus, model Edmund

Bühler GmbH, Bodelshausen, Germany rapidly solidified the molten alloy in ribbons [20]. The molten alloy, contained in a quartz crucible, was expelled through a 2 mm nozzle onto a copper wheel rotating at 25 m/s in an argon-protected environment, forming amorphous ribbons of 25 μm and 2 mm with a thickness and width, respectively. Subsequently, the as-quenched amorphous ribbon was de-alloyed in a water bath containing an electrolyte composed of 10 M HNO_3 and 0.5 M HF at 70 °C for 4 hours. The treated sample was then thoroughly rinsed with double-distilled water, air-dried, and stored in a clean vial for future characterization. HF was specifically used to prevent SiO_2 formation. Hereafter, this sample will be referred to as 0 mM NPG.

Different concentrations were selected to assess the impact of L-cysteine on the morphology of NPG. Initially, concentrations of 4 mM, 8 mM, and 16 mM L-Cysteine were tested while maintaining the remaining conditions constant, that was, 0.5 M HF and 10 M HNO_3 at 70 °C for 4 hours. Subsequently, three additional samples were prepared, each featuring distinct concentrations of L-cysteine at 0.2mM, 0.4mM, and 0.6mM. After preparation, these samples underwent multiple rinses with double distilled water to remove residual acid or additives. Then, these samples were air-dried before being transferred to a plastic vial for further evaluation. The change in the concentration from 4 mM – 16 mM to 0.2 mM – 0.6 mM was extensively discussed in this chapter's results and discussion section. The structural properties were analyzed using Panalytical XRD, morphology and composition with TESCAN SEM and EDS, and ligament size measured using ImageJ [21].

3.3 Results and Discussion

The morphology of the 0 mM sample is present in Fig. 3.3. This sample was prepared through a standard chemical dealloying approach, using a solution of 0.5 M HF and 10 M HNO_3 at 70 °C for 4 hours. During this process, Au atoms near the alloy/electrolyte interfaces reorganized, whereas Ag and other less noble atoms were preferentially removed. 0 mM NPG will act as a reference sample to distinguish the effect of L-cysteine on the structural morphology of other NPG samples during L-cysteine-mediated chemical dealloying. Channels and unevenly distributed ligaments emerged first, subsequently developing into pores and ligaments throughout the thickness, as illustrated in Fig. 3.3 (a). The ligaments exhibit grain boundaries, frequently observable as grooves on the external surface, resulting from the impingement of separately developed crystals. The porous structure is predominantly homogeneous and uniform across the de-alloyed thickness, as illustrated in the cross-sectional image of Fig 3.3 (b).

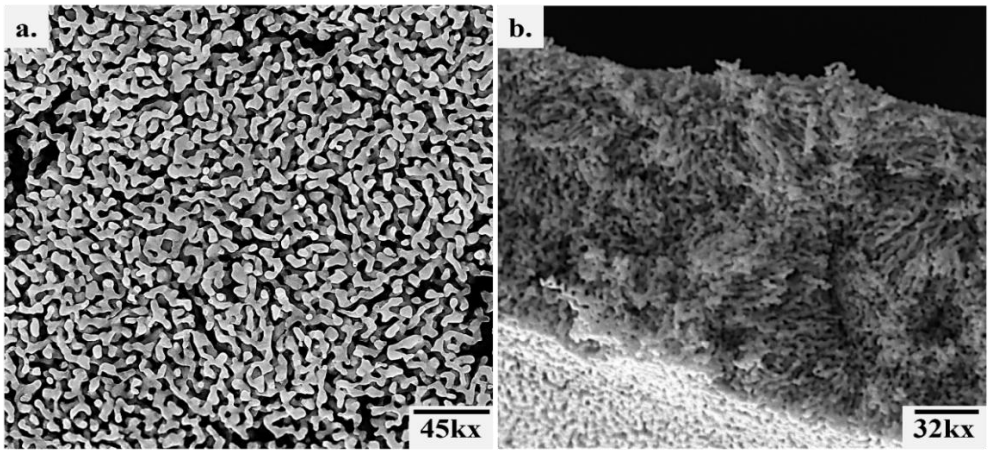

***Figure 3.3**: SEM analysis of 0 mM NPG (a) Formation of Pore and Ligament at 45 Kx magnification (b) Cross-sectional analysis of 0 mM NPG at 32 Kx magnification.*

In contrast, after the treatment, the ribbons retain their structure and can be utilized for analysis without experiencing any significant damage.A total of 250 measurements were taken to evaluate the dimensions of ligaments at their narrowest necks, with ligament sizes ranging from a minimum of 31 nm to a maximum of 132 nm. The average ligament size was found to be 73 ± 19.6 nm. After de-alloying, EDS analysis was also performed to reveal the effect of dealloying before and after the treatment, as illustrated in Fig 3.4. After dealloying, the ribbon primarily consists of Au, with diminished levels of other elements. The elemental composition includes Si at 0 at. %, Cu at 1.16 at. %, Pd at 1.14 at. %, and Ag at 0 at.%. This distribution aligns with the expected outcomes of the dealloying process.

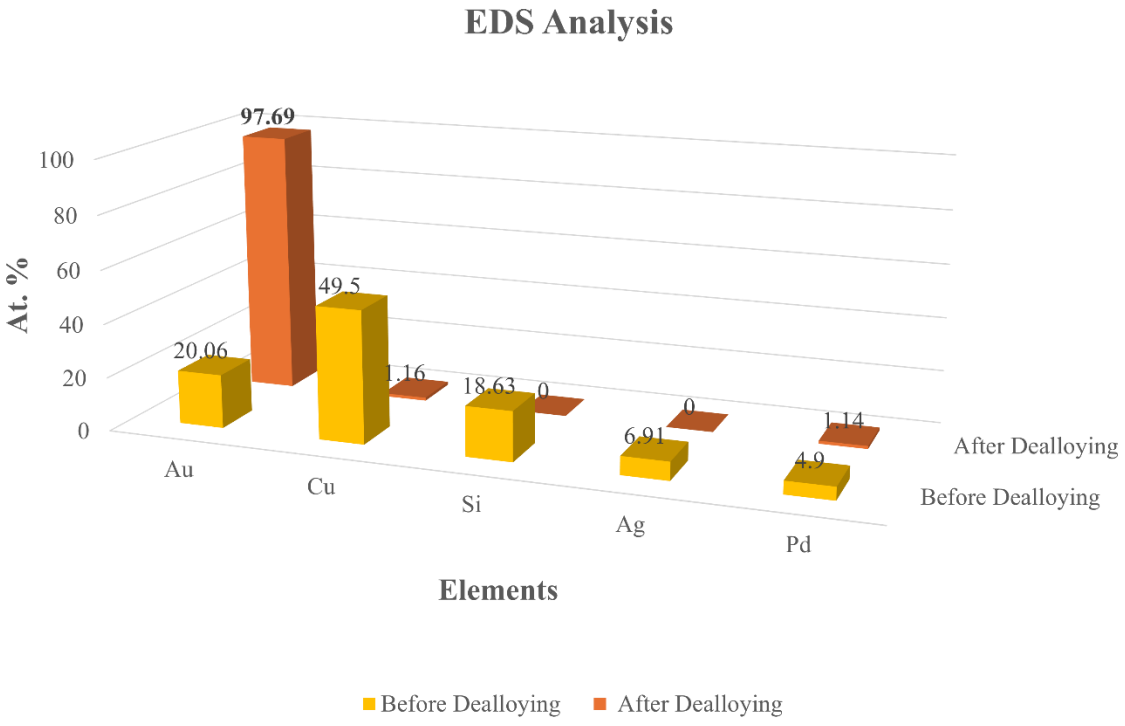

***Figure 3.4:** EDS analysis of 0 mM NPG before and after the chemical dealloying*

L-cysteine was added in an electrolyte solution of 10 M HNO_3 and 0.5 M HF to produce ultrafine NPG. Initially, 3 different concentrations of L-cysteine were selected, such as 4 mM, 8 mM, and 16 mM L-cysteine, while other experimental procedures, time and temperature, were kept constant. Henceforth, the as-synthesized sample was named 4 mM NPG, 8 mM NPG, and 16 mM NPG. The structure feature of these samples was analyzed using SEM coupled with EDS as shown in Fig. 3.5. SEM analysis indicates that the concentration of L-cysteine significantly influences the structural morphology of as-synthesized NPG.

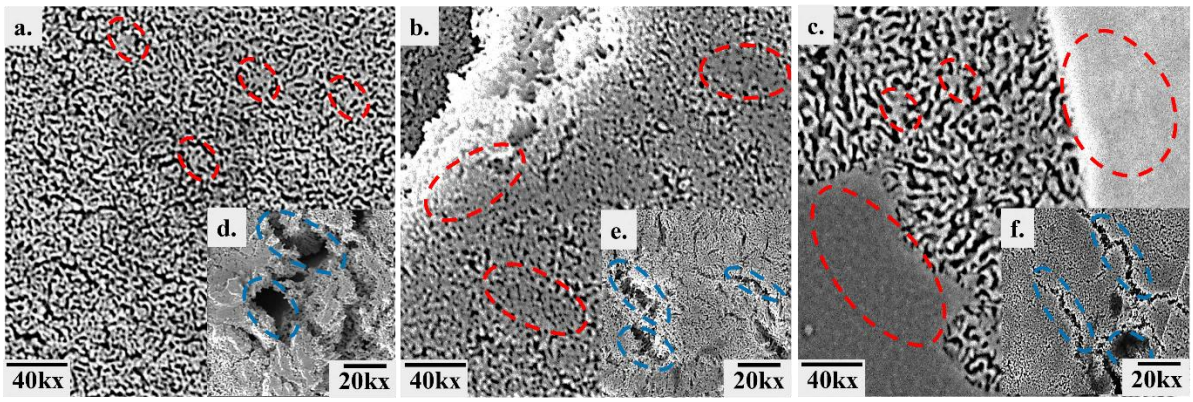

Figure 3.5: *SEM analysis of L-Cysteine modified chemical dealloying (a, d) 4 mM NPG (b. e) 8 mM NPG (c, f) 16 mM NPG.*

At the lower concentration, the 4 mM NPG reveals a pronounced formation of cracks and holes, as shown in Fig 3.5 (d), highlighted in blue. At the higher magnification Fig 3.5 (a), ligaments and pores form, but they tend to merge, as indicated by red circles. These results suggest that the L-cysteine contributes to the development of cracks and holes. As the L-cysteine concentration increased from 4 mM to 8 mM, the cracks became more prominent, resulting in an increase in surface defects, as shown in Fig. 3.5(c). At higher magnification, there is an observable accumulation of heavy mass, which might be an excess of L-cysteine stuck on the samples and suppressed the formation of ligaments and pores, as highlighted with the red lines in Fig 3.5 (b). At 16 mM NPG, the structural defect becomes more pronounced, with deeper cracks and a significant amount of L-cysteine that seem unreacted during the chemical dealloying process, as depicted in Fig 3.5 (f). Moreover, it inhibits the formation of well-defined ligaments and pores, as shown in Fig 3.5 (c). These structural features affect the functional properties of NPG, such as decreasing catalytical activity and damaging the structural integrity, leading to a less stable structure.

A cleaning process was employed to resolve this problem. The sample was subjected to an ultrasonic bath and immersed in a concentrated solution of HNO_3 for 3 to 4 minutes. After that, the samples were rinsed with Milli-Q water to remove residual L-cysteine. Additionally, acetone and isopropanol were used to clean the sample further.

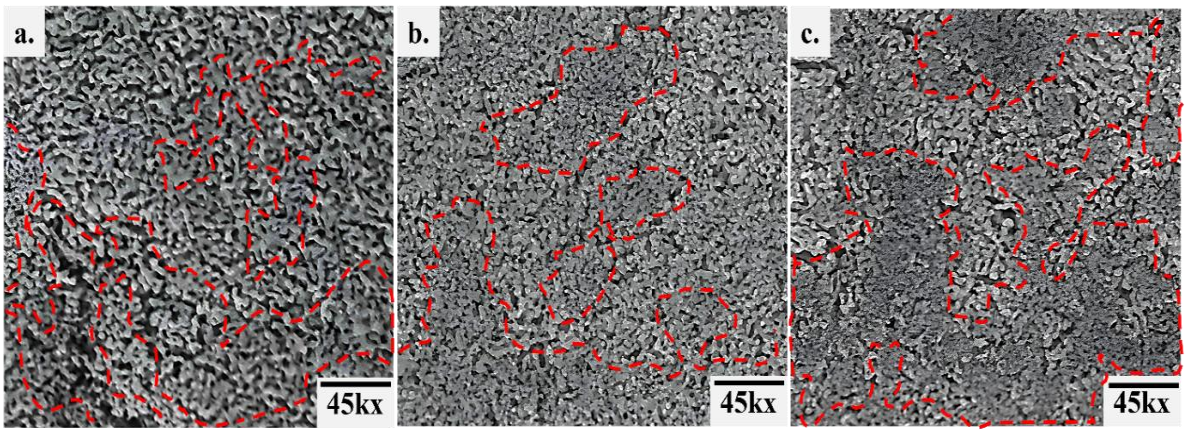

Figure 3.6: *SEM analysis of L-Cysteine modified chemical dealloying samples after the cleaning treatment (a) 4 mM NPG, (b) 8 mM NPG, and (c) 16 mM NPG.*

The SEM analysis in Fig. 3.6 indicates that although the cleaning methods show some improvement, it is still insufficient in removing L-cysteine residues, possibly due to the insufficient duration of the cleaning process. In Fig. 3.6 (a), the 4 mM NPG shows the formation of ligaments and pores, but they are not well-defined, and surface defects affect the overall morphology. Additionally, a significant amount of L-cysteine remained in 8 mM NPG and 16 mM NPG, inhibiting the formation of ligaments and pores, as demonstrated in Fig. 3.6 (b, c) by highlighting the excess L-cysteine with red lines. Liyanage et al. [3] demonstrated that L-cysteine can permanently bind to surfaces, leading to irreversible inhibition of catalytic activity and resulting in structural modifications that do not recover over time. These findings suggest that the resulting changes in the structural morphology may be permanent once high concentrations of L-cysteine are introduced. Furthermore, higher concentrations lead to increased surface irregularities and hinder the formation of a well-defined nanoporous structure due to excessive material accumulation. Therefore, optimising the concentration of L-cysteine to achieve the desired balance between structural integrity and morphological features in NPG synthesis is important.

To achieve the ultrafine feature of NPG and the ideal balance of L-cysteine, the Xiao et al. [18] work was chosen as a reference. In this study, 0.8 mM L-cysteine was used to dealloy the $Au_{25}Ag_{75}$ leaf using the chemical dealloying method, resulting in the 4 nm ligament size of NPG. Therefore, in our research, three different concentrations of L-cysteine, 0.2 mM, 0.4 mM, and 0.6 mM concentration were chosen to achieve the ultrafine structure of NPG by dealloying an amorphous ribbon $Au_{20}Cu_{48}Ag_7Pd_5Si_{20}$. The detailed procedure is discussed in this chapter's materials and methods section.

To better understand the effect of L-cysteine concentration on structural morphology, SEM analysis was carried out following the synthesis of 0.2 NPG, 0.4 NPG, and 0.8 NPG. Fig. 3.7 presents the SEM analysis of L-Cysteine-modified chemical dealloying, illustrating the structural changes at different concentrations of NPG. The 0.2 mM NPG in Fig 3.7 (a, b) revealed the formation of ligaments and pores, even at the lower magnification of 15 Kx being observable.

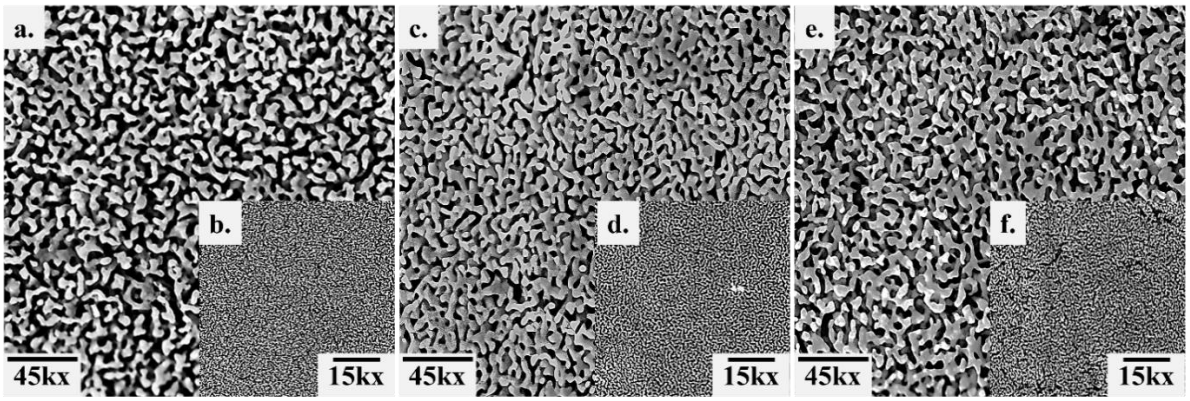

***Figure 3.7**: SEM analysis of L-Cysteine modified chemical dealloying samples after the cleaning treatment (a, b) 0.2 NPG, (c, d) 0.4 NPG, and (e, f) 0.6 NPG*

As magnification increased to 45 Kx, well-defined 3-D interconnected ligaments became apparent. In Fig. 3.7 (c, d), a clear and more refined ligament structure was observed with 0.4 mM NPG compared to the 0.2 mM NPG sample. No cracks were visible in either sample, even at lower magnification. Finally, the analysis of 0.6 mM NPG (Fig 3.7 (e, f)) displayed a significant reduction in ligament size, enhanced surface defects and some cracks compared to the other samples. These findings suggest that L-cysteine is more effective in modifying the surface morphology of NPG. In order to confirm these findings, the ligament size of as-synthesized NPG was measured at their narrow neck using 200 counts.

The results of each synthesised sample were subsequently analysed in comparison to the 0 mM NPG that acts as our reference, as illustrated in Fig. 3.8. The analysis of ligament size with varying concentrations of L-cysteine for the 0 mM NPG sample resulted in an average measurement of 73 ± 18 nm. In contrast, the 0.2 mM NPG sample exhibited an average size of 40 ± 14 nm, the 0.4 mM NPG sample showed 39 ± 15 nm, and the 0.6 mM NPG sample recorded an average size of 35 ± 13 nm. The results indicate a decrease in ligament size with an increase in the L-cysteine concentration. It is important to emphasize that the right concentration is crucial to modifying the surface morphology of nanoporous metals. Beyond a specific threshold, the formation of ligaments and pores is inhibited, as demonstrated in Fig. 3.3.

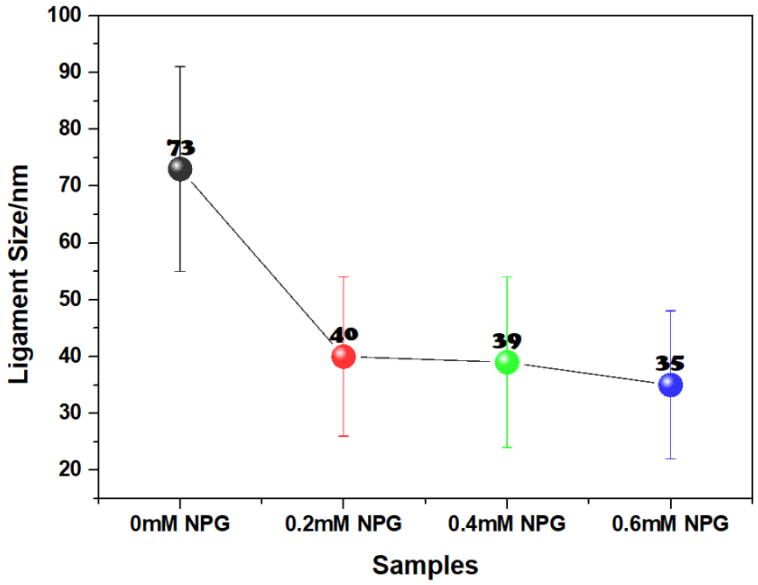

Figure 3.8: *Comparison of Ligament size using the L-cysteine-modified chemical dealloying method.*

Furthermore, the Energy Dispersive Spectroscopy (EDS) analysis was also performed, which gives valuable insight into the elemental composition of the samples before and after dealloying with different concentrations of L-cysteine. A comparative representation of 0.2 NPG, 0.4 NPG, and 0.6 NPG before and after dealloying was depicted in Fig. 3.9.

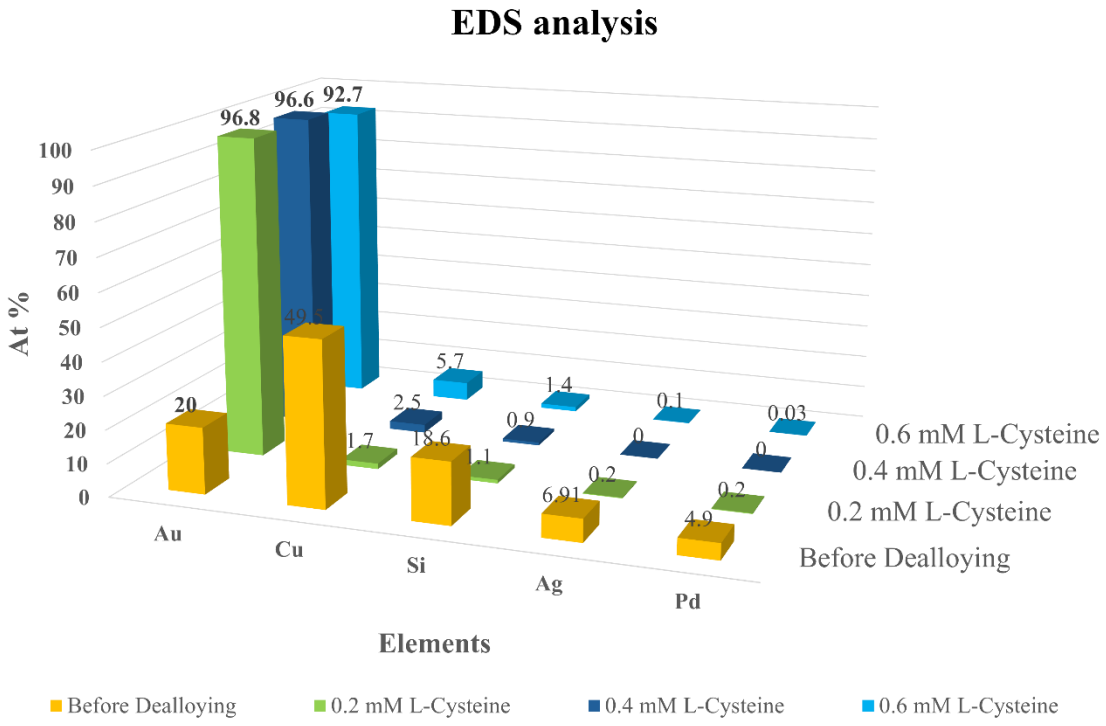

Figure 3.9*: EDS analysis before and after de-alloying using the different concentrations of L-Cysteine*

The EDS analysis revealed a substantial increase in gold content (% Au), rising from 20 to 96 after dealloying, indicating effective extraction of less noble metals. The Au conc. remained consistently high at approximately 96 to 97 atomic % across all concentrations of L-cysteine, suggesting that higher L-cysteine concentrations do not negatively impact Au retention. Following dealloying, the Cu content decreased significantly from an initial 49.5% to as low as 1.7%, 2.5%, and 5.7%. Si reduced from 18.6% to 0.9-1.4%, while Ag dropped from 6.9% to negligible amounts (0-0.2%) across all samples. Pd exhibited a similar trend, decreasing from an initial concentration of 4.9% to negligible levels (0-0.2%) after dealloying.

After obtaining structural information for the L-cysteine-modified sample, XRD analysis was performed to obtain crystallographic insights. Fig. 3.10 illustrates the XRD analysis of the amorphous ribbon and samples with 0 mM NPG, 0.2 NPG, 0.4 NPG, and 0.6 NPG. The XRD analysis revealed that as dealloying progressed. The amorphous halo's intensity decreased, revealing distinct peaks in the randomly distributed crystals of the FCC phase. All dealloyed samples displayed identical peaks with varying intensities, corresponding to the face-centered cubic Au that is in planes of 111, 200, 220, and 311 (PDF No. 04-0784). According to The Scherrer equation, $D = K\lambda/(\beta \cos \theta)$, the characteristic length scale of NPG was reduced by the L-cysteine in HNO_3 and HF solution. The mean crystallite size of 0.6 NPG was ~ 36.0 nm, whereas 0.4 NPG had ~ 40.3 nm and 0.2 NPG had ~ 43.8 nm, which were smaller than that of 0 NPG, which was ~ 49.6 nm.

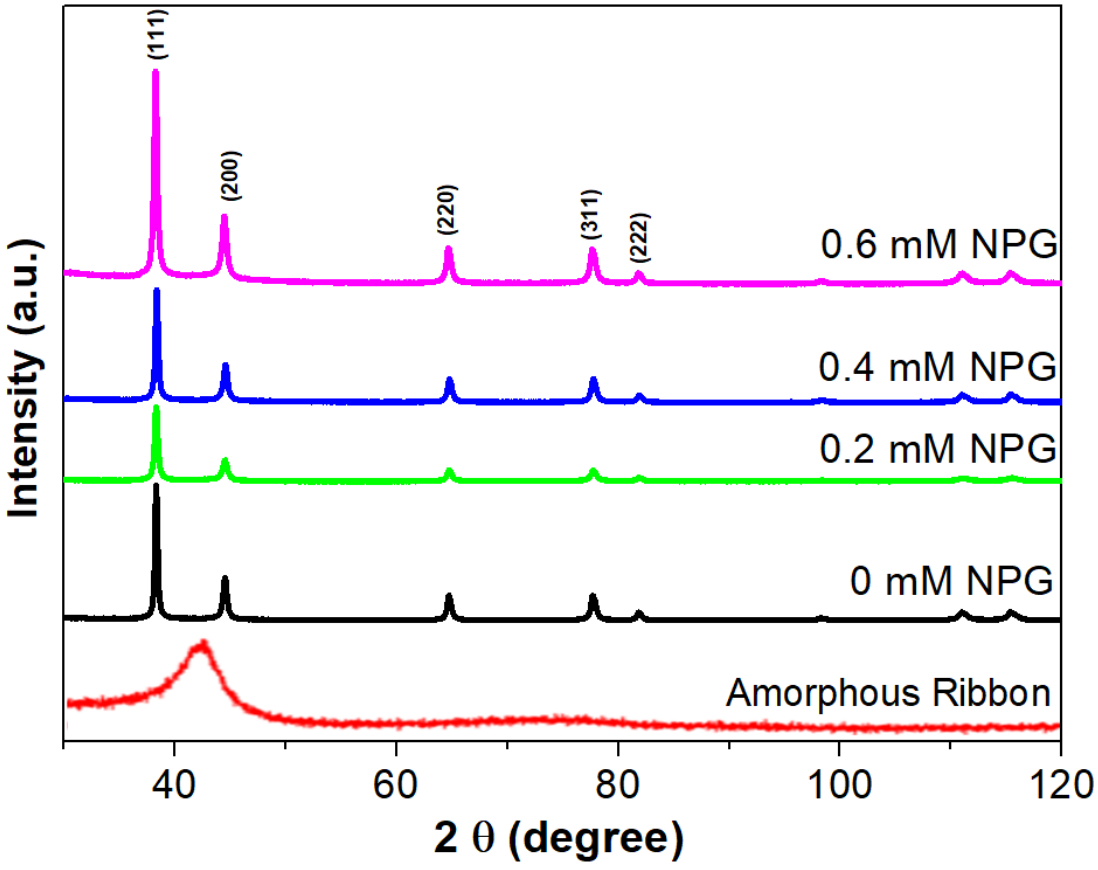

Figure 3.10: *Comparison of XRD analysis with the different conc. of L-Cysteine*

3.4 Conclusion

In conclusion, a simple and effective method of dealloying coupled with L-cysteine is presented for producing ultrafine nanoporous Au from an amorphous ribbon $Au_{20}Cu_{48}Ag_7Pd_5Si_{20}$ synthesized through arc melting. The study emphasizes the substantial impact of L-cysteine concentration on altering the structural morphology of NPG produced via chemical dealloying. The findings indicate that lower concentrations of L-cysteine 0.2 mM, 0.4 mM, and 0.6 mM promote the formation of well-defined interconnected ligaments and pores. In contrast, higher concentrations of L-cysteine, i.e. 4 mM, 8 mM and 16 mM, lead to significant surface defects and inhibit the formation of ligaments and pores to achieve the desired nanoporous structure. The cleaning process to remove residual L-cysteine proved ineffective, suggesting that high concentrations may cause irreversible changes to the NPG's morphology and catalytic properties. However, the optimal concentration for achieving ultrafine NPG structures appears to be around 0.2 mM to 0.6 mM, as evidenced by reduced ligament sizes and improved structural integrity. Additionally, EDS and XRD analyses confirm effective dealloying and crystallization, highlighting concentration optimization as important in synthesizing NPG for potential applications. This research provides valuable insights into the delicate balance required in the chemical dealloying process to achieve desired morphological and functional characteristics in nanoporous metals. The synthesis of ultrafine NPG is cost-effective and suitable for large-scale production. This method provides a simple and efficient approach to creating high-performance nanoporous metal frameworks for a variety of applications.

References

1. Fujita, T.; Guan, P.; McKenna, K.; Lang, X.; Hirata, A.; Zhang, L.; Tokunaga, T.; Arai, S.; Yamamoto, Y.; Tanaka, N.; et al. Atomic Origins of the High Catalytic Activity of Nanoporous Gold. *Nat Mater* 2012, *11*, 775–780, doi:10.1038/nmat3391.

2. Haruta, M.; Kobayashi, T.; Sano, H.; Yamada, N. Novel Gold Catalysts for the Oxidation of Carbon Monoxide at a Temperature Far below 0 C. *Chem Lett* 1987, *16*, 405–408.

3. Scaglione, F.; Rizzi, P.; Celegato, F.; Battezzati, L. Synthesis of Nanoporous Gold by Free Corrosion of an Amorphous Precursor. *J Alloys Compd* 2014, *615*, S142–S147, doi:10.1016/j.jallcom.2014.01.239.

4. Scaglione, F.; Paschalidou, E.M.; Rizzi, P.; Bordiga, S.; Battezzati, L. Nanoporous Gold Obtained from a Metallic Glass Precursor Used as Substrate for Surface-Enhanced Raman Scattering. *Philos Mag Lett* 2015, *95*, 474–482, doi:10.1080/09500839.2015.1093665.

5. Zhao, M.-C.; Shan, Y.-Y.; Xiao, F.R.; Yang, K.; Li, Y.H. Investigation on the H2S-Resistant Behaviors of Acicular Ferrite and Ultrafine Ferrite. *Mater Lett* 2002, *57*, 141–145.

6. Pickering, H.W.; Wagner, C. Electrolytic Dissolution of Binary Alloys Containing a Noble Metal. *J Electrochem Soc* 1967, *114*, 698.

7. Forty, A.J.; Rowlands, G. A Possible Model for Corrosion Pitting and Tunneling in Noble-Metal Alloys. *Philosophical Magazine A* 1981, *43*, 171–188.

8. Sieradzki, K.; Newman, R.C. Stress-Corrosion Cracking. *Journal of physics and chemistry of solids* 1987, *48*, 1101–1113.

9. Erlebacher, J.; Guest, R.S. *Hard Materials with Tunable Porosity A Brief History of Nanoporous Metals*;

10. Paschalidou, E.M.; Celegato, F.; Scaglione, F.; Rizzi, P.; Battezzati, L.; Gebert, A.; Oswald, S.; Wolff, U.; Mihaylov, L.; Spassov, T. The Mechanism of Generating Nanoporous Au by De-Alloying Amorphous Alloys. *Acta Mater* 2016, *119*, 177–183, doi:10.1016/j.actamat.2016.08.025.

11. McCue, I.; Benn, E.; Gaskey, B.; Erlebacher, J. Dealloying and Dealloyed Materials. *Annu Rev Mater Res* 2016, *46*, 263–286.

12. Lang, X.Y.; Yuan, H.T.; Iwasa, Y.; Chen, M.W. Three-Dimensional Nanoporous Gold for Electrochemical Supercapacitors. *Scr Mater* 2011, *64*, 923–926.

13. Guo, X.; Zhang, C.; Tian, Q.; Yu, D. Liquid Metals Dealloying as a General Approach for the Selective Extraction of Metals and the Fabrication of Nanoporous Metals: A Review. *Mater Today Commun* 2021, *26*, 102007.

14. Wittstock, A.; Zielasek, V.; Biener, J.; Friend, C.M.; Bäumer, M. Nanoporous Gold Catalysts for Selective Gas-Phase Oxidative Coupling of Methanol at Low Temperature. *Science (1979)* 2010, *327*, 319–322.

15. Jing, Z.; Zhang, L.; Xu, X.; Zhu, S.; Zeng, H. Carbon-Assistant Nanoporous Gold for Surface-Enhanced Raman Scattering. *Nanomaterials* 2022, *12*, doi:10.3390/nano12091455.

16. Głowniak, S.; Szczęśniak, B.; Choma, J.; Jaroniec, M. Advances in Microwave Synthesis of Nanoporous Materials. *Advanced Materials* 2021, *33*.

17. Xiao, X.; Ou, W.; Du, P.; Lyu, F.; Diao, Y.; Lu, J.; Li, Y.Y. Ultrafine Nanoporous Gold via Thiol Compound-Mediated Chemical Dealloying. *Journal of Physical Chemistry C* 2020, *124*, 10026–10031, doi:10.1021/acs.jpcc.0c01953.

18. Wang, Z.; Liu, P.; Han, J.; Cheng, C.; Ning, S.; Hirata, A.; Fujita, T.; Chen, M. Engineering the Internal Surfaces of Three-Dimensional Nanoporous Catalysts by Surfactant-Modified Dealloying. *Nat Commun* 2017, *8*, doi:10.1038/s41467-017-01085-3.

19. Lavernia, E.J.; Srivatsan, T.S. The Rapid Solidification Processing of Materials: Science, Principles, Technology, Advances, and Applications. *J Mater Sci* 2010, *45*, 287–325.

20. Scaglione, F.; Rizzi, P.; Celegato, F.; Battezzati, L. Synthesis of Nanoporous Gold by Free Corrosion of an Amorphous Precursor. *J Alloys Compd* 2014, *615*, S142–S147, doi:10.1016/j.jallcom.2014.01.239.

CHAPTER IV

Ultrasensitive Detection of the Malachite Green Isothiocyanate Utilizing Nanoporous Gold as A SERS Substrate

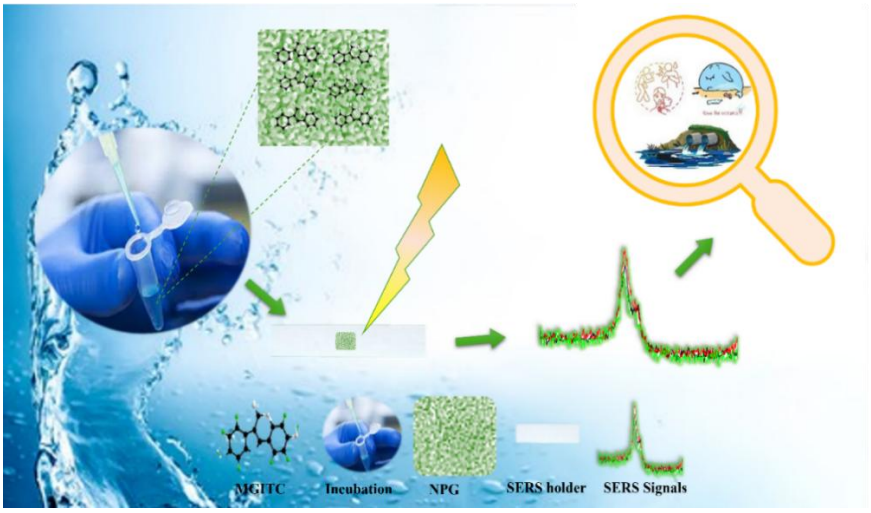

4.1 Introduction

The production of toxic emissions and waste matter has increased due to the speedy advancement of the chemical sector. The increased concentrations, number, and diversity of harmful organic and inorganic pollutants in the wastewater leads to dangerous environmental concerns [1]. The threats of carcinogenesis and pathogenesis regarding human health cannot be overlooked once these substances are emitted into environment [2–5]. In the last decade, the detection of organic pollutants has gained attention and is considered crucial in environmental safety. Organic pollutants are primarily produced in the manufacturing industries, like pharmaceuticals, food, textiles, explosives, pesticides, and synthetic dyes. One frequently used coloring agent in the textile industry is malachite green (MG),a synthetic dye known as a persistent organic pollutant in wastewater. Malachite green and isothiocyanate (MGIT), a derivative of MG is widely used as repellents and fungicides for treatment and prevention various fish infections and diseases [2,3]. Due to their complicated genotoxic properties and long degradable time, releasing these highly colored wastes severely compromises the biological environment and human health [4,5]. For these reasons, many European and other countries, like China, Japan, and the United States, have banned MG dyes or other representative triphenylmethane derivatives due to their toxic properties. The minimum required performance limit (MRPL) for the detection of MG and its derivatives is 2 μg/L (4×10^{-9} M) [6]. This threshold ensures food safety compliance, as exposure levels at or below this limit are unlikely to pose health risks.

The crucial need for identifying organic pollutants has encouraged the advancement of innovative and novel analytical methods to detect toxic organic composites from water resources. Various strategies, such as spectroscopic approaches, like mass spectrometry, infrared spectroscopy, Raman spectroscopy, UV-vis spectroscopy, and some electroanalytical

approaches, were recommended [7–10]. The techniques mentioned above have many benefits. However, they require long detection time, sophisticated equipment, and a complex separation process. Among them, SERS is a simple, sensitive, and non-destructive method. That is gradually gaining attention [11]. A detailed description of the SERS technique and its working principle is provided in Chapter II. However, to further enhance SERS performance, an efficient substrate with a larger surface area and high enhancement factor is crucial [12]. The effectiveness of the SERS sensor mainly relies on its selectivity and sensitivity [13]. Therefore, it is necessary that SERS sensors maintain a wide linear range of detection and a low detection limit [14]. Current efforts are primarily focused on forming an active substrate as a three-dimensional nano-architecture[15]. Among the different metal nano-architectures, NPG serves as an ideal substrate due to its remarkable biocompatibility, reproducibility, stability, and highly controlled, robust surface plasmon resonance [16,17]. Their presence in the nanoporous matrix increases the catalytic and plasmonic properties of the NPG. Generally, producing high-quality NPG suitable for various sensing and catalytic applications is both straightforward and effective.

Scaglione et al. [18] achieved a bimodal morphology by chemically dealloying NPG and subsequently anodizing it in oxalic acid. For 4'4-bipyridine as a probe molecule, the resulting NPG and anodized NPG (3-min) exhibited SERS enhancement factors of 2×10^{13} and 1×10^{17}, respectively, with a detection limit of 10^{-16} M. C. Awada et al. [18] studied a porous gold nanostructure in an Ag/Au system, finding that the SERS activity resulted in selective photon adsorption, achieving an enhancement factor of 10^5. Hu et al. [19] investigated the stability and enhancement of the SERS substrate by combining dealloying and magnetron sputtering to generate NPG. The resulting NPG yielded an EF of 10^7. These studies highlight that surface modifications and NPG as an active SERS substrate can significantly improve performance. The surface of NPG contains abundant active sites that enhance localized surface plasmon excitation, which is crucial in optimizing SERS performance [20]. Furthermore, a recyclable SERS substrate produced from gold-based nanostructures could increase efficiency while reducing both environmental footprint and cost [21].

To accomplish these advantages, several gold-based nanostructured SERS substrates have been developed for environmental monitoring of organic pollutants that include malachite green and its derivatives, pesticide residues, dyes, persistent organic contaminants and bisphenol A [22–26]. In the Weinan Leng experiment [21], stable suspensions of MGITC functionalized on gold nanoparticles (MGITC-AuNPs), consisting primarily of monomers and a mixture of monomer and multimer, were analyzed. SERS intensity at 785 nm and multimer concentration ratios were used to determine an enhancement factor of 2×10^3. Fu et al. [27] designed an MG-detecting SERS substrate utilizing π–π stacking interactions and electrostatic forces, achieving 2.5 μM, a minimum detectable concentration. Tan et al. [28] produced an active SERS substrate that achieved a detection limit of 1.0 pM by utilizing a 3D TiO_2 nanorod scaffold that was coated with Ag nanoparticles. However, further research is required to optimize the substrate fabrication procedure by improving the cost efficiency as well as boosting SERS performance. Consequently, in this study, an amorphous precursor, $Au_{20}Cu_{48}Ag_7Pd_5Si_{20}$, was chemically dealloyed in a solution of HNO_3 and HF at 70 ºC for 5 hours to fabricate (NPG) as an improved

SERS sensor substrate. The developed sensor demonstrates an impressively low detection limit (LOD) of 10^{-16} and a high EF of 10^9, making it as a highly efficient, sensitive and effective substrate for identifying MGITC with exceptionally low concentrations.

4.2 Materials and Methods

4.2.1 Synthesis of the Nanoporous gold

A master alloy with the composition of $Au_{20}Cu_{48}Ag_7Pd_5Si_{20}$ was produced through arc-melting of high-purity elements in a Ti-gettered argon environment using a Buehler electric arc furnace. This combination produces an amorphous alloy with superior glass-forming characteristics. Using melt-spinning, the ingot was then quickly solidified. The molten alloy was pulled onto a Cu wheel via a 2 mm nozzle revolving at 25 m/s in an argon-shielded atmosphere. This resulted in amorphous ribbons measuring 25 µm in thickness and the width is 2 mm. The newly formed Au-based ribbon was treated in a solution containing HNO_3 and HF solution with concentrations of 10 M and 0.5 M, respectively, at 70 °C for 5 hours and referred to as NPG-5h. After dealloying, the sample was thoroughly rinsed with double-distilled water, air-dried, and kept in a clean vial for future research.

The XRD configuration was used for structural analysis of the quenched ribbon and dealloyed sample. Additionally, the surface and cross-sectional features, along with composition of the NPG-5h sample were analyzed in detailed. The open-source ImageJ program [29] was used to analyze 160 ligaments at their narrowest places in order to determine the average ligament size in the NPG-5h.

4.2.2 Preparation of probe molecule solutions

The SERS performance of the NPG-5h, using MGITC as the probe molecule was evaluated. All solutions were generated using chemical-grade reagents from Sigma Aldrich and deionized water was used with a resistivity of 18 $M\Omega \cdot cm^{-1}$. A concentrated stock solution was made by precisely weighing the MGITC powder and dissolving it in 10 mL of deionized water. Subsequent dilutions were then made to achieve concentrations ranging from 10^{-16} M to 10^{-10} M.. A small section of the NPG-5h sample, about 2 cm long, was cut and placed in an Eppendorf tube. immersed in the MGITC solution for 30 minutes. The method began with the most dilute solution of 10^{-16} M, then progressed to 10^{-14} M, 10^{-12} M, and finally 10^{-10} M. The sample was removed from the solution after 30 minutes and air-dried for an additional 30 minutes in order to ensure the maximal adsorption of probe molecules onto the surface.

Once dried, the sample was positioned in the SERS sample holder for measurement. This procedure was consistently implemented for all MGITC concentrations, including 10^{-16} M, 10^{-14} M, 10^{-12} M, and 10^{-10} M. To prevent contamination, fresh Eppendorf tubes and tips were used for each concentration. The SERS investigation of the carcinogenic MGITC was performed using a SERS (Renishaw in Via Raman Microscope) equipped with a 785 nm laser line. For the detection of MGITC, a 20x long working distance objective was employed, utilizing a laser power of 0.5% and three acquisitions, each with an acquisition time of 20 s.

To investigate the SERS signal distribution, the intensity map image was also obtained on functionalized NPG-5h for all conc. The Maps were obtained on a surface area of 100 × 100 um^2, and spot-to-spot 25 Raman spectrum maps were collected across a wavelength range of 750 to 950 cm^{-1}, 0.5% laser, with an acquisition time of 20 s.

4.2.3 Data analysis

The enhancement factor of NPG-5h was determined to evaluate its SERS capability. From the SERS spectra, the peak at 827 cm^{-1}, associated with C-H skeleton bending, was selected as the representative characteristic peak [30]. The enhancement factor (EF) was calculated using **10^{-16} M** MGITC on the NPG-5h substrate, where a strong SERS signal was detected. Additionally, **10^{-8} M** MGITC was analyzed on a flat gold substrate to compare SERS enhancement at higher concentrations where signal detection is possible. The SERS EF, excited at 785 nm, is calculated as follows.

$$E.F = {}^{\text{ISERS}}/_{C\ SERS} \times {}^{C\ blank}/_{I\ blank}$$

Where I_{SERS} and I_{Blank} are the Raman intensities, i.e., NPG-5h substrate and a flat gold substrate in this study, respectively, C_{SERS} and C_{blank} imply the analyte concentrations used for the SERS substrate and flat gold substrates. Therefore, the roughly calculated EF of the NPG-5h substrate was 7.9×10^9. For the analytical chemistry, I_{SERS} = 227.52 cm^{-1} and I_{Blank} = 2.92 cm^{-1} signify the Raman intensities, and C_{SERS} =10^{-16} and C_{blank} = 10^{-8}.Chemical enhancement is further improved through through the electronic coupling between the MGITC and the NPG-5h surface, resulting in a high enhancement factor of approximately 7.9×10^9. Based on the findings previously reported by Kaminska et al. [31], the overall EF is three times higher than the acquired EF. Using the photo-etched technique, he created the SERS surface on Au-coated GaN for the purpose of his scholarly investigation. Nanoporous structures can confine electromagnetic fields, which is the reason for this remarkable result. They display an exceptionally high enhancement because they have a comparatively large specific surface area.

4.3 Results and Discussion

Scanning electron microscopy was used to examine the surface morphology and dimensions of the dealloyed NPG-5h SERS substrate Fig. 4.1 (a, b) illustrates the surface morphology and cross-sectional analysis of the NPG-5h samples. In addition to this, Fig. 4.1 a illustrates a surface structure characterized by pores and ligaments, while Fig. 4.1 b displays interconnected three-dimensional channels throughout the ribbon's thickness. Fig. 4.1 c demonstrates the distribution of ligament sizes on the sample's surface, with multigrain ligaments measured at the narrower necks, ranging from 35 to 80 nm, and an average diameter of around 65 ± 7.5 nm for NPG-5h.

The creation of an amorphous ribbon as a result of the melt-spinning technique and a crystalline system as a result of the dealloying process were both successfully validated through the use of XRD studies. A single enlarged halo can be seen in the diffractogram of the amorphous precursor, which is depicted in red in Fig. 4.1 d. This demonstrates that there are no crystalline

planes within the sample that are capable of obeying Bragg's law and, as a result, producing diffraction. In comparison, the diffractogram for NPG-5h (shown in black) clearly shows the change from the precursor's amorphous phase to a crystalline phase. This shift is evident by the appearance of characteristic face-centered cubic (fcc) peaks, indicative of an Au-rich solid solution.

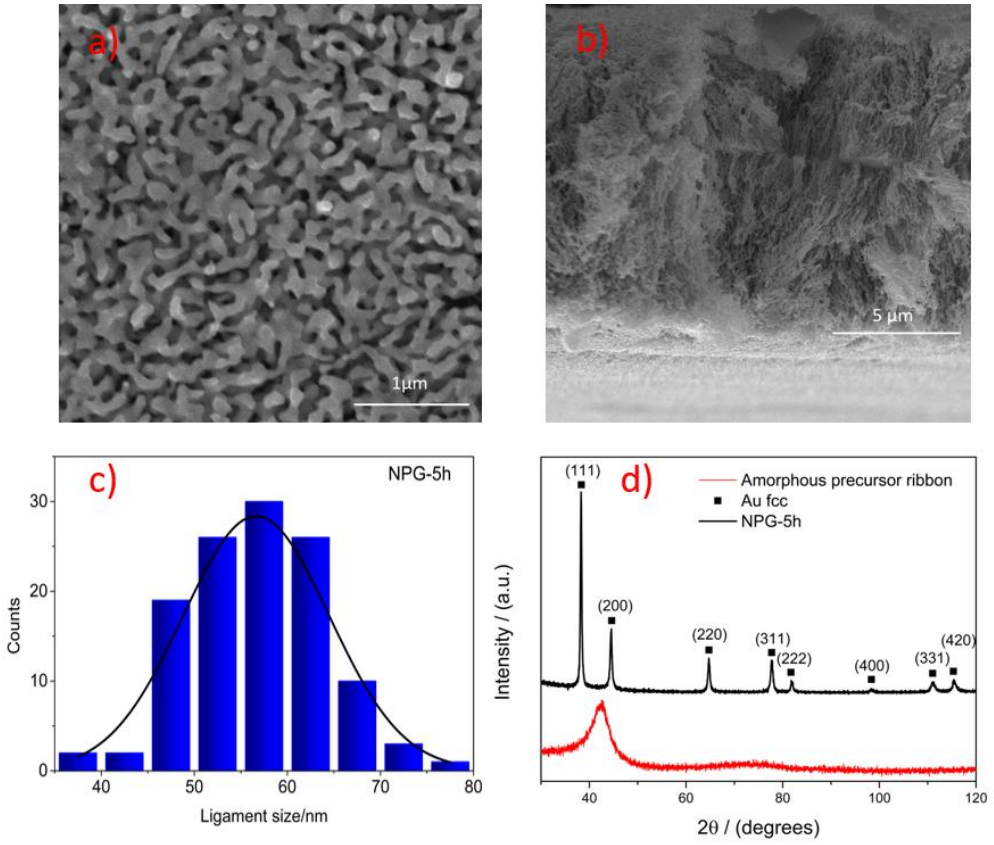

***Figure 4.1**: showing the SEM images of the NPG-5h sample: a) top surface view of NPG-5h, b) cross-sectional view of NPG-5h, c) ligament size distribution|, d) XRD spectra of NPG-5h along with the amorphous precursor ribbon.*

The EDS analysis, also shown in Table 4.1, shows that gold is the predominant component, with only small quantities of other elements present. These components are composed of 0.1 at. % Ag, 1.0 at. % Si, 0.3 at. % Pd, and 5.3 at.% copper. According to the dealloying procedure, these remaining elements are predicted to persist in the Au ligaments as part of a solid solution.

At. %	Si	Cu	Pd	Ag	Au
Mean	1.0	5.3	0.3	0.1	93.3
SD	0.1	0.2	0.2	0.1	0.2

***Table 4.1**: EDS analysis of NPG-5h*

4.3.1 SERS analysis

A SERS analysis was conducted to evaluate the sensitivity of NPG-5h in detecting MGITC. The SERS response of the NPG-5h substrate was measured across varying MGITC concentrations of 10^{-16} M, 10^{-14} M, 10^{-12} M, and 10^{-10} M. Fig. 4.2 a illustrates the spectra collected for these concentrations within the range of 750 cm^{-1} to 950 cm^{-1}, including a comparison with the standard Raman spectra of MGITC. The most prominent SERS peak was observed at 827 cm^{-1}, which aligns with previous studies [30] showing a high-intensity peak around 806 cm^{-1}, corresponding to the out-of-plane bending of aromatic hydrogen. Interestingly, there are some differences between the obtained MGITC spectrum and those reported in the literature [32,33]. These variations likely stem from intrinsic chemical and structural differences in substrates, which can affect SERS outcomes. Additionally, factors such as sample preparation, laser power, spot size, and detector settings during measurement can influence SERS signals [34].

The SERS intensity of MGITC on the NPG-5h substrate increased with higher concentrations, ranging from 10^{-14} M to 10^{-10} M, as illustrated in Fig. 4.2 a. At 10^{-14} M, a distinct signal is detected, while at the lower concentration of 10^{-16} M, the peaks are still visible but appear more subdued. Based on these results, the detection limit (LOD) for MGITC on the NPG-5h substrate was determined to be 10^{-16} M, as shown in Fig. 4.2 a. Fig. 4.2 b (inset of Fig. 4.2 a) shows SERS signals from four different spots on the substrate's surface after exposure to 10^{-12} M MGITC, demonstrating consistent peak intensities across all points. This uniformity highlights the reproducibility of the signal and the reliable performance of the SERS substrate. The enhancement factor (EF) was calculated to be approximately 7.9×10^{9}.

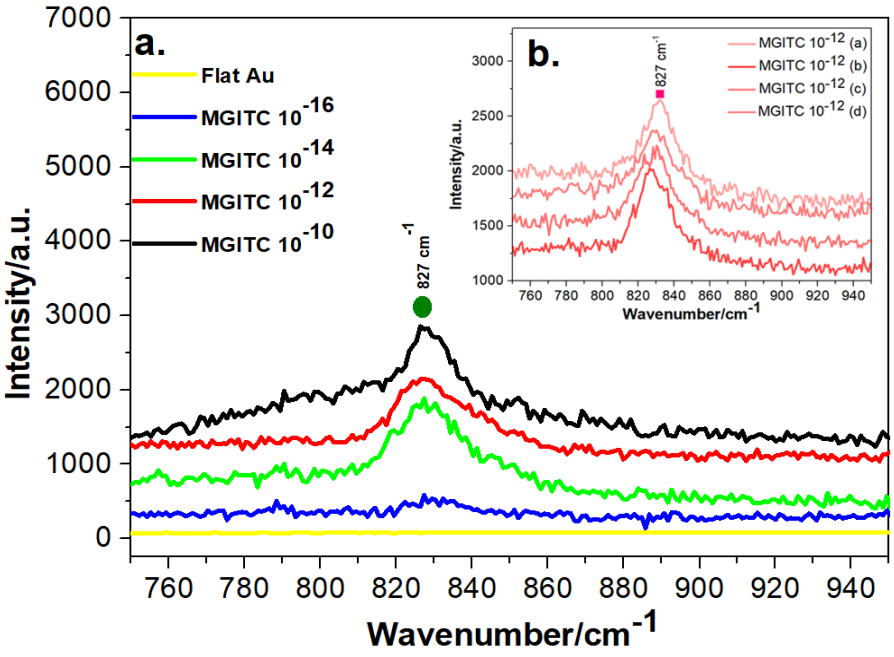

***Figure 4.2**: the SERS spectra for MGITC obtained in different concentrations ranging from 10^{-10} M, 10^{-12} M, 10^{-14} M, and 10^{-16} M was shown in a) and the in-set of MGITC 10^{-12} M represent 4 spot to spot spectrum was shown in b).*

The experimental results suggest that the NPG-5h substrate shows exceptional sensitivity and efficiency in the SERS detection of MGITC, offering a potential method for identifying MGITC in wastewater and supporting environmental protection efforts. A mapping was performed for each concentration to examine the influence of MGITC concentration on the SERS signal and substrate uniformity, collecting SERS signals from 25 points within a 100 µm × 100 µm grid. The intensity of the characteristic signal at 827 cm^{-1} is represented on a color scale in the maps shown in Fig. 4.3. Differences in relative intensity across various MGITC concentrations highlight a consistent interaction between the molecules and the NPG-5h surface, as illustrated in Fig. 4.3.

In Fig. 4.3 a, the MGITC concentration of 10^{-16} M is depicted, where the dark blue-violet color indicates a uniform substrate response even when the analyte is highly diluted, with only a limited number of molecules under the laser spot. As supported by literature, increasing MGITC concentrations gradually saturate most, if not all, of the SERS hot spots on the NPG ligaments. Once these active sites are fully occupied, any additional molecules that remain unbound or are near the surface contribute only minimally to the SERS signal, resulting in a plateau in signal intensity [35]. This effect is seen in the map in Fig. 4.3b, which shows significant SERS signals at a 10^{-14} M MGITC concentration, indicating that the substrate surface is nearly fully populated with MGITC, resulting in strong SERS responses. As concentration levels are further increased, specifically at 10^{-12} M and 10^{-10} M, the active sites become more saturated, causing a reduction in intensity relative to the previous concentration, as shown in Fig. 4.3c, d. Although it remains stronger than at lower concentrations. Random hot spots can enhance the signal, as seen in the upper right region of Fig. 4.3 d.

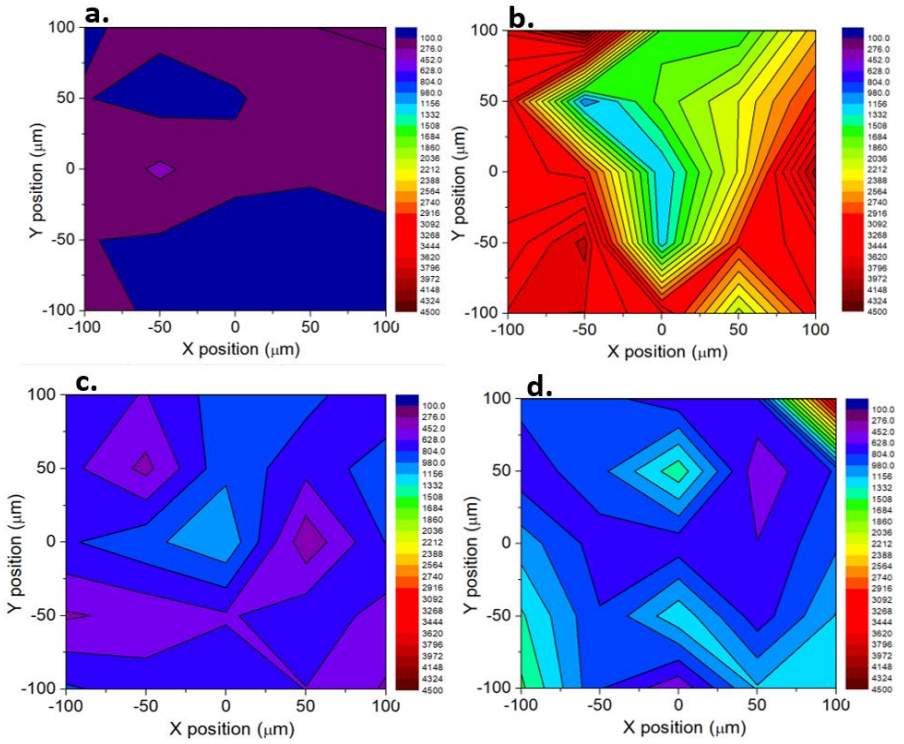

Figure 4.3. *SERS mapping of MGITC on a 100 × 100 µm² area using NPG-5h as the substrate: (a) 10^{-16} M, (b) 10^{-14} M, (c) 10^{-12} M, and (d) 10^{-10} M concentrations of MGITC.*

The intensity values obtained from the maps are displayed as mean ± SE relative to concentration in Fig. 4.4. In the saturation region, the molecules fully occupied all available active sites on the surface. The signal remains stable despite arbitrarily distributed hot patches that could potentially impact the mean value. Molecules gradually occupy the quantification region's surface because of the elevated concentration.

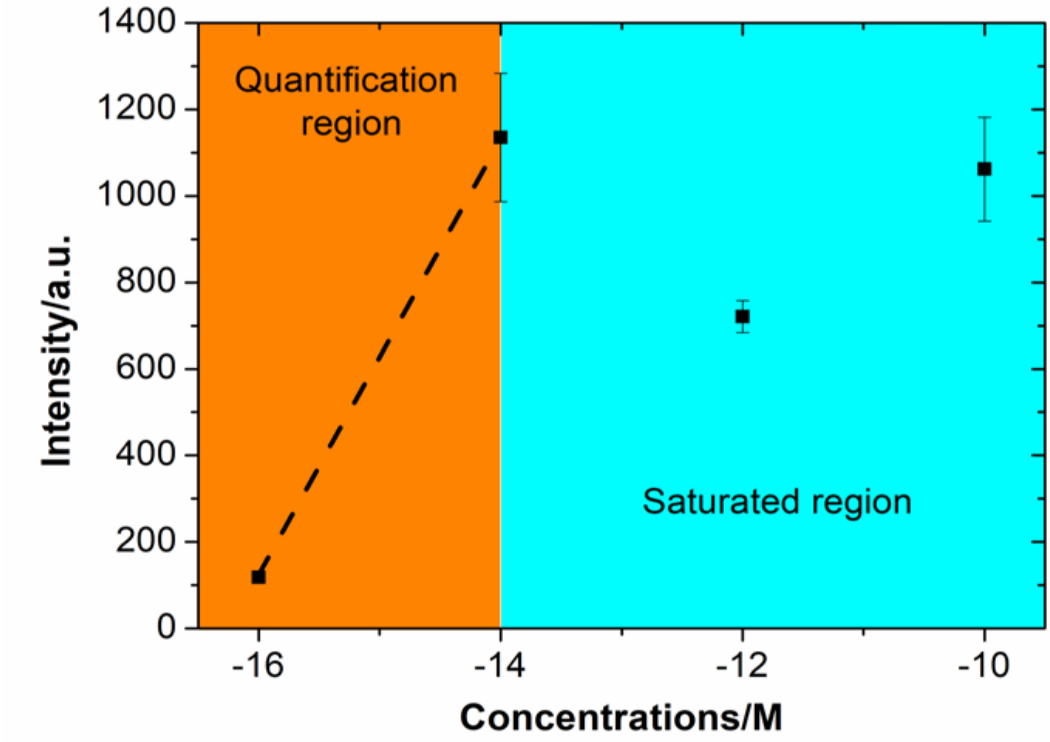

Figure 4.4: *Intensity vs. concentration graph: cyan highlights the saturated region, orange marks the quantification region, and the dashed line serves as a visual reference.*

The reproducibility of the NPG-5h substrate was validated by conducting the experiments in triplicate, with each trial involving a new sample and a freshly prepared solution. In the first two trials, measurements were taken from random points on the surface, while in the third trial, a mapping technique was employed to generate a surface map.

The detection limits (LOD) and EF of MGITC using NPG-5h as the SERS substrate were then compared to those of other substrates documented in the literature. Li et al. [36] developed a self-assembled plasmonic Au@Ag heterogeneous nano-cuboid (Au@Ag NC) sensor for SERS, achieving a detection limit of 8.7×10^{-10} M with MG as the target molecule. Chen et al. [37] fabricated a highly sensitive and recyclable SERS substrate by electrostatically assembling an organic framework material (MIL-100(Fe)) with Au nanoparticles (AuNPs), achieving a detection limit of 10^{-13} M for MG and an EF of 7.67×10^{7}.

Huang et al. [38] introduced a nanostructured SERS substrate comprising a silicon pyramid array coated with a nanostructured gold film (AuNS@SiPA), reaching a detection limit of 0.01 nM and an EF of 4.05×10^{8} for MG detection. Xu et al. [39] developed a system for detecting MG in aquaculture water by dispersing Ag nanoparticles onto Au electrodes, which under

optimized conditions achieved a detection limit of 2.4×10^{-16} M. Qiu et al. [40] employed a NPG disk as a substrate for MG detection, obtaining an EF of 5.4×10^{8} and a detection limit of 5 nM. Cheng et al. [41] explored a substrate created by self-assembling negatively charged AuNPs with positively charged covalent organic frameworks (COFs), achieving a detection limit of 6.2×10^{-10} M and an EF of 5.3×10^{5}.

Wang et al. [42] investigated MG detection on Ag nanodendrite (AgND) substrates produced via cyclic voltammetry electrodeposition on indium tin oxide, achieving a detection limit of 9.4×10^{-13} M and an EF of 5.4×10^{9}. Zi et al. [43] created Fe_3O_4 composite nanospheres coated with Au nanoparticles (Fe_3O_4@AuMCS) as a SERS substrate, with an LOD of 10^{-7} M and an EF of approximately 1.10×10^{5}. Kaminska et al. [31] produced a GaN SERS surface coated with Au via photo-etching, resulting in an EF of 2.8×10^{6} for MG. This study highlights that the NPG-5h substrate achieves an impressively low detection limit of 10^{-16} M, along with an EF of 7.9×10^{9}. When compared with various substrates in the literature, as summarized in Table 4.2, NPG-5h demonstrates the highest performance in terms of both LOD and EF.

Table 4.2. *Comparison of the SERS efficiency of different substrates in detecting MGITC.*

SERS Substrate	(LOD)	Methods	(EF)	Ref.
Au@Ag NCs	8.7×10^{-10} M	SMG	-------	[36]
MIL-100(Fe)/Au	10^{-13} M	ST & EA	7.67×10^{7}	[37]
Au NS @ SiPA	1.0×10^{-11} M	WE	4.05×10^{8}	[38]
Ag NPs	2.4×10^{-16} M	EP	-------	[39]
NPG disk	10^{-11} M	NSL	5.49×10^{8}	[40]
COF-AuNPs	6.2×10^{-10} M	EA	5.3×10^{5}	[41]
Ag NDs	4×10^{-13} M.	ED	5.4×10^{9}	[42]
Fe_3O_4@Au MCS	10^{-7} M	SMG & IR	1.1×10^{5}	[43]
Au-GaN	-------	PE	2.8×10^{6}	[31]
GO-AuNPs	2.5×10^{-6} M	RE	3.8×10^{3}	[27]
(Ag/TiO_2)	1×10^{-12} M	FTO	4.36×10^{5}	[28]
NPG-5h	10^{-16} M	CD	7.9×10^{9}	This work

CD: Process involving chemical dealloying, ED: Method of electrodeposition, PE: Technique for photo-etching, RE: Reduction-based synthesis, FTO: Fluorine-doped tin oxide material, COF: Frameworks with covalent organic bonds, NDs: Structures referred to as nanodendrites, MCS: Magnetic nanospheres with composite structures, MIL-100(Fe): A type of metal-organic framework, GO-AuNPs: Hybrids combining graphene oxide with gold nanoparticles, NPs: Structures made up of nanoparticles, NCs: Nanocuboids with heterogeneous properties, NPG: Porous gold at the nanoscale, NS: Clusters formed at the nanoscale, NDa: Arrays structured as nanodomes, SiPA: Pyramid arrays made from silicon, NSL: Lithography using nanospheres, (Ag/TiO_2): 3D scaffold of TiO_2 nanorods coated with silver particles, ST: Thermal synthesis in a solvent-based environment, EA: Electrostatic assembly and interaction, SMG: Growth mediated by seeds, IR: Iterative chemical reduction, WE: Etching process using wet techniques, EP: Preconcentration achieved through electrochemical methods.

The remarkable SERS enhancement observed in NPG-5h can be attributed to its nanoporous structure, which creates numerous SERS-active sites likely linked to grain boundaries and surface defects, thereby facilitating the localized surface plasmon resonance (LSPR) phenomenon. Furthermore, the creation of hotspots, due to the large curvatures of the nano-sized ligaments and the electromagnetic coupling in the ligaments, also improved LSPR [44–46]. Our findings show that the NPG-5h substrate is very effective for SERS detection of MGITC. A limit of 2 μg/L (4×10^{-9} M) for MGITC in wastewater was set according to the environmental regulations in many industrialized countries. Our synthesized NPG-5h demonstrates significant potential for improving pollution monitoring. Its ability to detect MGITC at extremely low concentrations highlights its suitability for real-world environmental applications.

4.4 Conclusions

In conclusion, the NPG-5h was synthesized via a chemical dealloying approach, resulting in a simple and fast production method. The synthesized NPG-5h serves as an active SERS substrate for ultrasensitive MGITC detection. The NPG-5h sample demonstrates exceptional sensitivity and selectivity in SERS, attributed to the LSPR phenomenon along with its nanosized pores and ligaments. The interconnected ligaments have an average size of 65.0 ± 7.5 nm. The SERS analysis indicates a high EF of 7.9×10^9 and LOD of 10^{-16} M was achieved via the NPG-5h sample. The obtained LOD is in accordance with the regulatory standards set by EU. The determined limit of detection meets EU regulatory criteria. The findings of the SERS investigation performed on the NPG 5h substrate show that it is a rapid detection method for MGITC. This presents new prospects for developing ultrasensitive detection of toxic effluents.

References

1. Vigneshwaran, S.; Sirajudheen, P.; Karthikeyan, P.; Meenakshi, S. Fabrication of Sulfur-Doped Biochar Derived from Tapioca Peel Waste with Superior Adsorption Performance for the Removal of Malachite Green and Rhodamine B Dyes. *Surfaces and Interfaces* **2021**, *23*, 100920.
2. Plakas, S.M.; Doerge, D.R.; Turnipseed, S.B. Disposition and Metabolism of Malachite Green and Other Therapeutic Dyes in Fish. *Xenobiotics in fish* **1999**, 149–166.
3. Culp, S.J.; Beland, F.A. Malachite Green: A Toxicological Review. *J Am Coll Toxicol* **1996**, *15*, 219–238.
4. Thetford, D.; Staff, U. by Triphenylmethane and Related Dyes. *Kirk-Othmer Encyclopedia of Chemical Technology* **2000**, 1–19.
5. Yang, M.-C.; Fang, J.-M.; Kuo, T.-F.; Wang, D.-M.; Huang, Y.-L.; Liu, L.-Y.; Chen, P.-H.; Chang, T.-H. Production of Antibodies for Selective Detection of Malachite Green and the Related Triphenylmethane Dyes in Fish and Fishpond Water. *J Agric Food Chem* **2007**, *55*, 8851–8856.
6. Stead, S.L.; Ashwin, H.; Johnston, B.H.; Dallas, A.; Kazakov, S.A.; Tarbin, J.A.; Sharman, M.; Kay, J.; Keely, B.J. An RNA-Aptamer-Based Assay for the Detection and Analysis of Malachite Green and Leucomalachite Green Residues in Fish Tissue. *Anal Chem* **2010**, *82*, 2652–2660.
7. Xu, C.; Wang, J.; Wan, L.; Lin, J.; Wang, X. Microwave-Assisted Covalent Modification of Graphene Nanosheets with Hydroxypropyl-β-Cyclodextrin and Its Electrochemical Detection of Phenolic Organic Pollutants. *J Mater Chem* **2011**, *21*, 10463–10471.
8. Carstea, E.M.; Bridgeman, J.; Baker, A.; Reynolds, D.M. Fluorescence Spectroscopy for Wastewater Monitoring: A Review. *Water Res* **2016**, *95*, 205–219.
9. De Souza, D.; Machado, S.A.S. Electrochemical Detection of the Herbicide Paraquat in Natural Water and Citric Fruit Juices Using Microelectrodes. *Anal Chim Acta* **2005**, *546*, 85–91.
10. Alvarez-Puebla, R.A.; Liz-Marzan, L.M. Environmental Applications of Plasmon Assisted Raman Scattering. *Energy Environ Sci* **2010**, *3*, 1011–1017.
11. Chen, W.; Yu, H.-Q. Advances in the Characterization and Monitoring of Natural Organic Matter Using Spectroscopic Approaches. *Water Res* **2021**, *190*, 116759.
12. Meng, X.; Qiu, L.; Xi, G.; Wang, X.; Guo, L. Smart Design of High-performance Surface-enhanced Raman Scattering Substrates. *SmartMat* **2021**, *2*, 466–487.
13. Bell, S.E.J.; Charron, G.; Cortés, E.; Kneipp, J.; de la Chapelle, M.L.; Langer, J.; Procházka, M.; Tran, V.; Schlücker, S. Towards Reliable and Quantitative Surface-enhanced Raman Scattering (SERS): From Key Parameters to Good Analytical Practice. *Angewandte Chemie International Edition* **2020**, *59*, 5454–5462.

14. Yuan, K.; Jurado-Sánchez, B.; Escarpa, A. Nanomaterials Meet Surface-Enhanced Raman Scattering towards Enhanced Clinical Diagnosis: A Review. *J Nanobiotechnology* **2022**, *20*, 1–28.

15. Qian, L.H.; Yan, X.Q.; Fujita, T.; Inoue, A.; Chen, M.W. Surface Enhanced Raman Scattering of Nanoporous Gold: Smaller Pore Sizes Stronger Enhancements. *Appl Phys Lett* **2007**, *90*, doi:10.1063/1.2722199.

16. Paschalidou, E.M.; Celegato, F.; Scaglione, F.; Rizzi, P.; Battezzati, L.; Gebert, A.; Oswald, S.; Wolff, U.; Mihaylov, L.; Spassov, T. The Mechanism of Generating Nanoporous Au by De-Alloying Amorphous Alloys. *Acta Mater* **2016**, *119*, 177–183, doi:10.1016/j.actamat.2016.08.025.

17. Rizzi, P.; Scaglione, F.; Battezzati, L. Nanoporous Gold by Dealloying of an Amorphous Precursor. *J Alloys Compd* **2014**, *586*, S117–S120.

18. Scaglione, F.; Battezzati, L.; Rizzi, P. Breaking Down SERS Detection Limit: Engineering of a Nanoporous Platform for High Sensing and Technology. *Nanomaterials* **2022**, *12*, doi:10.3390/nano12101737.

19. Huang, J.; Liu, Y.; He, X.; Tang, C.; Du, K.; He, Z. Gradient Nanoporous Gold: A Novel Surface-Enhanced Raman Scattering Substrate. *RSC Adv* **2017**, *7*, 15747–15753, doi:10.1039/c6ra28591k.

20. Li, W.; Ma, C.; Zhang, L.; Chen, B.; Chen, L.; Zeng, H. Tuning Localized Surface Plasmon Resonance of Nanoporous Gold with a Silica Shell for Surface Enhanced Raman Scattering. *Nanomaterials* **2019**, *9*, 251.

21. Scaglione, F.; Alladio, E.; Damin, A.; Turci, F.; Baggiani, C.; Giovannoli, C.; Bordiga, S.; Battezzati, L.; Rizzi, P. Functionalized Nanoporous Gold as a New Biosensor Platform for Ultra-Low Quantitative Detection of Human Serum Albumin. *Sens Actuators B Chem* **2019**, *288*, 460–468.

22. Li, X.; Chen, G.; Yang, L.; Jin, Z.; Liu, J. Multifunctional Au-coated TiO2 Nanotube Arrays as Recyclable SERS Substrates for Multifold Organic Pollutants Detection. *Adv Funct Mater* **2010**, *20*, 2815–2824.

23. Tan, M.J.; Hong, Z.-Y.; Chang, M.-H.; Liu, C.-C.; Cheng, H.-F.; Loh, X.J.; Chen, C.-H.; Liao, C.-D.; Kong, K.V. Metal Carbonyl-Gold Nanoparticle Conjugates for Highly Sensitive SERS Detection of Organophosphorus Pesticides. *Biosens Bioelectron* **2017**, *96*, 167–172.

24. Quyen, T.T.B.; Chang, C.-C.; Su, W.-N.; Uen, Y.-H.; Pan, C.-J.; Liu, J.-Y.; Rick, J.; Lin, K.-Y.; Hwang, B.-J. Self-Focusing Au@ SiO 2 Nanorods with Rhodamine 6G as Highly Sensitive SERS Substrate for Carcinoembryonic Antigen Detection. *J Mater Chem B* **2014**, *2*, 629–636.

25. Ekmen, E.; Bilici, M.; Turan, E.; Tamer, U.; Zengin, A. Surface Molecularly-Imprinted Magnetic Nanoparticles Coupled with SERS Sensing Platform for Selective Detection of Malachite Green. *Sens Actuators B Chem* **2020**, *325*, 128787.

26. Chung, E.; Jeon, J.; Yu, J.; Lee, C.; Choo, J. Surface-Enhanced Raman Scattering Aptasensor for Ultrasensitive Trace Analysis of Bisphenol A. *Biosens Bioelectron* **2015**, *64*, 560–565.

27. Fu, W.L.; Zhen, S.J.; Huang, C.Z. One-Pot Green Synthesis of Graphene Oxide/Gold Nanocomposites as SERS Substrates for Malachite Green Detection. *Analyst* **2013**, *138*, 3075–3081.

28. En-Zhong, T.; Peng-Gang, Y.; Ting-ting, Y.; Hua, W.; Lin, G. Three Dimensional Design of Large-Scale TiO2 Nanorods Scaffold Decorated by Silver Nanoparticles as SERS Sensor for Ultrasensitive Malachite Green Detection. **2012**.

29. Scaglione, F.; Rizzi, P.; Celegato, F.; Battezzati, L. Synthesis of Nanoporous Gold by Free Corrosion of an Amorphous Precursor. *J Alloys Compd* **2014**, *615*, S142–S147, doi:10.1016/j.jallcom.2014.01.239.

30. Kamińska, A.; Sivanesan, A.; Witkowska, E.; Gołąb, J.; Winiarska, M.; Nowis, D.; Dzięcielewski, I.; Weyher, J.L.; Waluk, J. *Detection of DNA Mutations Using Novel SERS (Surface-Enhanced Raman Spectroscopy) Diagnostic Platform*; 2013; Vol. 7;.

31. Kamińska, A.; Dzicielewski, I.; Weyher, J.L.; Waluk, J.; Gawinkowski, S.; Sashuk, V.; Fiałkowski, M.; Sawicka, M.; Suski, T.; Porowski, S.; et al. Highly Reproducible, Stable and Multiply Regenerated Surface-Enhanced Raman Scattering Substrate for Biomedical Applications. *J Mater Chem* **2011**, *21*, 8662–8669, doi:10.1039/c0jm03336g.

32. Qin, M.; Wang, C.; Zhu, J.; Yong, L.; Wang, H.; Yang, L. Synthesis of Differently Sized Gold Nanoparticles for SERS Applications in the Detection of Malachite Green. *Spectroscopy* **2021**, *36*, 41–46, 54.

33. Pérez-Gregorio, M.R.; González-Barreiro, C.; Rial-Otero, R.; Simal-Gándara, J. Comparison of Sanitizing Technologies on the Quality Appearance and Antioxidant Levels in Onion Slices. *Food Control* **2011**, *22*, 2052–2058.

34. Zong, C.; Xu, M.; Xu, L.J.; Wei, T.; Ma, X.; Zheng, X.S.; Hu, R.; Ren, B. Surface-Enhanced Raman Spectroscopy for Bioanalysis: Reliability and Challenges. *Chem Rev* 2018, *118*, 4946–4980.

35. Yang, S.; Dai, X.; Stogin, B.B.; Wong, T.S. Ultrasensitive Surface-Enhanced Raman Scattering Detection in Common Fluids. *Proc Natl Acad Sci U S A* **2016**, *113*, 268–273, doi:10.1073/pnas.1518980113.

36. Li, J.; Wang, Q.; Wang, J.; Li, M.; Zhang, X.; Luan, L.; Li, P.; Xu, W. Quantitative SERS Sensor Based on Self-Assembled Au@ Ag Heterogeneous Nanocuboids Monolayer

with High Enhancement Factor for Practical Quantitative Detection. *Anal Bioanal Chem* **2021**, *413*, 4207–4215.

37. Chen, M.; Huang, Y.; Miao, J.; Fan, Y.; Lai, K. A Highly Sensitive Surface-Enhanced Raman Scattering Sensor with MIL-100 (Fe)/Au Composites for Detection of Malachite Green in Fish Pond Water. *Spectrochim Acta A Mol Biomol Spectrosc* **2023**, 122432.

38. Huang, C.-Y.; Chien, C.-H. Facile Fabrication of Micro/Nano Hierarchical SERS Sensor via Anisotropic Etching and Electrochemical Treatment for Malachite Green Detection. *Applied Sciences* **2019**, *9*, 5237.

39. Xu, K.X.; Guo, M.H.; Huang, Y.P.; Li, X.D.; Sun, J.J. Rapid and Sensitive Detection of Malachite Green in Aquaculture Water by Electrochemical Preconcentration and Surface-Enhanced Raman Scattering. *Talanta* **2018**, *180*, 383–388, doi:10.1016/j.talanta.2017.12.079.

40. Qiu, S.; Zhao, F.; Zenasni, O.; Li, J.; Shih, W.C. Nanoporous Gold Disks Functionalized with Stabilized G-Quadruplex Moieties for Sensing Small Molecules. *ACS Appl Mater Interfaces* **2016**, *8*, 29968–29976, doi:10.1021/acsami.6b09767.

41. Cheng, Y.; Ding, Y.; Chen, J.; Xu, W.; Wang, W.; Xu, S. Au Nanoparticles Decorated Covalent Organic Framework Composite for SERS Analyses of Malachite Green and Thiram Residues in Foods. *Spectrochim Acta A Mol Biomol Spectrosc* **2022**, *281*, 121644.

42. Wang, R.; Zhang, L.; Zou, S.; Zhang, H. Electrodeposition of Ag Nanodendrites SERS Substrates for Detection of Malachite Green. *Microchemical Journal* **2019**, *150*, doi:10.1016/j.microc.2019.104127.

43. Li, Z.H.; Bai, J.H.; Zhang, X.; Lv, J.M.; Fan, C.S.; Zhao, Y.M.; Wu, Z.L.; Xu, H.J. Facile Synthesis of Au Nanoparticle-Coated Fe3O4 Magnetic Composite Nanospheres and Their Application in SERS Detection of Malachite Green. *Spectrochim Acta A Mol Biomol Spectrosc* **2020**, *241*, doi:10.1016/j.saa.2020.118532.

44. Lang, X.Y.; Guan, P.F.; Zhang, L.; Fujita, T.; Chen, M.W. Characteristic Length and Temperature Dependence of Surface Enhanced Raman Scattering of Nanoporous Gold. *The Journal of Physical Chemistry C* **2009**, *113*, 10956–10961.

45. Zhang, L.; Song, Y.; Fujita, T.; Zhang, Y.; Chen, M.; Wang, T. Large Enhancement of Quantum Dot Fluorescence by Highly Scalable Nanoporous Gold. *Advanced Materials* **2014**, *26*, 1289–1294.

46. Ahmed, S.R.; Hossain, M.A.; Park, J.Y.; Kim, S.-H.; Lee, D.; Suzuki, T.; Lee, J.; Park, E.Y. Metal Enhanced Fluorescence on Nanoporous Gold Leaf-Based Assay Platform for Virus Detection. *Biosens Bioelectron* **2014**, *58*, 33–39.

CHAPTER V

Optimizing Chemical De-alloying Conditions for Nanoporous Copper Fabrication from Brass

5.1 Introduction

In the context of de-alloying as discussed in Chapters I and II, np-Cu (nanoporous copper) is one of the most thoroughly studied nanoporous metals, following nanoporous gold (np-Au) due to its unique properties and diverse applications [1]. Copper is cheaper than gold and silver, demonstrating higher electrical conductivity, significant strength, and oxidation resistance [2]. Np-Cu has various industrial applications; for example, it is used in fuel generation and chemical processes such as water gas shift reaction, alcohol dehydrogenation, and methanol synthesis due to its superior corrosion resistance properties [3]. During de-alloying, the earliest example of nanoporous copper (np-Cu) is known as Raney Cu. This material is produced by de-alloying an alloy with a composition of Al-Cu in a NaOH solution. It serves as an important catalyst in both gas and liquid-phase hydrogenation and dehydrogenation reactions. Subsequently, np-Cu was synthesized using single-phase solid solution precursor alloys, specifically Mn-Cu and Ni-Cu [4]. Additionally, in 2006, Hayes and his colleagues were pioneers in the successful fabrication of monolithic np-Cu by the dealloying of the precursor alloy composed of $Mn_{0.7}Cu_{0.3}$ [5].

Recently, np-Cu was synthesized by the de-alloying of intermetallic or multiphase alloy precursors, such as Zn-Cu, Mg-Cu, and Al-Cu alloys [6,7]. Additionally, several factors affect the de-alloying process, such as the composition of the master alloy, the type of de-alloying solution used, the processing temperature, and the duration of de-alloying. Moreover, the de-alloying solution influences the de-alloying behavior and dissolution process at various stages. However, most of the work done in the past has two significant issues. One of the drawbacks is that the starting materials are very expensive, although the final products look relatively cost-effective. The second issue is that the preparation process is both time-consuming and complicated.

To address these issues, this chapter introduced a simple fabrication method for successfully synthesizing nanoporous copper (hereafter referred to as np-Cu) using a chemical dealloying process. The starting material is the commercial brass bar, composed of $Cu_{60}Zn_{38}$ and trace amounts of other elements like Al, Mn, Si, Fe, Ni, Pd, and Sn. Following that, the bar was cut into small slices for Zn dissolution, which ultimately resulted in a bi-continuous np-Cu in a hydrochloric acid solution. Our investigation aims to identify the most effective parameters for chemical de-alloying of brass bars to obtain 3-dimensional interconnected ligaments and porous structure of np-Cu. Through experimentation, hydrogen chloride (HCl) serves as the chemical agent, and the effect of different concentrations of HCl was investigated. In addition to this, the impact of other parameters, including dealloying time ranging from 1-10 days and de-alloying temperature (25°C and 70°C) on the structural morphology was also evaluated.

5.2 Methodology

5.2.1 Sample Preparation:

A commercial brass bar with a nominal composition of approximately 57-60 atomic percent (at %) Cu and 36-38 at % Zn, along with trace amounts of Al, Si, Mn, Fe, Ni, Sn, and Pd was used as a parent alloy. Several small pieces, each with approximately 1 mm in thickness, were cut from the brass bar. These pieces were mechanically polished with a Struers machine (model LaboPol-5) and silicon carbide papers ranging from 600 to 1200 mesh to achieve a mirror-polished finish. After polishing, samples underwent sonication for 3 minutes in MilliQ water and ethanol solutions to remove the impurities. Then, they were air-dried.

5.2.2 Electrolyte Preparation:

To prepare the electrolyte solution for chemical dealloying, 36% hydrochloric acid (HCl) was diluted with highly purified water to create solutions with 0.1 M, 0.5 M, 1 M, and 5 M concentrations of HCl. Furthermore, an experiment was also performed using 36% purified HCl.

5.2.3 Chemical Dealloying Process

The small brass bars were subjected to chemical dealloying in 15 mL vials at 25°C and 70°C, following different dealloying times: 1, 2, 5, 14, and 15 days. After the completion of dealloying, the samples were extracted from the solution. The samples were washed with highly purified water and subjected to sonication for 3 minutes each in water and ethanol. The dealloying process resulted in a gradual change in the surface color of the Cu-Zn alloy from golden-yellow to reddish brown. The macroscopic analysis indicated removing the Zn phase from the Cu-Zn alloy while the insoluble Cu phase remained intact.

5.2.4 Microstructural analysis

The microstructural transformations in the samples at various processing stages were analyzed SEM-EDS with the same model as described in the earlier chapter to determine the composition of the np-Cu samples. The crystallographic structures of both the brass bar and the dealloyed

samples were investigated using an XRD. The diffraction peaks were identified and indexed with X'Pert Highscore software.

5.3 Result and Discussions

To fabricate np-Cu from a commercial brass piece, several trials were conducted at varying concentrations of HCl, along with different temperatures and dealloying times. The experiments were organized into four distinct batches based on concentration, with each batch corresponding to specific dealloying durations, as outlined in Table 5.1. The weights of the brass pieces were noted both before and after dealloying, allowing for the calculation of the weight loss percentage using the following formula:

$$Wt.loss\ (\%) = \frac{(intial\ wt.) - (final\ wt.)}{initial\ wt.} \times 100$$

The analysis of weight loss revealed significant differences in dealloying rates based on HCl concentration; it can be observed that the dealloying process in the case of 0.1, 0.5, and 1 M HCl is very slow, even after 15 days at 25 °C temperature, the dealloying was not completed. In contrast, using a concentrated solution of HCl (36%) for 14 days at 25 °C temperature resulted in partial dealloying with a notable weight loss of 50%.

Table 5.1: *Weight Loss Analysis of Brass Samples During Chemical Dealloying Using Various Concentrations of HCl*

1st batch of experiments using 0.1 M HCl							
Sr #.	**Electrolyte (M) HCl**	**Volume (ml)**	**Temperature (°C)**	**Time (day)**	**Wt. before dealloying (g)**	**Wt. After dealloying (g)**	**wt. loss (%)**
1	0.1	15	25	1	0.0732	0.0732	0
2	0.1	15	25	2	0.0956	0.0955	0.1
3	0.1	15	25	5	0.0909	0.0906	0.3
2nd batch of experiments using 0.5 M HCl							
Sr #.	**Electrolyte (M) HCl**	**Volume (ml)**	**Temperature (°C)**	**Time (day)**	**Wt. before dealloying (g)**	**Wt. After dealloying (g)**	**wt. loss (%)**
1	0.5	15	25	1	0.1325	0.1316	0.7

2	0.5	1	25	5	0.2091	0.2065	1.2
3	0.5	15	25	15	0.1022	0.1002	1.9
3rd batch of experiments using 1 M HCl							
Sr #.	**Electrolyte (M) HCl**	**Volume (ml)**	**Temperature (°C)**	**Time (day)**	**Wt. before dealloying (g)**	**Wt. After dealloying (g)**	**wt. loss (%)**
1	1	15	25	1	0.0962	0.0953	1
2	1	15	25	5	0.1408	0.1387	1.5
3	1	15	25	15	0.2126	0.2075	2.4
4rth batch of experiments using 36% HCl							
Sr #.	**Electrolyte (M) HCl**	**Volume (ml)**	**Temperature (°C)**	**Time (day)**	**Wt. before dealloying (g)**	**Wt. After dealloying (g)**	**wt. loss (%)**
1	11.6	10	25	14	0.2438	0.1218	50

5.3.1 SEM analysis

Scanning electron microscopy analysis was performed to understand the influence of different concentrations of HCl, dealloying times, and temperature on the structural morphology of np-Cu. The study revealed that HCl concentration significantly influences the zinc dissolution rate and the formation of interconnected porous structures. The samples treated with 0.1 M HCl are shown in Fig 5.1. The results showed minimal surface changes after 1 day, with slight etching observed but no distinct shapes forming, Fig 5.1 (a). After 5 days, the surface exhibited only minor etching with small pits, indicating a slow dissolution of zinc that resulted in limited formation of porous structures, as shown in Fig 5.1 (b).

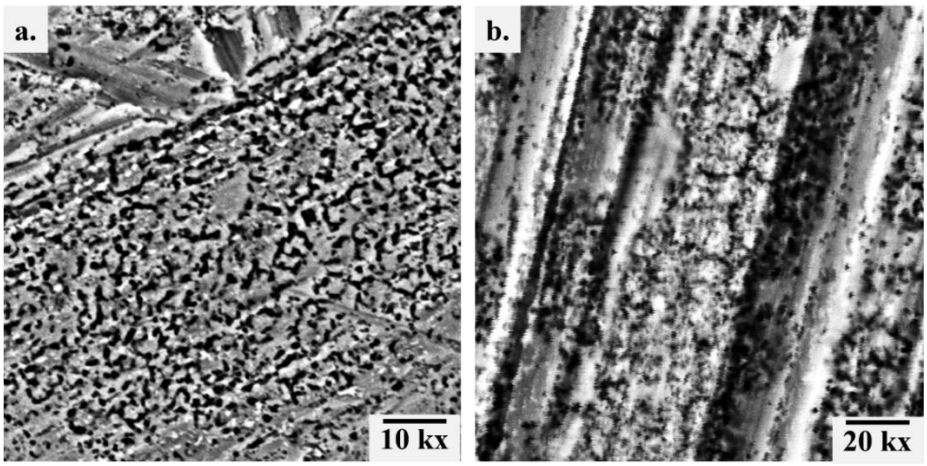

Figure 5.1*: Chemical dealloying of np-Cu using 0.1 M HCl at 25 °C (a) dealloying after 1 day (b) dealloying after 5 days.*

In contrast to 0.1 M HCl, the SEM analysis of 0.5 M HCl np-Cu treated sample was illustrated in Fig 5.2 by varying the time of dealloying at 25°C. Fig 5.2 (a) revealed the beginning of porosity with small, densely packed grains. The surface starts to develop pores but is still relatively compact after 1 day of the dealloying treatment. As the dealloying time increased from 1 day to 5 days, the pores became more pronounced. The structure reveals more intricate details with layers forming, indicating the initial formation of ligaments as represented in Fig 5.2 (b). The more complex and compact structure of np-Cu was observed in Fig 5.2 (c) after 15 days of dealloying with a few pores. They indicated slightly higher but still slower dissolution of zinc. However, the increased concentration might accelerate the dissolution of zinc, but it is still not enough for the formation of well-defined pores.

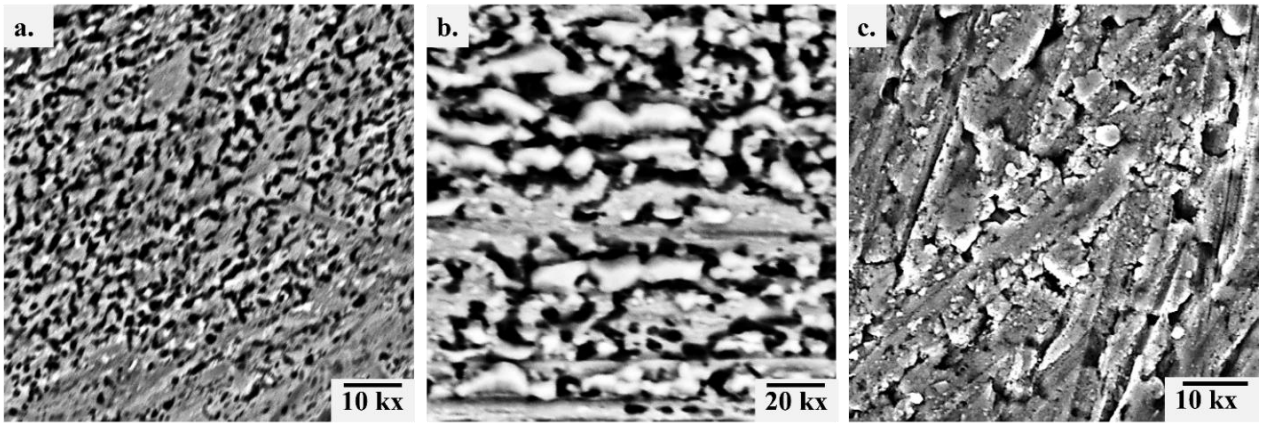

Figure 5.2: *Chemical dealloying of np-Cu using 0.5 M HCl at 25 °C (a) dealloying after 1 day (b) dealloying after 5 days (c) after 15 days.*

At 1 M HCl, np-Cu dealloying was conducted for 1 day, 5 days, and 15 days, as shown in Fig 5.3. A noticeable etching and porosity were observed compared to 0.1 and 0.5 M HCl after 1 day, as indicated in Fig 5.3 (a). After 5 days, a compact porous structure developed, resulting in zinc dissolution Fig 5.3 (b). However, after 15 days, the morphology shifted to long, flat,

irregular rod-like structures, as shown in Fig 5.3 (c) with the continuous dissolution of zinc. Despite these morphological changes, the porous structure and interconnecting ligament were not observable. Even the weight loss indicates that only 2% of zinc was dissolved while the remaining zinc is still present. These observations may highlight the need to increase the concentration of HCl to achieve completed dealloyed np-Cu with more pronounced structural features.

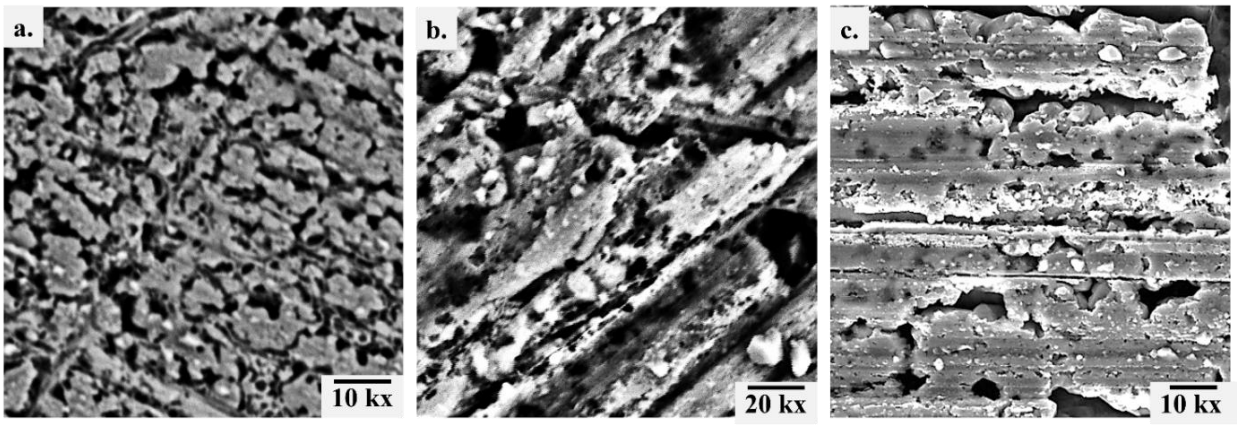

Figure 5.3: *Chemical dealloying of np-Cu using 1 M HCl at 25 °C (a) dealloying after 1 day (b) dealloying after 5 days (c) after 15 days.*

Therefore, one trial was performed using 11.6 M HCl, a more concentrated solution as an electrolyte, and dealloying was performed for approximately 14 days, as represented in Fig 5.4. In the initial stage of chemical dealloying of brass using 11.6 M HCl, as shown in Fig 5.4 (a) at a magnification of 1 kx, the microstructure reveals the formation of porous structure, characterized by an irregular circular with rough surfaces. These observations indicate the preferential removal of zinc from the brass alloy. The rough and irregular nature of these pores suggests that the dealloying process might be progressing unevenly due to variations in the alloy composition.

As the magnification increases to 5 kx in Fig 5.4 (b), more defined features appear within the porous matrix. Elongated rod-like structures are observed along the irregular structure features. The presence of these rod-like structures suggests that the material is undergoing significant morphological changes, which could be attributed to the continued dissolution of zinc and the subsequent reorganization of the remaining copper atoms.

At the highest magnification of 10 kx, as shown in Fig 5.4 (c), cracks are visible in the walls of the rod-like strands. These cracks indicate the formation of zinc oxide (ZnO) due to the ongoing dissolution process. The appearance of these cracks raises concerns about potential over-etching and the loss of structural integrity in the material. Moreover, the formation of ZnO also suggests that the dealloying process has reached a stage where the remaining zinc reacts with oxygen, further altering the material's properties.

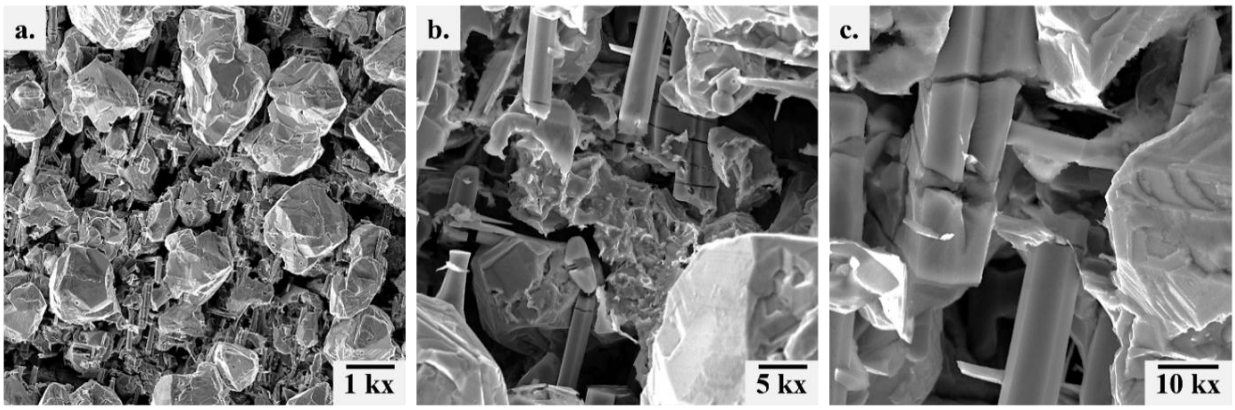

***Figure 5.4**: Chemical dealloying of np-Cu using 11.6 M HCl at 25 °C (a) at lower magnification of 1 kx (b) 5 kx (c) at higher magnification, i.e. 10 kx.*

5.3.2 XRD analysis

The XRD analysis of chemically dealloyed brass bars at room temperature using different concentrations of HCl is illustrated in Fig 5.5. The XRD reflection of the brass bar reveals the three main peaks at 43.3°, 62.9,° and 79.5,° as shown in Fig 5.5 (a), which correlate to the Cu-Zn pattern (PDF: 03-065-6321) commonly named β phase. As the chemical dealloying was initiated using 0.1 M HCl, two new peaks grew with very low intensity at 50.5° and 74.2°, indicating the presence of Cu (PDF: 03-065-9026). As we increased the HCl concentration from 0.1 M to 1 M, an additional peak at 43.4° appeared, as represented in Fig 5.5 (b), and its intensity increased with the increase in HCl concentration. This peak also corresponds to the Cu pattern. Notably, when 11.6 M HCl was used, the intensity of Cu-Zn peaks decreased, leaving behind the highly intense pure Cu peak, as opposed to a lower HCl concentration. Because all of the zinc is dissolved in the solution, these results indicate that dealloying occurs, but not throughout the thickness of the brass bar.

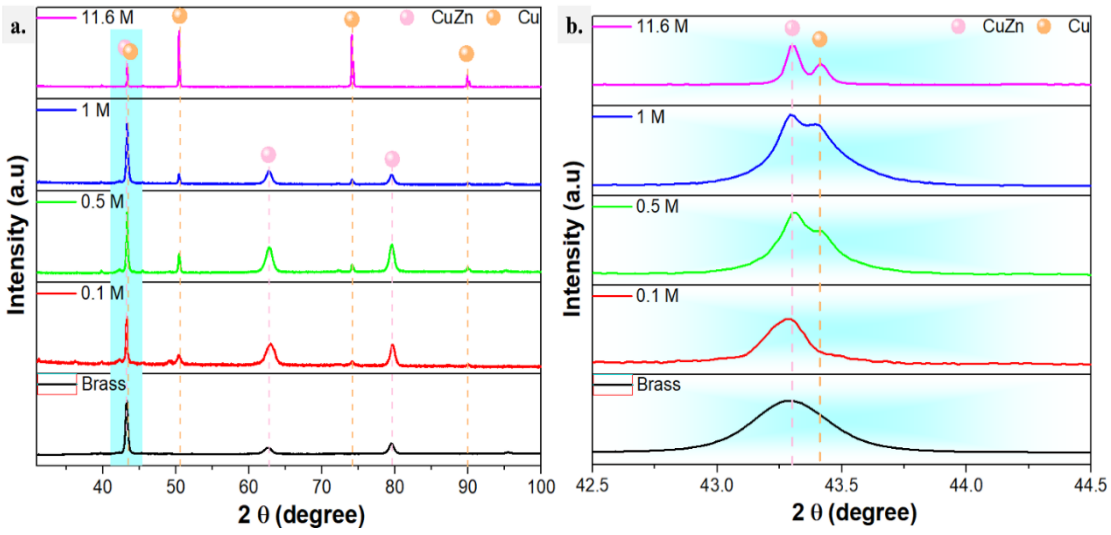

***Figure 5.5**: XRD analysis of chemically de-alloyed brass bars using different concentrations of HCl at room temperature (a) Complete scale (b) Zoom-in view of Cu-Zn peak and Cu peak*

5.3.3 Effect of temperature (70 ºC)

To assess the impact of temperature, a few trials were also conducted at 70 °C using three different concentrations of HCl: 1 M, 5 M, and 11.6 M. The weight of small pieces of brass was measured before and after the treatment, as detailed in Table 5.2.

Table 5.2: *Weight Loss Analysis of Brass Samples During Chemical Dealloying at 70 ℃ Using Different Concentrations of HCl*

Sr #.	Electrolyte (M) HCl	Volume (ml)	Temperature (°C)	Time (day)	Wt. before dealloying (g)	Wt. After dealloying (g)	Wt. loss (%)
1	1 M	15	70	5	0.3313	0.3047	8.03
2	5M	15	70	19hr	0.1540	0.0865	43.8
3	11.65	15	70	1	0.3200	0.0010	99.6

The findings indicate a direct relationship between the concentration of HCl and weight loss observed in the brass samples. At a concentration of 1 M HCl, the weight loss was minimal, with only 8.03% of the total weight lost over 5 days. In contrast, at a concentration of 5 M HCl, the weight loss increased significantly to 43.8% in 19 hours. The most notable weight loss was observed with the highest concentration of 11.6 M HCl, where 99.6% of the sample's weight was lost in just 1 day.

5.3.4 SEM Analysis

To gain a clearer understanding of how temperature affects the structural morphology of the dealloyed sample, scanning electron microscopy analysis was conducted, as shown in Fig. 5.6. The structural features of np-Cu, dealloyed using 1 M HCl for 5 days at 70 °C are shown in Fig. 5.6 (a, b). The np-Cu structure appears relatively intact, with some visible porosity. The surface is rough but does not exhibit significant pitting or large voids. These findings indicate partial dealloying, where only a small amount of material has been removed, resulting in minor structural changes. In another trial, 5 M HCl was used instead of 1 M, with the dealloying time set to 19 hours. The subsequent SEM analysis is presented in Fig. 5.6 (c, d). The np-Cu structure shows increased corrosion, characterized by larger voids and a more irregular surface than the 1 M HCl treatment. This suggests a higher degree of dealloying, where almost all the zinc has been removed, leading to noticeable morphological changes. In the final trial, an 11.6 M HCl solution was used, as depicted in Fig. 5.6 (e, f).

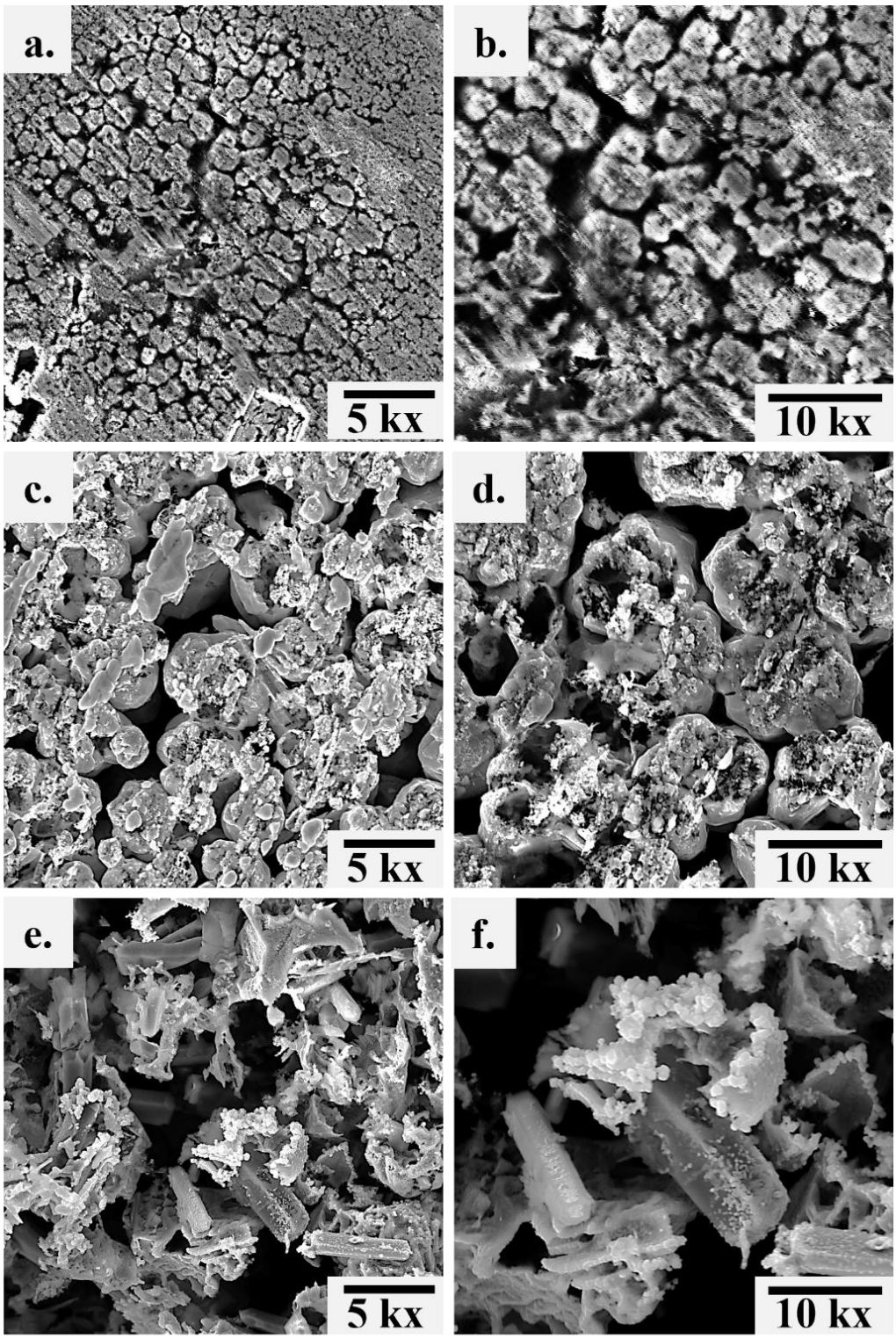

***Figure 5.6**: chemical dealloying of np-Cu at 70 ºC (a, b) 1 M for 5 days HCl (c, d) 5 M HCl for 19 hr and (e, f) 11.6 M HCl for 1 day*

The resulting structure reveals three-dimensional elongated features with drastically altered thin-walled structures, indicating potential over-etching and a loss of structural integrity. A significant amount of material has been removed, with approximately 99.6% of the samples

dissolved, leaving only 0.4% remaining. These observations highlight the critical role of HCl concentration in controlling the dealloying process and the resulting structural features of np-Cu. This information is essential for optimizing the dealloying conditions for specific applications where the structural properties of np-Cu are crucial.

5.3.5 XRD analysis

The effect of temperature on the chemical dealloying process was further evaluated at 70°C using different concentrations of HCl, as shown in Fig 5.7. Fig 5.7 (a) displays the XRD patterns over a range of 2θ angles from approximately 30° to 100°. The peaks corresponding to the Cu-Zn pattern (PDF: 03-065-6321) are marked with pink lines, while those for Cu (PDF: 03-065-9026) are highlighted in orange, and the peak position is the same as discussed in the 5.1.2 section. The results reveal that the intensity of Cu-Zn peaks changes according to the concentration of the dealloying solution, and distinct Cu peaks emerge with varying intensities depending on the HCl concentration. Fig. 5.7 (b) provides a zoomed-in view of the XRD patterns between approximately 42.5° and 44.5°, clearly showing changes in the position and shape of Cu-Zn peaks and highlighting the growth of the Cu peak as HCl concentration increases. Moreover, the XRD analysis of chemically dealloyed brass bars conducted at both room temperature and 70 °C provides valuable insights into the effect of HCl concentration on dealloying. Higher concentrations of HCl facilitate the removal of Zn from the alloy, and elevated temperature further enhances the dealloying process by reducing the treatment time.

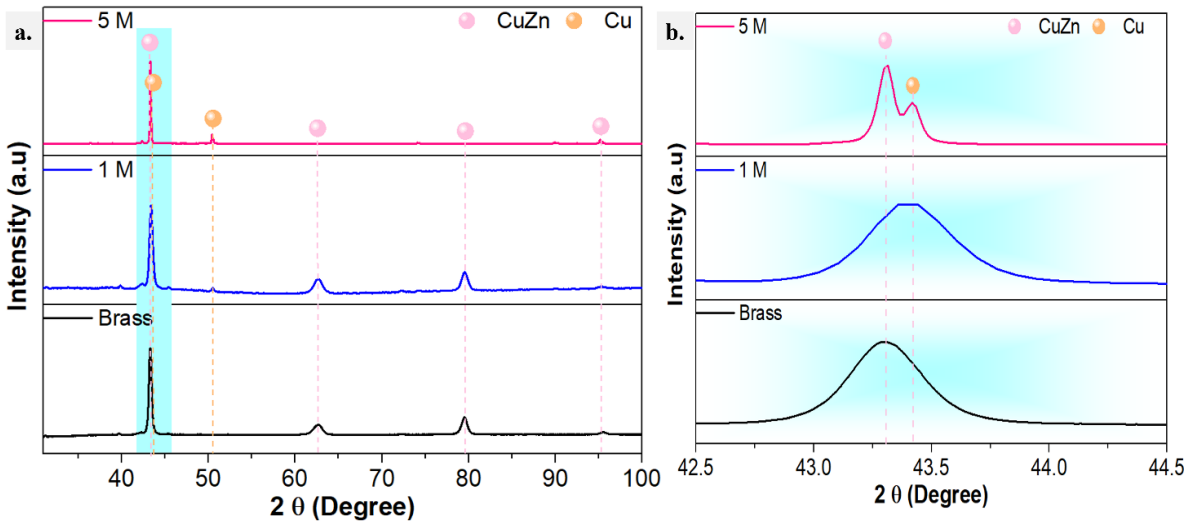

Figure 5.7: *XRD analysis of chemically dealloyed brass bar using different concentrations of HCl at 70 °C (a) Complete scale (b) Zoom-in view of Cu-Zn peak and Cu peak.*

5.3.6 EDS analysis

Furthermore, the effects of chemical dealloying on brass composition with a specific focus on the changes in the concentrations of Cu that was represented with red color and Zn with green were evaluated using an Energy Dispersive Spectroscopy (EDS) analysis, as illustrated in Fig. 5.8. Fig. 5.8 (a) represents the composition of different brass bars that were treated with

different HCl concentrations: 0.1, 0.5, 1, and 11.6 M at room temperature. The results revealed that as the HCl concentration increased, the Zn content decreased while the Cu content increased. Notably, the lower concentrations, such as 0.1, 0.5, and 1 M, were less effective at removing Zn, resulting in minimal dissolution. In contrast, the highest concentration of HCl, i.e. 11.6 M proved to be more effective in dissolving Zn.

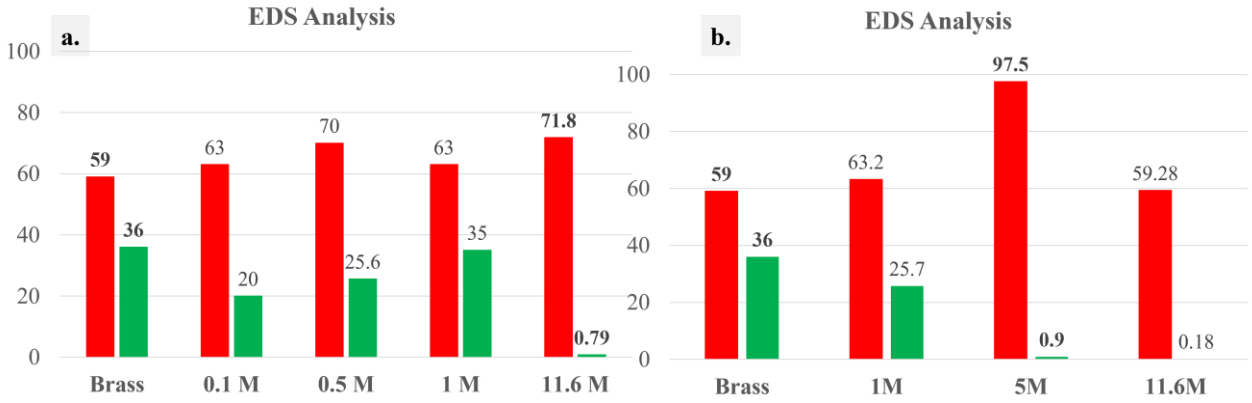

Figure 5.8: *EDS analysis of dealloyed Bar using different concentrations of HCl where red bars represent the at % of Cu and Geen bars represent the at % of Zn (a) At room temperature (b) At 70 °C*

Additionally, the effect of temperatures at 70 °C on the composition of the dealloyed brass bar was also evaluated using the different concentrations of HCl, as shown in Fig. 5.8 (b). It was observed that as the HCl concentration increased from 1 M to 5 M, there was a significant decrease in Zn content alongside an increase in Cu content. This indicated that the higher temperature facilitated the dealloying process, leading to a more pronounced reduction in Zn compared to room temperature conditions. However, when the HCl concentration was increased from 5 to 11.6 M, the entire brass bar dissolved completely in the solution, leaving behind a small remnant. Furthermore, the effectiveness of the dealloying process is positively correlated with HCl concentration; higher concentrations result in a more pronounced reduction in Zn content, indicating that the chemical environment plays an important role in the efficiency of the dealloying process.

5.4 Conclusion

In this chapter, a common brass bar is used as the starting material, offering a cost-effective way to produce np-Cu with potential catalytic applications. The present study examines the optimal conditions for producing np-Cu from brass by using several factors, including HCl concentration, duration, and temperature, via the method of chemical dealloying. Additionally, the mass of the brass bar was evaluated before and after the chemical dealloying, demonstrating that lower HCl concentrations, particularly 0.1 M, 0.5 M, and 1 M, resulted in slower Zn dissolution and insignificant weight loss. In contrast, excessive concentrations of 11.6 M (for example, 36% HCl) may result in severe weight loss and porosity. Furthermore, the SEM studies demonstrated that optimum porosity may be achieved with 5 M HCl at 70 °C and 11.6

M HCl at ambient temperature. It was observed that the dealloying process was significantly accelerated by higher temperatures, which facilitated more rapid Zn dissolution and augmented the development of the linked porous network. EDS results supported these findings by showing the progressive removal of Zn and the relative enrichment of Cu in the final dealloyed material. Overall, these results underscore the critical role of dealloying parameters in developing a three-dimensional interconnected porous structure. Future research could explore alternative dealloying solutions or different alloy combinations further to enhance the properties of np-Cu for various industrial applications. To improve the qualities of np-Cu for a range of industrial applications, further research might investigate other alloy combinations or dealloying techniques. Overall, our findings point to a practical, efficient method for producing np-Cu, making it more accessible for a broader range of technological applications.

Reference

1. Park, B.; Le Han, D.; Saito, M.; Mizuno, J.; Nishikawa, H. Fabrication and Characterization of Nanoporous Copper through Chemical Dealloying of Cold-Rolled and Annealed Mn–Cu Alloy. *Journal of Porous Materials* 2021, *28*, 1823–1836, doi:10.1007/s10934-021-01128-7.

2. Egle, T.; Barroo, C.; Janvelyan, N.; Baumgaertel, A.C.; Akey, A.J.; Biener, M.M.; Friend, C.M.; Bell, D.C.; Biener, J. *LLNL-JRNL-733718 Multiscale Morphology of Nanoporous Copper Made from Intermetallic Phases*; 2017;

3. Xu, Z.; Erinomo, A.M.; Dan, Z.; Qin, F.; Chang, H. Flexible SERS Substrates with Gradient Porous Cu Structure Dealloying from the Thermal Diffusion Couples of Al/Cu Stacking Foils. *Chemical Engineering Journal* 2024, *490*, doi:10.1016/j.cej.2024.151871.

4. Smith, A.J.; Tran, T.; Wainwright, M.S. Kinetics and Mechanism of the Preparation of Raney® Copper. *J Appl Electrochem* 1999, *29*, 1085–1094.

5. Hayes, J.R.; Hodge, A.M.; Biener, J.; Hamza, A. V; Sieradzki, K. Monolithic Nanoporous Copper by Dealloying Mn–Cu. *J Mater Res* 2006, *21*, 2611–2616.

6. Liu, W.; Zhang, S.; Li, N.; Zheng, J.; An, S.; Xing, Y. Monolithic Nanoporous Copper Ribbons from Mg-Cu Alloys with Copper Contents below 33 at.%: Fabrication, Structure Evolution and Coarsening Behavior along the Thickness Direction. *Int J Electrochem Sci* 2011, *6*, 5445–5461.

7. Zhang, Q.; Zhang, Z. On the Electrochemical Dealloying of Al-Based Alloys in a NaCl Aqueous Solution. *Physical Chemistry Chemical Physics* 2010, *12*, 1453–1472.

CHAPTER VI

Nanoporous Copper Films via Dynamic Hydrogen Bubbling: A Promising SERS Substrate for Sensitive Detection of Methylene Blue

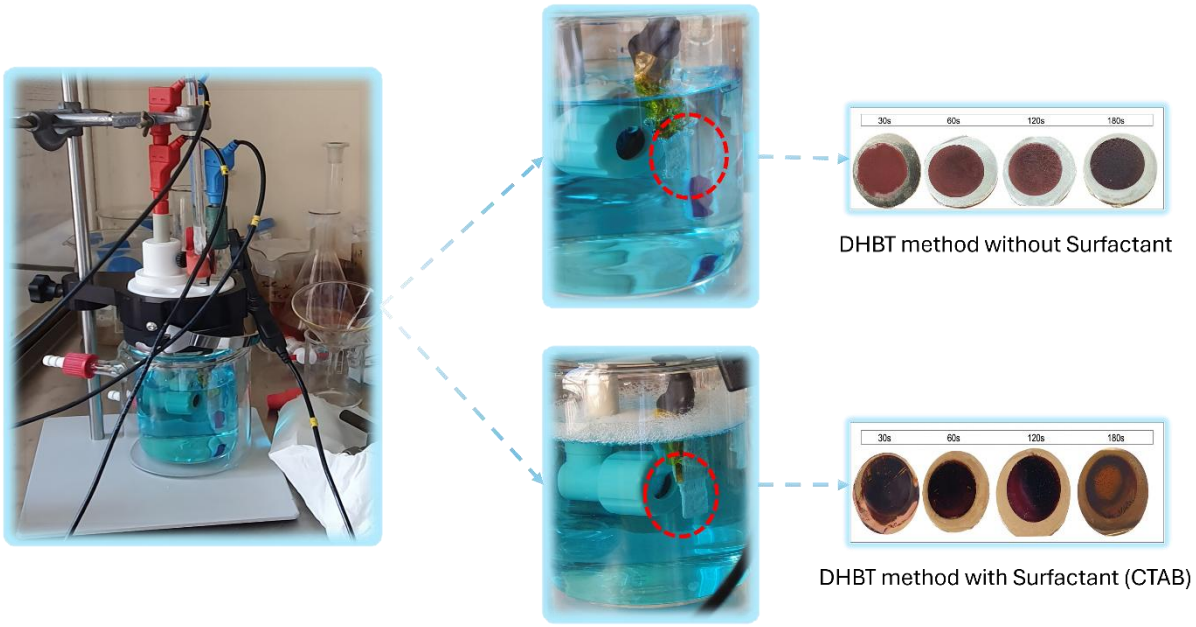

6.1 Introduction

Considerable attention has been focused on improving the development/fabrication of 3-dimensional porous metals due to their unique features such as controlled morphology, high surface area, well-organized pore structure, and precise pore-size distributions [1,2]. These unique characteristics have applications in catalysis [3,4], sensors [5], SERS (surface-enhanced Raman scattering) [5], and pharmaceuticals [6,7]. Among the porous metals, there has been a growing interest in porous copper (Cu) and copper alloys due to their exceptional characteristics like high thermal conductivity and catalytic activity [8]. Moreover, introducing the porosity to copper and its inherent metallic characteristics enhances its catalytic efficiency, fluid permeability, wettability, optical and electrocatalytic applications [9]. Nanoporous copper can be fabricated using different methods, including template synthesis, chemical dealloying, electrodeposition, and surfactant-mediated synthesis [10–14].

Among these, the electrodeposition using the dynamic hydrogen bubble template method (DHBT) is one of the most effective techniques for fabricating nanoporous copper, introduced by Shin et al. in 2003 [15]. It is a cost-effective approach that allows precise control over the structure of the deposited material by adjusting various factors such as temperature, electrolyte composition, current/potential, and duration [16,17]. Therefore, it is essential to have precise control of the electrodeposition parameter to prepare high-performance porous copper. The DHBT method involves the evolution of hydrogen gas, which serves as a soft template for reducing the metal ions and forming a 3D hierarchical porous nanostructure. The process

begins with the nucleation of hydrogen gas on the electrode surface, followed by the evaluation of the hydrogen bubbles and their subsequent desorption from the surface [18].

When an overpotential is applied, the hydrogen gas generated on a surface substrate works as a cathode aggregate and temporarily adheres to the surface before desorbing into the gas phase. This aggregation leads to forming a hollow porous framework with a large surface area, which occurs through the focused deposition around short-lived adherent hydrogen bubbles caused by the simultaneous reduction of metal ions in the precursor solution [19]. Moreover, it was noticed that the surfactants commonly used as stabilizers are favorable in the DHBT synthesis method to customize and stabilize the hydrogen bubbles produced from the electrochemical reduction of protons [20]. This, in turn, impacts the pore structure of the deposited metal films. Li et al. studied the evolution process of porous copper films and revealed that a higher concentration of CTAB results in smaller pore size and wall thickness because the hydrogen bubble size is influenced by the surfactant concentration. [21].

Furthermore, the pore morphology resulting from this technique depends on the stability of the surface-adsorbed hydrogen bubbles. Using DHBT templates for surface nanostructuring allows precise porosity control, pore diameter, and film thickness, resulting in nanoporous copper (NPC) with significant active sites, a notably large surface area, and a high volume of interconnected porosity [22]. The source and concentration of the substrate material and the presence of surfactants and additives can also influence the structural morphology. Adjusting these parameters allows the bubble size to be controlled before it is released from the substrate. Nanoporous copper fabricated using the DHBT method has potential for use in surface enhanced Raman spectroscopy (SERS) due to its large surface area and interconnected porosity [23].

Recent research suggests that nanostructured copper substrates can provide comparable enhancement levels to traditional Ag and Au substrates, increasing interest in developing optimized nanostructured copper for efficient SERS applications at a competitive cost [24]. With its unique advantages and cost-effectiveness, NPC is anticipated to serve as a promising substrate for SERS. Chen et al. successfully synthesized nanoporous copper with adjustable pore sizes by controlling the dealloying process, leading to enhanced SERS performance due to the tunable nanoporosity among the copper nanoparticles [25]. In a separate study, Tan et al. investigated the SERS properties of copper butterfly wing scales. Their results indicated that the significant Raman enhancement primarily arises from the three-dimensional sub-micrometer periodic rib structures found on the main ridges of the Cu scales. These structures demonstrated a low detection limit of 10^{-8} M for R6G [26]. Herein, the SERS activity of the Cu substrate can be modulated by using the electrodeposition with the DHBT method to control the morphology of the NPC film. This study aims to enhance the effectiveness of the SERS substrate and make it highly sensitive for detecting methylene blue (MB). This highly toxic MB dye is frequently misused illegally in aquaculture as an alternative antifungal, by neglecting its adverse effects on human health like nausea, anxiety, and quadriplegia.

6.2 Material and Methods

6.2.1 Material

The electrodeposition of the NPC was conducted on a metallic substrate, which was prepared by cutting a commercial brass bar with a 15 mm diameter into disks approximately 1 mm thickness. The nominal composition of the brass is approximately 53-56 at % copper and 44 – 47 at % zinc, resulting in a $\alpha+\beta$ structure. The brass discs were mechanically polished using a Struers machine (model LaboPol-5) and silicon carbide papers (600 to 1200 mesh) to achieve a mirror-polished surface. After polishing, samples were sonicated for 3 minutes in acetone, MilliQ water, and then finally in ethanol solutions to remove the impurities and dry in the air.

The electrolyte for electrodeposition was prepared by dissolving 0.5 M sulphuric acid (H_2SO_4) and 0.1 M copper sulphate ($CuSO_4$) in 200 mL of MilliQ water. In another experiment, an alternative electrolyte solution was prepared using CTAB with a concentration of 0.5 mM, along with the same concentrations of sulfuric acid (0.5 M) and copper sulphate (0.1 M) in 200 mL of MilliQ water.

Methylene blue (MB) was selected as the probe molecule to assess the SERS activity of the NPC samples. To prepare the solutions, MB powder was precisely weighed and dissolved in 20 mL of deionized water to create a 10^{-3} M stock solution. This stock solution was then serially diluted to obtain concentrations ranging from 10^{-4} M to 10^{-7} M. All reagents used were chemical grade and sourced from Sigma Aldrich.

6.2.2 Fabrication of NPC

The electrochemical measurements were performed using a standard three-electrode setup connected to an Autolab potentiostat from Metrohm, Utrecht, The Netherlands. The porous Cu was electrodeposited on a well-polished brass disc (acting as a working electrode) using the 0.5 M H_2SO_4 and 0.1 M $CuSO_4$ as electrolyte; the instrument was used in the potentiostatic mode by applying a constant voltage of -4 V. The Platinum foil of 0.15 mm was served as a counter electron and placed at 2 cm of distance in front of the working electrode, while an Ag/AgCl reference electrode, configured in a double-bridge system with a saturated KCl solution, completed the circuit. All the samples were electrodeposited at 25 °C by varying the time from 30 s, 60 s, 120 s, and 180 s under unstirred conditions. After electrodeposition, the samples were thoroughly rinsed with distilled water and stored in well-closed sample holders for further analysis. A Bruker Alicona InfiniteFocus G6 was used to measure the thickness of NPC film with and without CTAB. The topographies were performed by using a 4x objective with a working distance of 30 mm.

6.2.3 SERS Measurements

NPC disks, fabricated with and without CTAB using the DHBT method for deposition times of 30 s, 60 s, 120 s, and 180 s, were then immersed in 5 mL solution of the 10^{-4} M MB overnight. After immersion, the samples were taken out of the solution and left to air-dry for 10 minutes

to ensure optimal absorption of probe molecules onto the surface. Once dried, the samples were positioned in the sample holder of the SERS instrument for measurement. This procedure was repeated consistently for each MB concentration: 10^{-4} M, 10^{-5} M, 10^{-6} M, and 10^{-7} M. The SERS EF for the NPC film fabricated both with and without CTAB, was determined using the following formula as described in Chapter III.

$$E.F = \frac{I_{SERS}}{C_{SERS}} \times \frac{C_{blank}}{I_{blank}}$$

The concentration of the MB used for the SERS measurements, C_{SERS}, was set at 10^{-7} M. In contrast, the concentration for the control measurements on the copper disk substrate, C_{blank}, was set at 10^{-4} M.

6.3 Results and Discussions

The SEM images of NPC deposited films in Fig. 6.1 provide a detailed depiction of the morphology of as-prepared NPC via the DHBT method in the absence and presence of CTAB additive, prepared by applying -4 V potential for deposition time of 30 s, 60 s, 120 s, and 180 s respectively. Notably, all the deposited NPCs without CTAB exhibit a relatively homogeneous and uniform distribution of three-dimensional interconnected porous structures characterized by numerous holes and pore walls, possessing a honeycomb-like morphology. The pore size of NPC deposits is directly influenced by the duration of electrodeposition time, as observed in (Fig 6.1 (a, b)) NPC-deposited films in the 30 s have smaller pores compared to those NPC deposited in the 60 s, which have relatively larger pores size (Fig 6.1 (c, d)). Additionally, as the deposition time increased from 60 s to 180 s, the diameter of the honeycomb-like pores also increased, as clearly illustrated in Fig 6.1 (a, c, e, and g). This phenomenon is attributed to the formation of hydrogen bubbles during the electrochemical reduction of hydrogen ions. These bubbles act as dynamic templates during the copper electrodeposition process, facilitating the growth of porous copper films as the hydrogen bubbles coalesce and expand. The coalescence of the hydrogen bubbles determines the growth of the pore diameter.

Furthermore, when the magnification increased from 500 x to 2500 x, a honeycomb-like structure resembled a blossom flower of small and large dendrites growing in all directions (see Fig. 6.1 b, d). As the deposition time increased, the dendrites became more refined and longer than the 30 s and 60 s deposition times. These dendrites had a very long and thin structure with branches of small dendrites, giving a leaf-like appearance throughout. The dendrite formation in NPC film typically begins in the plateau region and is observable in the DHBT method without CTAB (b, d, f, h). When voltage is applied, Cu^{2+} ions are reduced at the cathode, leading to the production of metallic copper and the subsequent formation of either growth nuclei or a uniform copper layer. The initial growth areas then transform into preferential growth zones as the intensified electric fields at the tips of the dendrites attract more Cu^{2+} ions and enhance diffusion flow, thereby facilitating further elongation of the dendrites [27]. Moreover, the anisotropic characteristics of copper growth promote the directed growth of dendrites by allowing atoms to preferentially attach to the corners and edges of existing

crystals. The remarkable 3-D network and hierarchical pore structure of the copper deposits demonstrate the effectiveness of the DHBT method in creating highly porous and interconnected copper structures with tunable pore sizes.

In the DHBT method, surfactants are essential for reducing surface tension and stabilizing the bubble system. They achieve this by preventing bubbles' coalescence and uncontrolled growth during the electrodeposition process. The resulting bubble template leads to a reduction in pore size and wall thickness, which ultimately affects the structural morphology of the deposited NPC. Nonetheless, the direct influence of surface tension on bubble size is relatively low. The SEM analysis of NPC deposited with 0.5 mM of CTAB by varying the deposition times of 30 s, 60 s, 120 s, and 180 s, is illustrated in Fig. 6.1 (a′ - h′).

Notably, the deposited NPCs with CTAB resulted in a markedly different morphology than those prepared without CTAB (Fig. 6.1 (a – h)). The NPCs synthesized with CTAB exhibit a comparatively non-uniform distribution of three-dimensional interconnected porous structures characterized by numerous holes, as illustrated in Fig. 6.1 (a′, c′, e′, and g′). Furthermore, the pore size of the NPCs prepared with CTAB is relatively smaller than those without CTAB even at the higher deposition time, i.e. 180 s a few pores were observed. This might be due to the cationic surfactant (CTAB) that prevents bubble coalescence during the deposition process by adsorbing at the interface between the gas and liquid phases, effectively adhering to the surface of the bubbles. This mechanism maintains smaller hydrogen bubbles, which in turn lead to the formation of smaller pore sizes [22].

However, the porous copper films produced at varying deposition times, both with and without the addition of CTAB, display distinct morphologies, as illustrated in Fig. 6.1. Initially, the NPC displays a more uniform and compact surface morphology at 30 s deposition times (Fig. 6.1 a & a'). As the deposition time extends from 30 s to 120 s, a well-defined honeycomb-like pattern develops, with the upper layer of the honeycomb structure gradually thickening, as depicted in Fig. 6.1 (c & c'). Simultaneously, at 180 s, thin dendritic structures grow and develop into a larger porous network, creating a more intricate and open architecture (Fig 6.1 e and e'). For instance, the deposition time is directly proportional to the pore size; with an increase in deposition time from 30 s to 120 s, the pore size also increases from 12.80 µm to 24.42 µm. The detailed summary of NPC pore size and dendrite size with and without CTAB was presented in Table 6.1. This indicates that longer deposition times result in larger pore sizes (see Fig 6.1 a′, c′, and e′).

***Table 6.1**: Summary of NPC Pore Size with and without CTAB*

Time of Deposition (s)	Pore Size without CTAB (µm)	Pore Size with CTAB (µm)	Dendrite Length (µm) without CTAB
30	26.79 ± 9.4	12.80 ± 4.8	2.86 ± 0.5
60	31.53 ± 12.7	23.46 ± 3.1	4.25 ± 0.4

120	54.84 ± 17.2	24.42 ± 4.8	18.37 ± 5.4
180	73.33 ± 32.2	negligible pores	28.22 ± 5.9

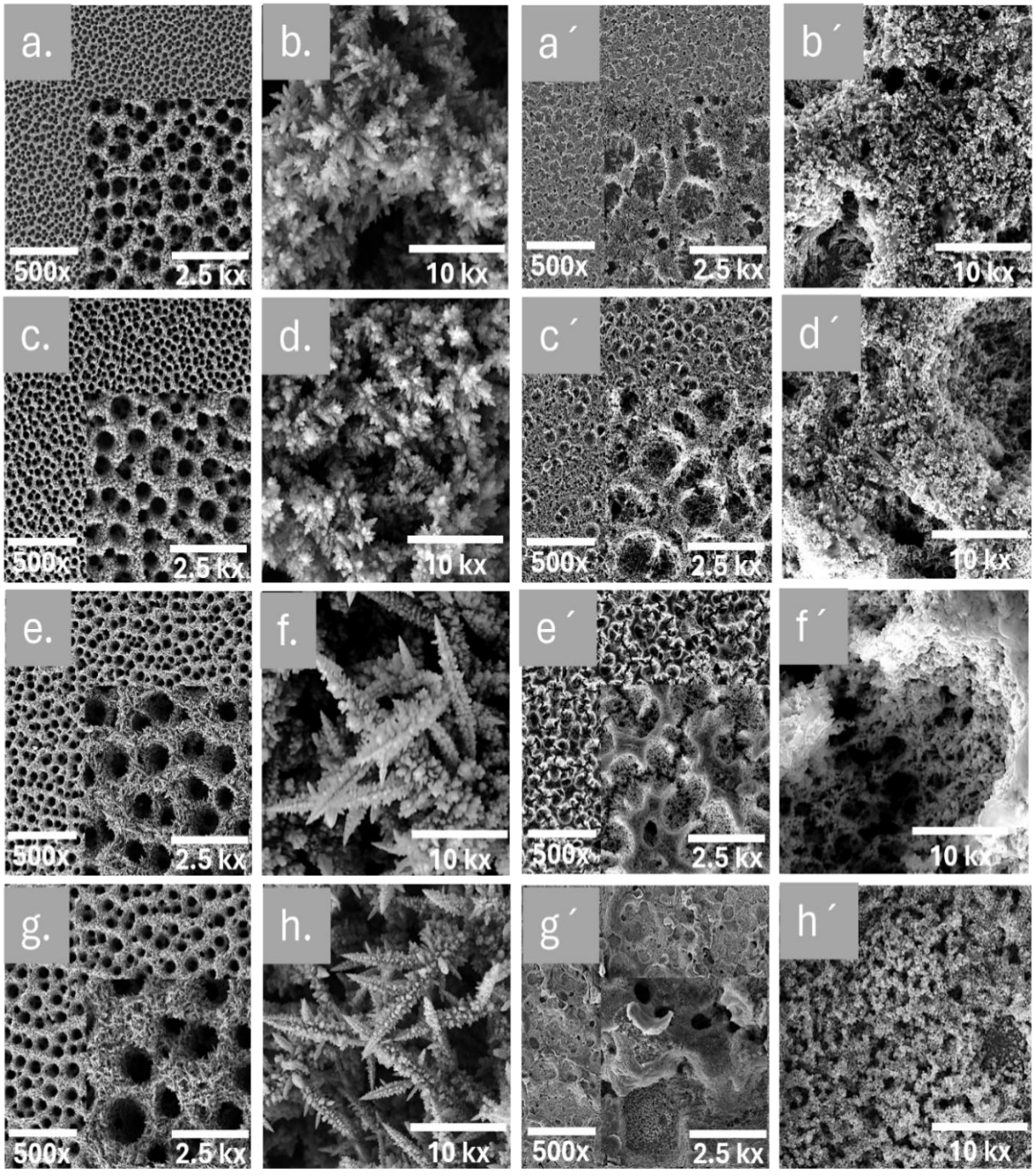

Figure 6.1*: SEM analysis of NPCs deposited with and without CTAB (a, b) represent the NPCs deposit at 30 s without CTAB, (c, d) NPCs deposit at 60 s without CTAB, (e, f) NPCs deposit at 120 s without CTAB, (g, h) NPCs deposit at 180 s without CTAB, similar to this (a′, b′) NPCs deposit at 30 s with CTAB, (c′, d′) NPCs deposit at 60 s with CTAB, (e′, f′) NPCs deposit at 120 s with CTAB, (g′, h′) NPCs deposit at 180 s with CTAB.*

In addition to the impact of the surfactant (CTAB), deposition time significantly influences the morphology of NPC deposits. As shown in Fig. 6.1 (a - h), NPCs formed at different deposition times exhibit distinctly varied structures. With increased deposition time, a honeycomb-like structure gradually develops, accompanied by thinning of the upper layer. At the same time, thinner dendritic structures evolve into larger pore formations. The interfacial growth and thickness of nanoporous copper (NPC) films were investigated with and without the addition of CTAB, as illustrated in Fig. 6.2. In Fig. 6.2 (a), depicts the growth of NPC films in the absence of CTAB, which shows a linear trend in thickness up to 120 s of deposition. However, beyond this point, specifically at 180 s further deposition was inhibited, resulting in a constant or a slight decrease in the thickness of the deposited film. Conversely, Fig. 6.2 (b) shows that the interfacial growth process of copper deposits increases with an increase in the deposition times in the presence of CTAB, demonstrating a direct relationship where the thickness of the porous copper films rises alongside the deposition duration. Furthermore, the high standard deviation values indicate the inhomogeneity of the samples, which is more pronounced for the samples without CTAB reported in Fig 6.2 [32]. Please notice that the sample Fig 6.1 (c) does not follow the linear trend, due to its shape very similar to the sample Fig 6.1 (d). [28].

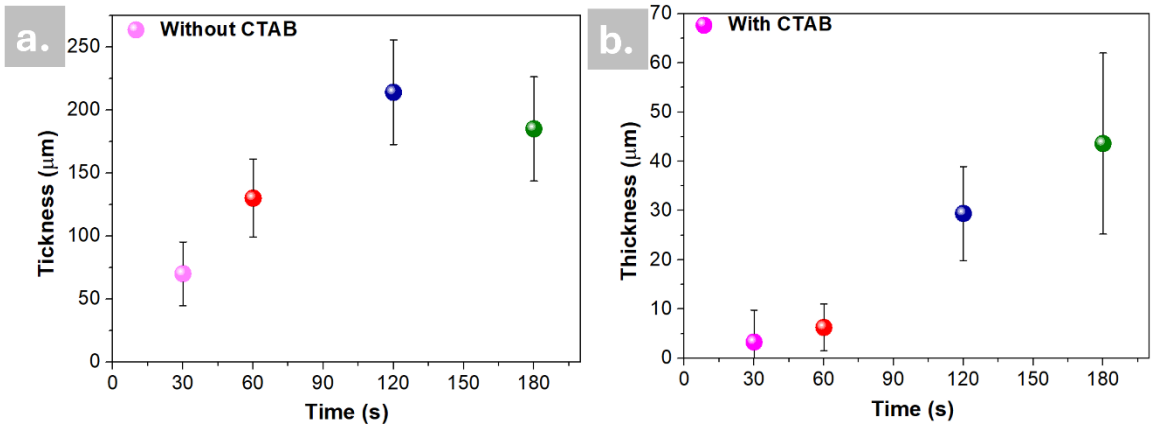

Figure 6.2: *Thickness of NPC with respect of deposition time (a) NPC deposit without CTAB (b) NPC deposited with CTAB.*

As reported in Fig. 6.3, the entire samples were measured by stitching 4x4 images, defining a volume of about 14 mm x 14 mm x 0.5 mm in X, Y and Z directions, for a total of about 21 million points measured. The images were processed by using the metrological software Mountains Map v 10.0. The instrument used was a Bruker Alicona InfiniteFocus G6 using the Focus Variation measurement mode. This technology permits to reconstruct in a fast way the 3D surface of a multimaterial sample without contact and with high resolution.

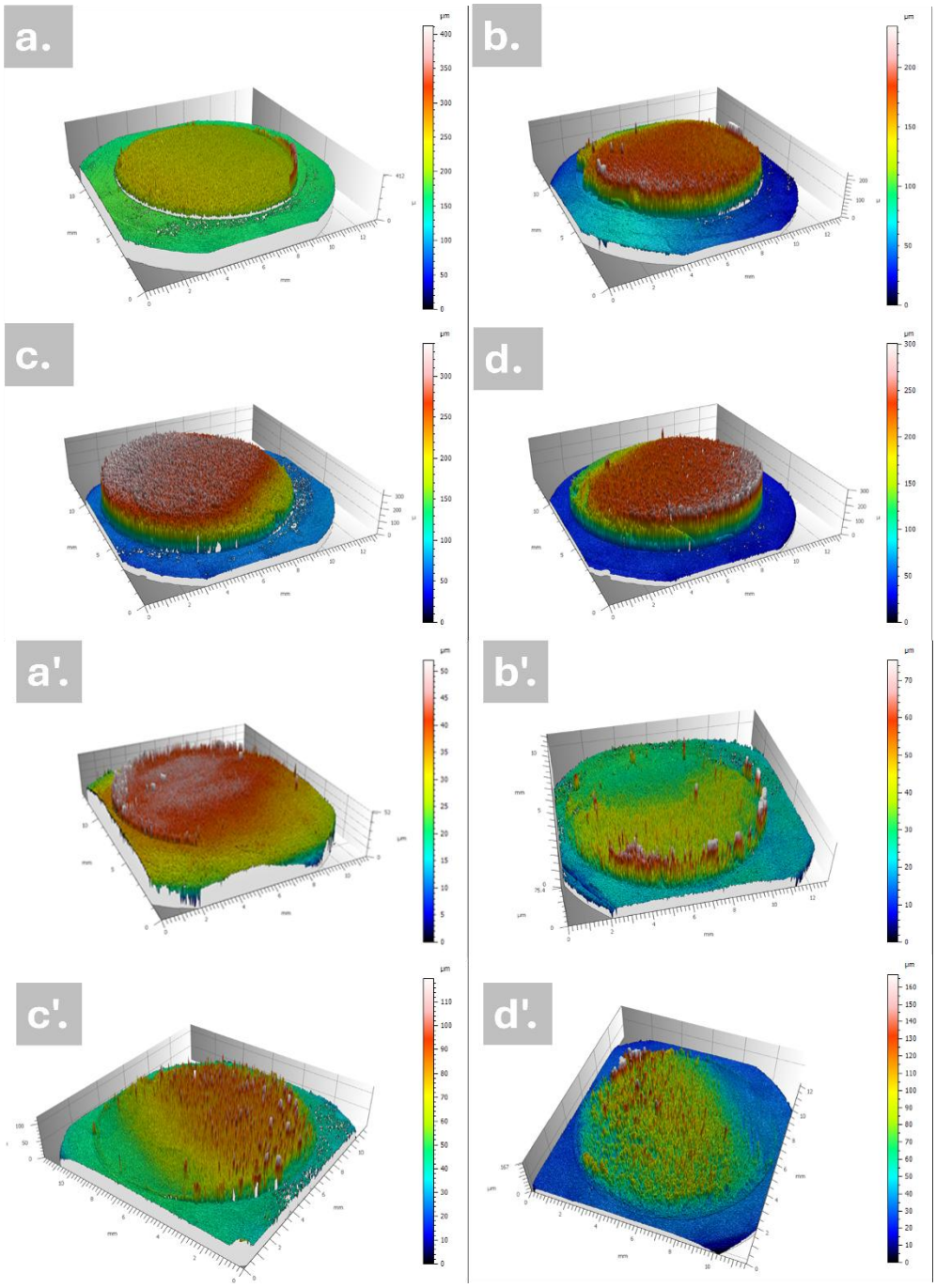

***Figure 6.3**: Mountain Map of thickness measurement with and without CTAB (a) represent the NPCs deposit at 30 s without CTAB, (b) NPCs deposit at 60 s without CTAB, (c) NPCs deposit at 120 s without CTAB, (d) NPCs deposit at 180 s without CTAB, similar to this (a′) NPCs deposit at 30 s with CTAB, (b′) NPCs deposit at 60 s with CTAB, (c′) NPCs deposit at 120 s with CTAB, (d′) NPCs deposit at 180 s with CTAB.*

X-ray diffraction (XRD) analysis of NPC films deposited with and without the surfactant (CTAB) demonstrated notable differences in crystal structure and oxidation resistance, as shown in Fig. 6.4. In Fig 6.4 (a), a significant reduction is observed in the intensity of the characteristic peaks (fcc) associated with the substrate containing α phase of brass [PDF: 00-050-1333] peak (111) at 42.4°, (200) at 49°, and (220) at 72.1° was observed due to the

increasing thickness of the copper deposit. At the same time, the β phase of the brass substrate [PDF: 03-065-6321], identified as body-centred cubic (bcc), was observed at peaks of 31.2°, 53°, and 92° in all samples deposited with CTAB, whereas these peaks did not appear in a sample deposited without CTAB. This phenomenon is attributable to the thickness of the deposited layer, indicating that NPCs deposited with CTAB produced a thinner layer due to CTAB's ability to lower surface tension at the bubble-liquid interface, preventing bubble coalescence and promoting thinner deposition of NPC film. In contrast, the peaks corresponding to the pure Cu crystal structure (fcc) [PDF: 01-089-2839] showed preferential growth along the orientations of pure Cu. All the NPCs deposited with and without CTAB display uniform crystal planes by exhibiting significant variations in peak intensities, as shown in Fig. 6.4 (a, b).

Furthermore, in the absence of CTAB, a relatively weak diffraction peak corresponding to Cu_2O [PDF: 01-078-2076] is observed in all NPCs, though with varying intensities. This peak is attributed to the oxidation of the porous copper surface when exposed to air. Notably, the intensity of Cu_2O diffraction peaks in NPCs synthesized with the CTAB additive is significantly lower or even negligible compared to those prepared without CTAB. This suggests that CTAB molecules effectively inhibit the crystal growth of Cu_2O, thereby enhancing the oxidation resistance of NPCs. The Shin et al. [29] study further supports these observations that, the low presence of copper oxide in the XRD characterization with CTAB samples allows for the formation of Cu^{2+} from CuO or Cu_2O and the reduction of Cu^{2+} ions on the surface of the working electrode due to the abundance of protons in the electrolyte. This suggests that adding CTAB may improve the oxidation resistance of NPCs [30].

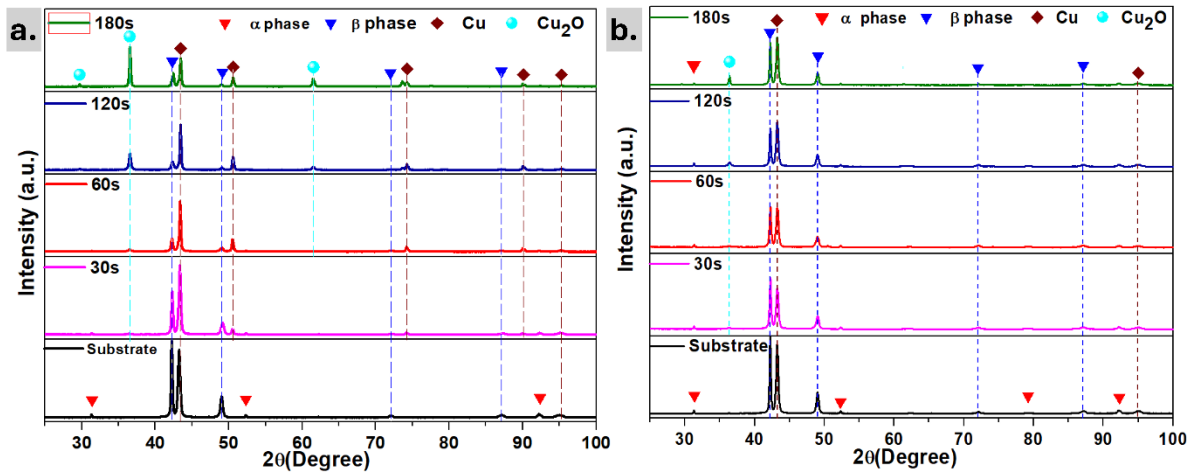

***Figure 6.4**: XRD analysis of NPCs deposited via DHBT (a) NPCs without CTAB (b) NPCs with CTAB.*

6.3.1 SERS analysis

The SERS activity of the NPC substrates was assessed by immersing them in a 10^{-4} M MB solution used as the probe molecule. The SERS spectra were obtained by focusing laser light directly onto the pore walls of the three-dimensional porous copper films. All the samples were initially tested with the same concentration of MB to identify the most active substrate, with

and without the addition of CTAB, as illustrated in Fig. 6.5. The NPCs deposited for 180 s without CTAB showed the most intense peak at 1628 cm^{-1} compared to those prepared at 30 s, 60 s, and 120 s, as illustrated in Fig. 6.5 (a). Distinct Raman bands observed at approximately 449 cm^{-1}, 628 cm^{-1}, 1394 cm^{-1}, and 1617 cm^{-1} can be attributed to C-N-C skeletal bending, C-C and C-N stretching, and C-N-S skeletal deformation of MB molecules, respectively [31]. Following this, the NPCs substrate deposited for 180 s was selected to determine the low detection limit for MB. The same procedure was repeated for the NPCs samples prepared with CTAB, and it was observed that the NPCs deposited at 120 s showed the most intense peak at 1617 cm^{-1}, as depicted in Fig 6.5 (b), and selected for further investigations. Based on the morphological analysis, it has been observed that dendrites of the NPC structures can cluster together, forming SERS hot spots. The presence of numerous slender dendrites in the porous copper, particularly when combined with CTAB, results in reduced spacing between them. This closer arrangement facilitates the generation of more surface plasmons, which significantly enhances SERS activity. As a result, NPCs prepared with CTAB significantly enhance SERS activity.

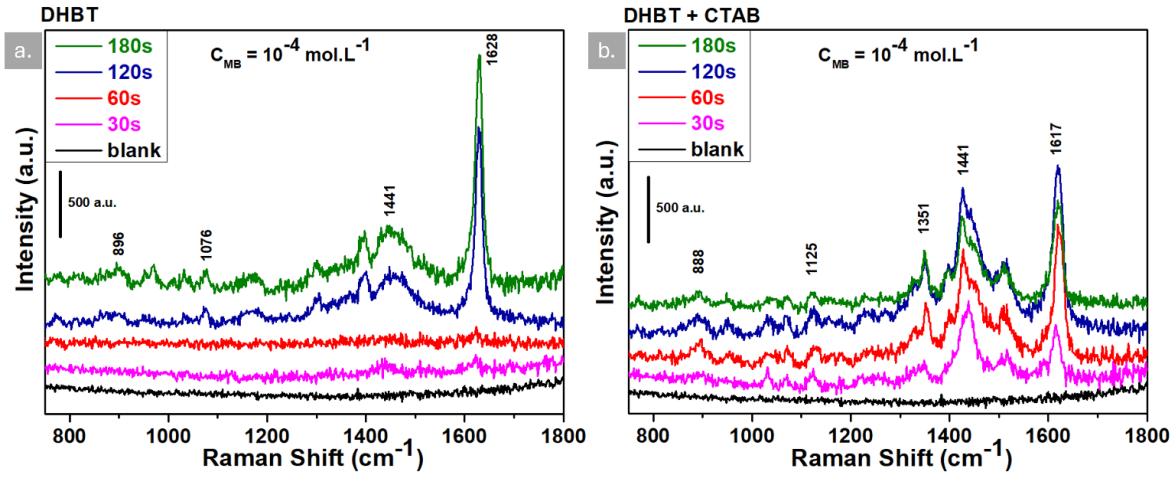

Figure 6.5: *Effect of deposition time on SERS active NPCs Substrate (a) NPCs without CTAB (DHBT) (b) NPCs with CTAB (DHBT + CTAB).*

Furthermore, the Raman spectra clearly show unique peaks associated with MB molecules, indicating that the NPC films exhibit effective SERS active sites throughout all the samples. The morphological analysis is illustrated in Fig. 6.1 (a' - h'). This observation suggests that longer deposition times promote the development of a more pronounced porous structure. Notably, the SERS activity is primarily influenced by the optimal parameters of the NPC deposits and the plasmonic surfaces within the porous copper framework. The decrease in thickness could potentially hinder the formation of SERS hot spots [32]. The peaks are less intense than 120 s, as illustrated in Fig. 6.5 (b).

The Raman spectra of MB were analyzed across a concentration range of 10^{-4} to 10^{-7} M to evaluate the SERS sensitivity of the NPC film. Two different types of NPC deposited films were used: one deposited at 180 s without CTAB and the other at 120 s with CTAB, as depicted in Fig. 6.6. In Fig. 6.6 (a), the spectra from the NPC deposited film for 180 s without CTAB

displayed a distinct peak that decreased in intensity as the MB concentration decreased from 10^{-4} M to 10^{-5} M. However, no peaks were observed at lower concentrations (10^{-6} M and 10^{-7} M), indicating a low detection limit of 10^{-5} M. In contrast, the samples containing CTAB exhibited a distinct peak at a lower concentration of 10^{-6} M, indicating a significant amplification of the Raman signal at this concentration. This highlights the critical role of CTAB in enhancing Raman signals, enabling the detection of prominent signals at lower concentrations compared to samples deposited without CTAB.

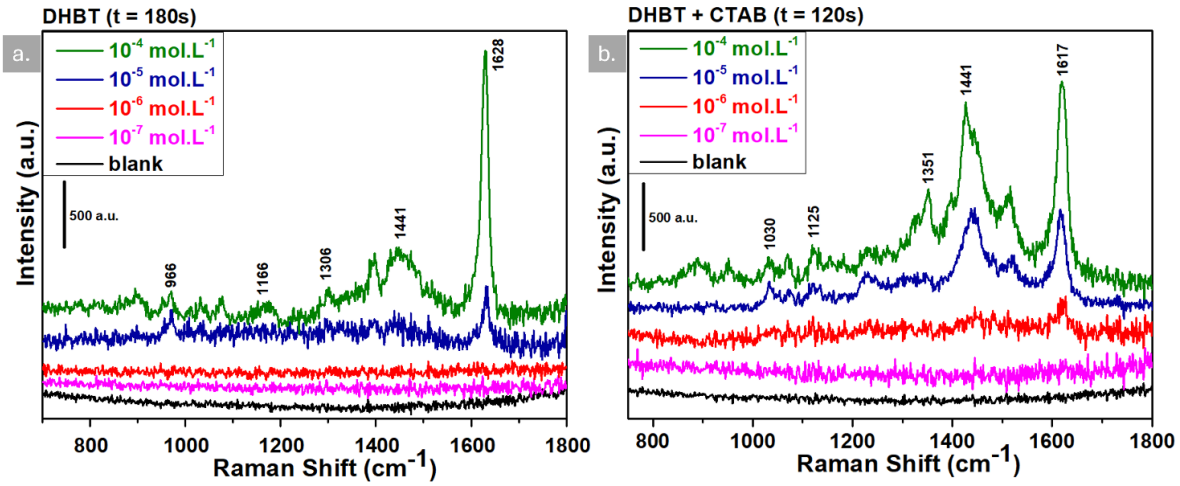

***Figure 6.6**: SERS sensitivity of MB using a concentration range of 10^{-4} – 10^{-7} using NPCs (a) NPCs without CTAB (b) NPCs with CTAB*

Additionally, a detailed comparison of the SERS active copper substrate prepared via different methods using the different analytes were performed in Table 6.2. Hu et al. [33] investigated the use of nanoporous copper (NPC) as a SERS substrate to enhance its enhancement factor (EF) for improved detection limits. In his study, Cu ion irradiation was employed to significantly enhance the EF of NPC resulting in a 4.4×10^4 increase in the EF and a detection limit of 10^{-4} M for rhodamine achieved by creating additional "hot spots" and roughening the NPC's surface. Diao et al. [34] employed co-sputtering Cu/Ti followed by dealloying process to synthesized nanoporous metals (NPMs) with tailored microstructures. The ideal NPC film demonstrated outstanding SERS performance for Rhodamine 6G, with a 10^{-9} M detection limit and strong consistency and repeatability. The EF was 4.71×10^7, which is higher than Au substrates and equivalent to Ag. Sai et al. [35] developed a cost-effective and sensitive SERS substrate by synthesizing CuO nanorods decorated with gold nanostructures. This innovative Au–CuO substrate demonstrated remarkable efficacy in identifying methylene blue at an extremely low concentration of 0.1 pM. Additionally, the SERS activity of the Au–CuO substrate exhibited impressive stability, maintaining approximately 80% of its performance after three recycling cycles.

Xu et al. [36] developed an advanced SERS substrate by fabricating copper nanoparticles (CuNPs)/silver nanowires (AgNWs) heterostructures through the vacuum thermal evaporation and solid-state ionic methods. These heterostructures exhibited remarkable sensitivity, capable of detecting melamine at an ultra-low concentration of 10^{-16} M. The integration of CuNPs and

AgNWs in a heterostructure design leverages the unique properties of both components, resulting in a highly efficient SERS substrate. In a separate study, Xu et al. [37] examined the SERS activity of rhodamine 6G (R6G) Raman probes on gradient porous copper (Cu) substrates. Their findings revealed an extraordinary EF of 6.63×10^{12}, along with a detection limit of 2.10×10^{-17} M, significantly outperforming other porous SERS substrates. The combination of CuNPs and AgNWs in a heterostructure configuration influences the unique properties of each component, resulting in a highly efficient SERS substrate.

Chen et al. [38] conducted a systematic investigation into the formation of nanoporous copper through the selective corrosion of a single-phase $Cu_{30}Mn_{70}$ alloy in HCl aqueous solutions. Their study demonstrated that controlling the nanopore size significantly enhanced the SERS performance of NPC. At the optimal nanopore size, the SERS enhancement factor achieved was approximately 1.85×10^5, comparable to that of NPG with a limit of detection (LOD) of 10^{-5} M for rhodamine and crystal violet. Li et al. [39] successfully fabricate free-standing nanoporous copper foils (NPCFs), with a thickness of approximately 1.4 μm and an area of up to 10 cm^2. Due to their nanoporosity, these NPCFs exhibited exceptional performance as SERS substrates, achieving an enhancement factor of 2.52×10^5 while detecting rhodamine at a concentration of 10^{-6} M.

Shao et al. [24] developed a novel approach to fabricate copper nanoparticles (CNPs) grafted directly on a silicon wafer. This method involves reducing copper ions using silicon-hydrogen bonds and assembling the CNPs in situ on the Si wafer surface. The resulting CNPs@Si substrate demonstrated excellent SERS performance, allowing the detection of rhodamine 6G at an ultra-low concentration of 10^{-9} M. A 2.29×10^7 SERS enhancement factor was achieved with a relative SD (standard deviation) of less than 20%, indicating good reproducibility across the substrate. Kowalska et al. [40] developed a novel approach to fabricate copper-based SERS platforms by depositing copper hydride (CuH) under high pressure. The enhancement factors calculated for malachite green isothiocyanate on these platforms ranged from 1.5×10^6 to 4.6×10^7, with a 10^{-6} M detection limit.

Yang et al. [30] employed a DHBT technique to fabricate dual-functional porous copper (Cu) films, enabling in situ monitoring of electrocatalytic reactions through SERS. These porous Cu films displayed exceptional sensitivity, with a detection limit of 10^{-7} M for methylene blue, while also demonstrating excellent reproducibility

***Table 6.2**: A detailed comparison of SERS active copper substrates*

Substrate	Shape/Structure	Analyte	LS/PS/Diameter	LOD (mol/L)	EF	Ref.
PCu	Copper sheet	MB	43.1 μm	10^{-9}	-----	[30]

NP-Cu	Ribbon	R6G	~ 1 µm	10^{-4}	4.4×10^{4}	[33]
NPC	Film	R6G	41.6 ± 9.2 nm	10^{-9}	4.7×10^{7}	[34]
CuO	Nanorods	MB	40 – 100 µm	10^{-14}	9.3×10^{8}	[35]
Cu/Ag	Nano heterostructure	melamine	10 – 50 nm	10^{-15}	4.8×10^{12}	[36]
GP-Cu	Laminated	R6G	~ 24 nm	10^{-17}	6.6×10^{12}	[37]
NPCu	Ribbon	R6G/ CV	~ 34 nm	10^{-5}	1.85×10^{5}	[38]
NPCFs	Foil	R6G	~ 200 nm	10^{-6}	2.52×10^{5}	[39]
Cu	Copper hybrid	MG isothiocyanate	~ 30 - 90 nm	10^{-6}	4.6×10^{7}	[40]
CNPs	Grafted on Si wafer	R6G	~ 20 nm	10^{-9}	2.29×10^{7}	[41]
NPCs	Cu Disks	MB	12 – 73 µm	10^{-6}	2.5×10^{3}	**This work**

NPC: nanoporous copper, LS: Ligament size, PS: pore size, LOD: limit of detection, EF: enhancement factor, GP-Cu: gradient porous copper, NPCFs: nanoporous copper films, CNPs: copper nanoparticles, MB: Methylene blue, PCu: Porous copper, R6G: Rhodamine 6G, CV: crystal violet.

These strategies have enabled the development of a cost-effective copper-based SERS substrates with average performances in terms of enhancement factors and detection limits, when compared with other copper-based substrate reported in the literature.

6.4 Conclusion

In this study, 3-D NPCs films were successfully fabricated using electrodeposition coupled with a DHBT approach, demonstrating their potential as effective SERS substrates for detecting the highly toxic dye methylene blue. The morphology of the NPC films was tailored in the presence of CTAB additives and adjusting the deposition time, both of which play crucial roles in creating bubble templates that drive the formation of the hierarchical structure. The deposition time and the presence or absence of CTAB significantly affect the SERS activity of the porous Cu films. The organic additive CTAB enhances the formation of NPCs films, resulting in a thinner pore structure and finer dendrites approximately in the range of 12.8 to 24 μm, which contribute to their superior SERS activity at a deposition time of 120 s. In contrast, nanoporous copper films prepared without CTAB demonstrated SERS performance at a longer deposition time of 180 s, resulting in a thicker dendritic structure that impacted their overall performance. Remarkably, the NPCs films exhibited high sensitivity of methylene blue having LOD 10^{-6} M with an enhancement factor of 2.5×10^3, good reproducibility and good activity for SERS detection. Furthermore, the film thickness and pore size of the copper films could be precisely tailored by varying both the electrodeposition time and the presence of the surfactant CTAB. The resulting NPCs film with varied pore sizes and wall thickness offers a simple and fast way for producing NPCs SERS substrates with adjustable morphology. The cost-effectiveness and facile fabrication process make the NPC deposited film a promising candidate for various SERS applications.

Reference

1. Zhu, P.; Wu, Z.; Zhao, Y. Hierarchical Porous Cu with High Surface Area and Fluid Permeability. *Scr Mater* 2019, *172*, 119–124.

2. Cao, C.; Cheng, J. Fabrication of Robust Surfaces with Special Wettability on Porous Copper Substrates for Various Oil/Water Separations. *Chemical Engineering Journal* 2018, *347*, 585–594.

3. Xue, Y.; Scaglione, F.; Rizzi, P.; Battezzati, L.; Denis, P.; Fecht, H.-J. Electrodeposited Platinum on De-Alloyed Nanoporous Gold with Enhanced Electro-Catalytic Performance. *Appl Surf Sci* 2019, *476*, 412–417.

4. Scaglione, F.; Xue, Y.; Celegato, F.; Rizzi, P.; Battezzati, L. Amorphous Molybdenum Sulphide@ Nanoporous Gold as Catalyst for Hydrogen Evolution Reaction in Acidic Environment. *J Mater Sci* 2018, *53*, 12388–12398.

5. Scaglione, F.; Alladio, E.; Damin, A.; Turci, F.; Baggiani, C.; Giovannoli, C.; Bordiga, S.; Battezzati, L.; Rizzi, P. Functionalized Nanoporous Gold as a New Biosensor Platform for Ultra-Low Quantitative Detection of Human Serum Albumin. *Sens Actuators B Chem* 2019, *288*, 460–468.

6. Jiang, J.; Lim, Y.S.; Park, S.; Kim, S.-H.; Yoon, S.; Piao, L. Hollow Porous Cu Particles from Silica-Encapsulated Cu 2 O Nanoparticle Aggregates Effectively Catalyze 4-Nitrophenol Reduction. *Nanoscale* 2017, *9*, 3873–3880.

7. Lv, J.; Jouny, M.; Luc, W.; Zhu, W.; Zhu, J.; Jiao, F. A Highly Porous Copper Electrocatalyst for Carbon Dioxide Reduction. *Advanced Materials* 2018, *30*, 1803111.

8. Ali, H.M. Experimental Investigation on Paraffin Wax Integrated with Copper Foam Based Heat Sinks for Electronic Components Thermal Cooling. *International Communications in Heat and Mass Transfer* 2018, *98*, 155–162.

9. Plowman, B.J.; Jones, L.A.; Bhargava, S.K. Building with Bubbles: The Formation of High Surface Area Honeycomb-like Films via Hydrogen Bubble Templated Electrodeposition. *Chemical Communications* 2015, *51*, 4331–4346.

10. Nam, S.; Jo, H.; Choe, H.; Ahn, D.; Choi, H. Development of Nanoporous Copper Foams by Chemical Dealloying of Mechanically Alloyed Al–Cu Compounds. *Mater Trans* 2014, *55*, 1414–1418.

11. Asnavandi, M.; Zhao, C. Hydrogen Bubble-Assisted Electrodeposition of Metal Nanoparticles from Protic Ionic Liquids for Electrocatalysis. *ACS Sustain Chem Eng* 2017, *5*, 85–89.

12. Pang, K.; Hou, Y.C.; Wu, W.Z.; Tian, S.D.; Sun, N.N. Control of the Morphology of Electrodeposited Three-Dimensional Copper Foam by Tuning the Pressure. *Sci China Chem* 2012, *55*, 1325–1329, doi:10.1007/s11426-012-4609-7.

13. Darayen, J.; Chailapakul, O.; Praserthdam, P.; Panpranot, J.; Tungasmita, D.N.; Boonyongmaneerat, Y. Porous Electrodeposited Cu as a Potential Electrode for Electrochemical Reduction Reactions of Co2. *Applied Sciences (Switzerland)* 2021, *11*, doi:10.3390/app112311104.

14. Vivegnis, S.; Delhalle, J.; Mekhalif, Z.; Renner, F.U. Copper–Zinc Alloy Electrodeposition Mediated by Triethanolamine as a Complexing Additive and Chemical Dealloying. *Electrochim Acta* 2019, *319*, 400–409, doi:10.1016/j.electacta.2019.07.007.

15. Shin, H.; Dong, J.; Liu, M. Nanoporous Structures Prepared by an Electrochemical Deposition Process. *Advanced Materials* 2003, *15*, 1610–1614.

16. Shin, H.-C.; Liu, M. Copper Foam Structures with Highly Porous Nanostructured Walls. *Chemistry of materials* 2004, *16*, 5460–5464.

17. Li, Y.; Jia, W.-Z.; Song, Y.-Y.; Xia, X.-H. Superhydrophobicity of 3D Porous Copper Films Prepared Using the Hydrogen Bubble Dynamic Template. *Chemistry of Materials* 2007, *19*, 5758–5764.

18. Sousa, E.; Silva, D.; De Los Ángeles, M.; Cámara, F.; Del, M.; Fernández-Poyatos, P.; Rahmati, F.; Sabouhanian, N.; Lipkowski, J.; Chen, A. Synthesis of 3D Porous Cu Nanostructures on Ag Thin Film Using Dynamic Hydrogen Bubble Template for Electrochemical Conversion of CO 2 to Ethanol. 2023, doi:10.3390/nano.

19. Du, D.; Lan, R.; Humphreys, J.; Sengodan, S.; Xie, K.; Wang, H.; Tao, S. Achieving Both High Selectivity and Current Density for CO2 Reduction to Formate on Nanoporous Tin Foam Electrocatalysts. *ChemistrySelect* 2016, *1*, 1711–1715.

20. Bommireddy, N.; Palathedath, S.K. Surfactant Mediated Electrodeposition of Copper Nanostructures for Environmental Electrochemistry: Influence of Morphology on Electrochemical Nitrate Reduction Reaction. *Journal of Solid State Electrochemistry* 2022, *26*, 2733–2742.

21. Hui, S.; Shaigan, N.; Neburchilov, V.; Zhang, L.; Malek, K.; Eikerling, M.; Luna, P. De Three-Dimensional Cathodes for Electrochemical Reduction of CO2: From Macro-to Nano-Engineering. *Nanomaterials* 2020, *10*, 1884.

22. Li, Y.; Jia, W.Z.; Song, Y.Y.; Xia, X.H. Superhydrophobicity of 3D Porous Copper Films Prepared Using the Hydrogen Bubble Dynamic Template. *Chemistry of Materials* 2007, *19*, 5758–5764, doi:10.1021/cm071738j.

23. Das, M.; Biswas, A.; Purkait, T.; Boruah, T.; Bhardwaj, S.; Das, S.K.; Dey, R.S. The Versatility of the Dynamic Hydrogen Bubble Template Derived Copper Foam on the Emerging Energy Applications: Progress and Future Prospects. *J Mater Chem A Mater* 2022, *10*, 13589–13624.

24. Shao, Q.; Que, R.; Shao, M.; Cheng, L.; Lee, S. Copper Nanoparticles Grafted on a Silicon Wafer and Their Excellent Surface-enhanced Raman Scattering. *Adv Funct Mater* 2012, *22*, 2067–2070.

25. Zhu, T.; Sun, Y.; Lu, W.; Wang, G.; Zhang, X.; Chen, S.; Zhang, C.; Li, Z.; Man, B.; Yang, C. Theoretical and Experimental Investigation of the Flexible Ag Nano-Tree@ Cu Mesh SERS Substrate. *J Alloys Compd* 2022, *908*, 164622.

26. Tan, Y.; Gu, J.; Xu, L.; Zang, X.; Liu, D.; Zhang, W.; Liu, Q.; Zhu, S.; Su, H.; Feng, C. High-density Hotspots Engineered by Naturally Piled-up Subwavelength Structures in Three-dimensional Copper Butterfly Wing Scales for Surface-enhanced Raman Scattering Detection. *Adv Funct Mater* 2012, *22*, 1578–1585.

27. Nikolić, N.D.; Popov, K.I.; Pavlović, L.J.; Pavlović, M.G. The Effect of Hydrogen Codeposition on the Morphology of Copper Electrodeposits. I. The Concept of Effective Overpotential. *Journal of Electroanalytical Chemistry* 2006, *588*, 88–98.

28. Song, Y.; Hu, J.; Tang, J.; Gu, W.; He, L.; Ji, X. Real-Time X-Ray Imaging Reveals Interfacial Growth, Suppression, and Dissolution of Zinc Dendrites Dependent on Anions of Ionic Liquid Additives for Rechargeable Battery Applications. *ACS Appl Mater Interfaces* 2016, *8*, 32031–32040.

29. Shin, H.-C.; Liu, M. Copper Foam Structures with Highly Porous Nanostructured Walls. *Chemistry of materials* 2004, *16*, 5460–5464.

30. Yang, H.; Hao, X.; Tang, J.; Jin, W.; Liu, C.; Hou, H.; Ji, X.; Hu, J. Dual-Functional Porous Copper Films Modulated via Dynamic Hydrogen Bubble Template for in Situ SERS Monitoring Electrocatalytic Reaction. *Appl Surf Sci* 2019, *494*, 731–739, doi:10.1016/j.apsusc.2019.07.241.

31. Naujok, R.R.; Duevel, R. V; Corn, R.M. Fluorescence and Fourier Transform Surface-Enhanced Raman Scattering Measurements of Methylene Blue Adsorbed onto a Sulfur-Modified Gold Electrode. *Langmuir* 1993, *9*, 1771–1774.

32. Hu, C.; Shen, J.; Yan, J.; Zhong, J.; Qin, W.; Liu, R.; Aldalbahi, A.; Zuo, X.; Song, S.; Fan, C. Highly Narrow Nanogap-Containing Au@ Au Core–Shell SERS Nanoparticles: Size-Dependent Raman Enhancement and Applications in Cancer Cell Imaging. *Nanoscale* 2016, *8*, 2090–2096.

33. Hu, Z.; Wang, J.; Li, R.; Xu, C.; Liu, X.; Wang, Y.; Fu, E.; Lu, Z. Ion Irradiation-Enhanced Raman Scattering on Nanoporous Copper. *Langmuir* 2018, *34*, 13041–13046, doi:10.1021/acs.langmuir.8b02764.

34. Diao, F.; Xiao, X.; Luo, B.; Sun, H.; Ding, F.; Ci, L.; Si, P. Two-Step Fabrication of Nanoporous Copper Films with Tunable Morphology for SERS Application. *Appl Surf Sci* 2018, *427*, 1271–1279, doi:10.1016/j.apsusc.2017.08.117.

35. Sai, C.D.; Nguyen, Q.H.; Tran, T.N.A.; Nguyen, T.B.; Do, H.H.; Vu, T.D. CuO Nanorods Decorated Gold Nanostructures as an Ultra-Sensitive and Recyclable SERS Substrate. *Mater Chem Phys* 2023, *293*, 126962.

36. Xu, D.; Zhang, T.; Zhang, S.; Li, J.; Yang, W.; Jiang, H. Centimeter Level High Surface Roughness Copper/Silver Nanoheterostructures for Highly Sensitive SERS Detection. *J Solid State Chem* 2023, *321*, 123916.

37. Xu, Z.; Erinomo, A.M.; Dan, Z.; Qin, F.; Chang, H. Flexible SERS Substrates with Gradient Porous Cu Structure Dealloying from the Thermal Diffusion Couples of Al/Cu Stacking Foils. *Chemical Engineering Journal* 2024, *490*, doi:10.1016/j.cej.2024.151871.

38. Chen, L.Y.; Yu, J.S.; Fujita, T.; Chen, M.W. Nanoporous Copper with Tunable Nanoporosity for SERS Applications. *Adv Funct Mater* 2009, *19*, 1221–1226, doi:10.1002/adfm.200801239.

39. Li, M.; Su, Y.; Zhao, J.; Geng, H.; Zhang, J.; Zhang, L.; Yang, C.; Zhang, Y. One-Pot Preparation of Thin Nanoporous Copper Foils with Enhanced Light Absorption and SERS Properties. *CrystEngComm* 2015, *17*, 1296–1304, doi:10.1039/c4ce01967a.

40. Kowalska, A.A.; Kaminska, A.; Adamkiewicz, W.; Witkowska, E.; Tkacz, M. Novel Highly Sensitive Cu-Based SERS Platforms for Biosensing Applications. *Journal of Raman Spectroscopy* 2015, *46*, 428–433, doi:10.1002/jrs.4674.

41. Shao, Q.; Que, R.; Shao, M.; Cheng, L.; Lee, S.T. Copper Nanoparticles Grafted on a Silicon Wafer and Their Excellent Surface-Enhanced Raman Scattering. *Adv Funct Mater* 2012, *22*, 2067–2070, doi:10.1002/adfm.201102943.

CHAPTER VII

Cost-Effective and Sustainable Metastable White Cast Iron Powder for Textile Dye Removal

7.1 Introduction

The approach to clean water is crucial for marine ecosystems, human populations, health, and sustainability. Sadly, abundant water sources are tainted due to various human activities [1]. A significant contributor in this case is the discharge of hundreds of tons of different dyes to environment annually by many industries like plastics, leather, textiles, cosmetics, food, pharmaceuticals, and paper [2]. Among the above-mentioned, textile industry stands out as the leading source, which releases almost 15-20% of the dyes to environment without any appropriate treatment [3]. The dyes are intricate materials typically categorized into various types according to their chemical makeup and uses. Azo dyes represent a major category of synthetic dyes dominating the worldwide dye industry, accounting for more than 70% of the dye production globally [4]. The reactive red dye has wide use in textile industry because of its strong stability and resistance to light and chemicals, making it a popular choice for numerous industrial applications [5].

In addition to the extensive use, the azo dyes pose serious environmental challenges. The azo dye can persist in the environment for long periods because its breakdown products possess toxic and carcinogenic characteristics. The detrimental impacts are linked to environmental issues and present significant dangers to both marine ecosystems and human well-being [6]. Consequently, creating appropriate and efficient treatment strategies is essential to stop the discharge of pollutants and harmful substances into the environment. Nonetheless, traditional approaches for treating dyed wastewater frequently fail to ensure adequate elimination of these compounds. Due to the strong electron bond within the azo group dyes makes them resistant to biodegradation, often resulting in the production of toxic transitional compounds such as aromatic amine [7–9]. Along these lines, the absorption methods are also infrequently utilized because of the generation of sludge and the need to replenish the absorbent [10]. While certain conventional chemical techniques, such as ozone (O_3) and hypochlorite oxidation, prove effective in dye decolorization, they may incur high costs related to equipment and materials [11]. As a result, creating cost-effective, efficient, and environmentally friendly materials to decompose azo dyes presents significant challenges. The zero-valent iron (ZVI) is a transition metal that can reduce dye degradation effectively by breaking azo bonds through redox reactions with the iron atoms. It is widely favored due to its affordability, high efficiency, safety, and reusability [12,13].

Recent advancements suggest that increasing the certain surface area of the ZVI significantly enhances its efficiency in breaking down azo dyes [14]. A potentially effective approach includes using nano-ZVI iron powders, which have some limitations, including their tendency to oxidize quickly and the requirement for extended reaction times to achieve the intended outcome. This method is effective at low pH levels [15]. A novel method involving cast iron

was introduced for wastewater treatment to overcome the limitations of traditional methods and conventional ZVI powder. These kinds of materials are cost-effective, readily available, and shown as effective reductive agents for efficiently breaking down dye molecules. Former studies highlighted the substantial potential of the cast iron in handling a variety of inorganic and organic pollutants in wastewater, like nitroaromatic compounds, dyes, and heavy metals. Wanner and colleagues demonstrated that the grey cast iron can be particularly effective in reducing Cr (VI) [16]. Fan and colleagues showed that scrap cast iron, in the presence of dissolved oxygen, effectively behaves toward neutral wastewater with 2,4-dinitrotoluene (2,4-DNT). They observed that the scrap cast iron demonstrates great reactivity in reducing 2,4-DNT by achieving over 80% conversion rates [17]. Oh et al. reported that the cast iron achieved perchlorate removal up to 98% under microwave radiation in just one hour. This superior performance highlights its enhanced reactivity and dispersion compared to the traditional ZVI, and significantly improved degradation rate [18].

Additionally, Fe-based nanocrystalline ribbons are significantly improved after the annealing, particularly in applications related to catalysis. Recent research highlights their superior ability in the dye degradation of azo dyes and makes them considerably promising materials for environmental remediation. For instance, Wang et al. studies have shown that annealed $Fe_{82.65}Si_4B_{12}Cu_{1.35}$ alloys, characterized by their multiple crystalline phases, are notably more efficient at removing the color from the azo dye Direct Blue 2B as compared to the amorphous ribbon [19]. This improvement suggests that the modifications in structure brought about by the annealing process enhance the catalytical activities. In contrast, Chen et al. discovered that nanocrystalline ribbons composed of $(Fe_{73.5}Si_{13.5}B_9Nb_3Cu_1)_{91.5}Ni_{8.5}$ exhibit an exceptionally high rate of degradation efficiency that is attributed to the creation of nanoscale galvanic cells between different nanocrystalline phases and the amorphous matrix, which aids in better electron transfer [20]. Moreover, $Fe_{78}Si_9B_{13}$ ribbons when annealed it form self-activated galvanic cells among intermetallic components, showing outstanding catalytic effectiveness in breaking down methylene blue [21]. These findings underscore the importance of phase interactions in enhancing catalytic efficiency and indicate a promising avenue for utilizing these materials in wastewater treatment and other environmental applications. These reports focus on the remarkable reactivity of the cast iron as a comparison to traditional ZVI, demonstrating its effectiveness in treating textile effluents with high dye concentrations and its strong potential for wastewater treatment. Consequently, optimizing the surface area and morphology of ZVI for enhancement of azo dye-degradation has developed a critical area of research. Our focus is on developing cost-effective ZVI materials capable of efficient azo dyes degradation.

In the previous study carried out in 2015 by our team [22], the dye degradation efficiency of two different azo dyes, i.e., ethyl orange and direct blue-6, was investigated using ball-milled iron powders derived from the same cast iron introduced in the current research, tested after 8 and 24 hours. The previous study employed a ball milling process without a controlled atmosphere, which constrained the effectiveness of the results. Nevertheless, degradation tests performed at room temperature showed promising outcomes. Building on these findings, our aim was to optimize the material synthesis. By maintaining the ingot's original composition

and utilizing melt-spinning process, we refined the ball milling techniques. The upgraded ball miller now operates in an argon atmosphere, effectively preventing oxidation of the powders before use. This enhancement produced smaller particle sizes while protecting the powders from oxidation, resulting in significantly improved efficiency of degradation. These optimized powders were then applied to degrade Sandal-fix Red C4BLN, which is a hazardous textile dye but commonly used.

This chapter presents an in-depth analysis of the cost-effective synthesis of white cast iron powder (WCI-P) derived from an iron-based metastable alloy ($Fe_{82}C_{15}Si_3$) produced through rapid solidification.The application of the melt spinning technique enabled a solidification rate of 10^6 K/s, which substantially enhanced the microstructural refinement of the material. Consequently, zero-valent iron grains are uniformly dispersed within the alloy matrix alongside cementite (Fe_3C) phases. The conversion of white cast iron ribbons (WCI-R) into fine powders is due to their brittle nature, designated as WCI-P, which was utilized for the degradation of the reactive red 195A dyes. Key parameters influencing degradation efficiency, including powder reusability, temperature for reaction, and initial dye concentration, were systematically investigated. The WCI-P powders demonstrated exceptional catalytic activity, completely degrading solution of reactive red 195A dye at 70 °C within just fifteen minutes. This remarkable efficiency is due to the larger surface area of the WCI-P, aiding fast degradation kinetics. The synthesis of cost-effective and straightforward WCI-P highlights its potential as an advanced catalyst for high-efficiency of dye-degradation applications.

7.2 Experimental Methodology

7.2.1 Preparation of white cast iron powder

An iron ingot with the atomic composition of $Fe_{82}C_{15}Si_3$ was developed through arc-melting high-purity elements in an Ar atmosphere. The master alloy was quickly solidified using a melt-spinning device [23], producing brittle WCI-R that dimension of the WCI-R is 1 cm in width and a thickness range of 25 μm. These ribbons were then processed into fine powders (WCI-P) using a controlled ball-milling method to enhance catalytic properties. The ball-milling process was performed using 5 mm zirconia balls in a zirconia jar, operating at 260 rpm in an argon atmosphere for 24 hours to prevent the powder from oxidation before its application. A 1:1 mass ratio was maintained for ball to powder. The resulting WCI-P powder achieved a 36 μm average particle size. The elemental composition, surface morphology, and microstructure of both the WCI-R and WCI-P samples were analyzed using scanning electron microscopy and energy-dispersive X-ray spectroscopy. For SEM analysis, the WCI-R samples were etched in a 4% nitric acid in ethanol for 5 s, then dried and stored. Structural analysis of both WCI-R and WCI-P samples was also conducted by diffractometric technique.

7.2.2 Particle size distribution

The distribution of the particle size of WCI-P was determined by analyzing 150 particles using SEM images captured at various magnifications, including low magnifications starting from 100x, 150x, and 500x toward the high magnifications of 1000x, 1500x, 3000x, and 5000x. The

analysis focused on particle sizes between 10 µm and 500 µm. Due to the irregular shape of the particles, their distribution was measured using ImageJ software.

7.2.3 Degradation analysis

The textile dye C4BLN Sandal-fix Red sourced from Sandal Textile Dyestuff in Faisalabad, Pakistan was selected for the degradation experiments. The detailed chemical structure and properties of Red 195A are summarized in Table 7.1.

***Table 7.1**: Comprehensive analysis of Reactive Red 195A.*

Common name	**Color index**	**MW (g/mol)**	**λ max (nm)**	**MF**
S.F. Red C4BLN	Reactive Red 195A	1034.3	540	$C_{31}H_{20}ClN_7Na_4O_{16}S_5$

Reactive red 195A dye solutions were prepared for the dye degradation analysis by dissolving the necessary quantities of dye in Milli-Q water for different concentrations of 0.01 g/L, 0.03 g/L, and 0.05 g/L. To examine the impact of dye concentration on degradation behavior, 0.1 g of WCI-P was added to 50 mL of each solution, and the experiment was carried out at 70°C with continuous stirring at 200 r/min. Further experiments were conducted using a 0.01 g/L dye solution at 25°C, 50°C, and 70°C while keeping the same stirring settings to assess the impact of temperature on degradation. In addition to this, to evaluate absorbance over the 400–650 nm range, samples were taken at regular intervals using a quartz cuvette and a UV-visible-NIR spectrophotometer, with a model of Agilent Cary 5000 from Santa Clara, CA, USA. To guarantee repeatability, each experiment was run twice. The following formulas [24,25] were used to determine the degradation efficiency and concentration of the residual solution.

$$C_t = C_o \times {}^{\lambda_{maxt}}/_{\lambda_{max0}}, \qquad \%R = \frac{(C_o - C_t)}{C_o} \times 100$$

%R represents the efficiency of dye degradation, where λmax refers to the absorbance peak intensities at the initial time t_0 and at a specific time t. C denotes the dye solution concentration before and after the given time t, respectively.

7.3 Results

The analysis of the chemical composition for both samples of white cast iron i.e, WCI-R and WCI-P was conducted using EDS, which confirmed that they align with the nominal composition of the $Fe_{82}C_{15}Si_3$ at%, as detailed in Table 7.2 below.

***Table 7.2**: Atomic % composition of WCI-P and WCI-R from EDS analysis.*

Composition	Fe	Si	C
WCI-P	84.3 ± 3.7	1.9 ± 0.4	14.6 ± 3.6
WCI-R	84.1 ± 1.6	1.8 ± 0.6	14.0 ± 1.7

The XRD analysis was performed on the WCI-R from both the air and wheel sides and WCI-P before and after dye degradation. Fig. 7.1 shows that both WCI-R and WCI-P consist of three distinct phases: ferrite, cementite, and retained austenite [22]. The α-Fe (ferrite) is the dominant phase and has a body-centered cubic (bcc) structure [PDF: 00-006-0696], which shows a limited number of peaks in the XRD pattern due to its high symmetry. Low-intensity peaks correspond to the Fe_3C of the cementite phase [PDF: 00-034-0001], which exhibits an orthorhombic structure. Additionally, some peaks may suggest a minor presence of retained austenite resulting from rapid solidification.

Following the dye degradation, the high-intensity peaks corresponding to iron oxides (Fe_2O_3) (PDF: 00-019-0629) are observable in the recycled powder pattern. This suggests that oxidation occurred during the degradation process. The variations in reflection intensities on opposite sides of the WCI-R are likely attributed to rapid solidification, which encourages grain growth in alignment with the direction of heat dissipation. Ball milling did not alter phase composition, as the WCI-P pattern shows consistent angular positions for most reflections, although a general broadening of peaks and loss of orientation might occur due to reduced scattering domain size from plastic deformation, resulting in an increased defect density and the emergence of low-angle grain boundaries.

After seven degradation cycles, peaks corresponding to the α-Fe phase display reduced the relative intensity as compared to those of the Fe_2O_3 phase. Estimating the relative quantities of these phases by analyzing the intensities of the primary peaks reveals that Fe_2O_3 makes up about 60%, while ferrite accounts for roughly 40%. Quantifying cementite is challenging due to its low scattering factor and peak broadening caused by plastic deformation during ball milling. Cementite, being an oxidized form of iron, likely does not contribute to the dye degradation process. This analysis suggests that more than 50% of ferrite undergoes oxidation following the 7 degradation cycles which may correlate with a decrease in degradation efficiency.

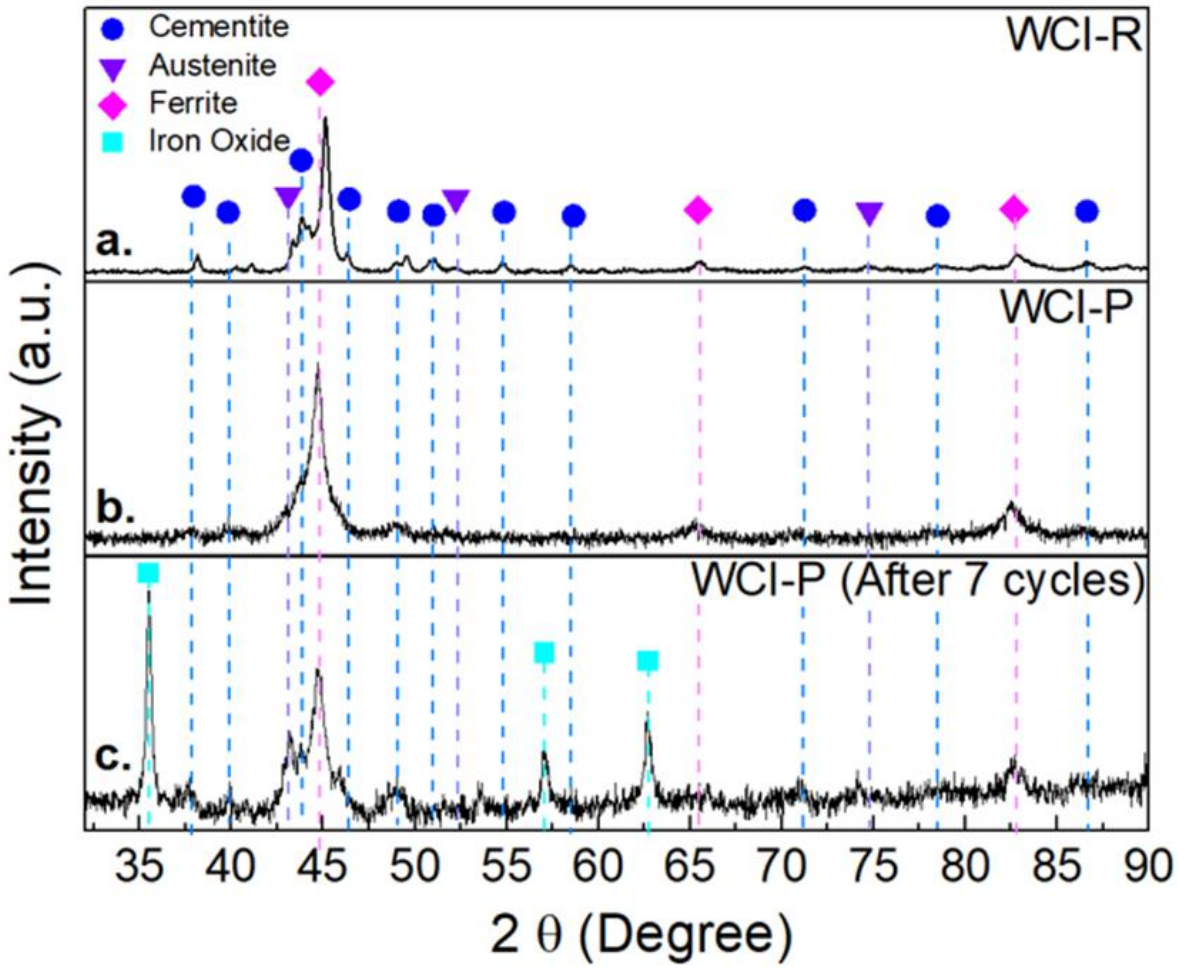

***Figure 7.1**: XRD analysis of (a) WCI-R, (b) WCI-P, and (c) WCI-P following the 7th cycle of dye degradation.*

The SEM images of WCI-R provide valuable insights into the microstructure of the as-cast iron ribbon, specifically on both sides (wheel and air). The analysis reveals the presence of lamellar crystals of ferrite and cementite on both surfaces with larger crystal formations observed on the air side as shown in Fig. 7.2. Fig. 7.2 (a, b) illustrates the microstructure of the air side, while Fig. 7.2 (c, d) focus on the wheel side. Ferrite (zero-valent iron) appears as lamellae, with an approximate thickness of 0.111 µm on the air side and 0.070 µm thickness on the wheel side. Furthermore, the surface morphology of WCI-P offers numerous reaction sites for dye molecules, thereby enhancing its reactivity and dye degradation efficiency.

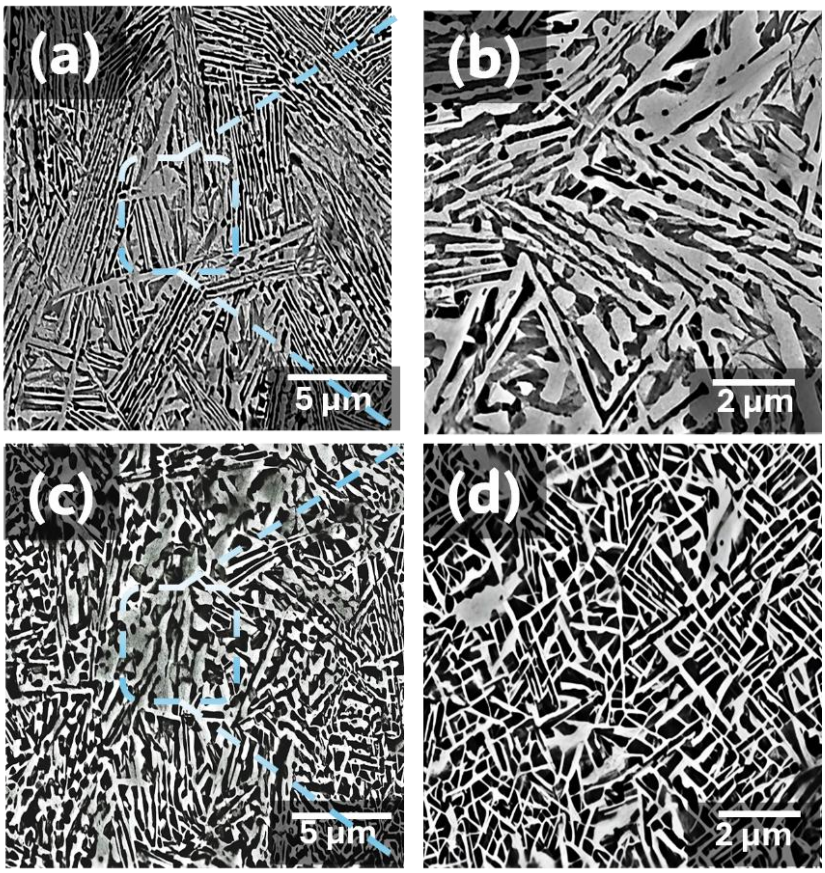

Figure 7.2*: SEM images of WCI-R: (a, b) air side and (c, d) wheel side at low and high magnifications.*

Fig. 7.3 (a), (b), and (c) shows the surface morphology of the WCI-P before dye degradation taken at different magnifications. The particles of WCI-P exhibit an irregular shape and bimodal size distribution, as illustrated in Fig. 7.3 (d). This distinctive morphology, along with a large proportion of particle sizes below 50 µm, allows WCI-P to offer an extensive surface area when interacting with the dye solution. This structure provides abundant reaction sites, significantly increasing the reaction rate.

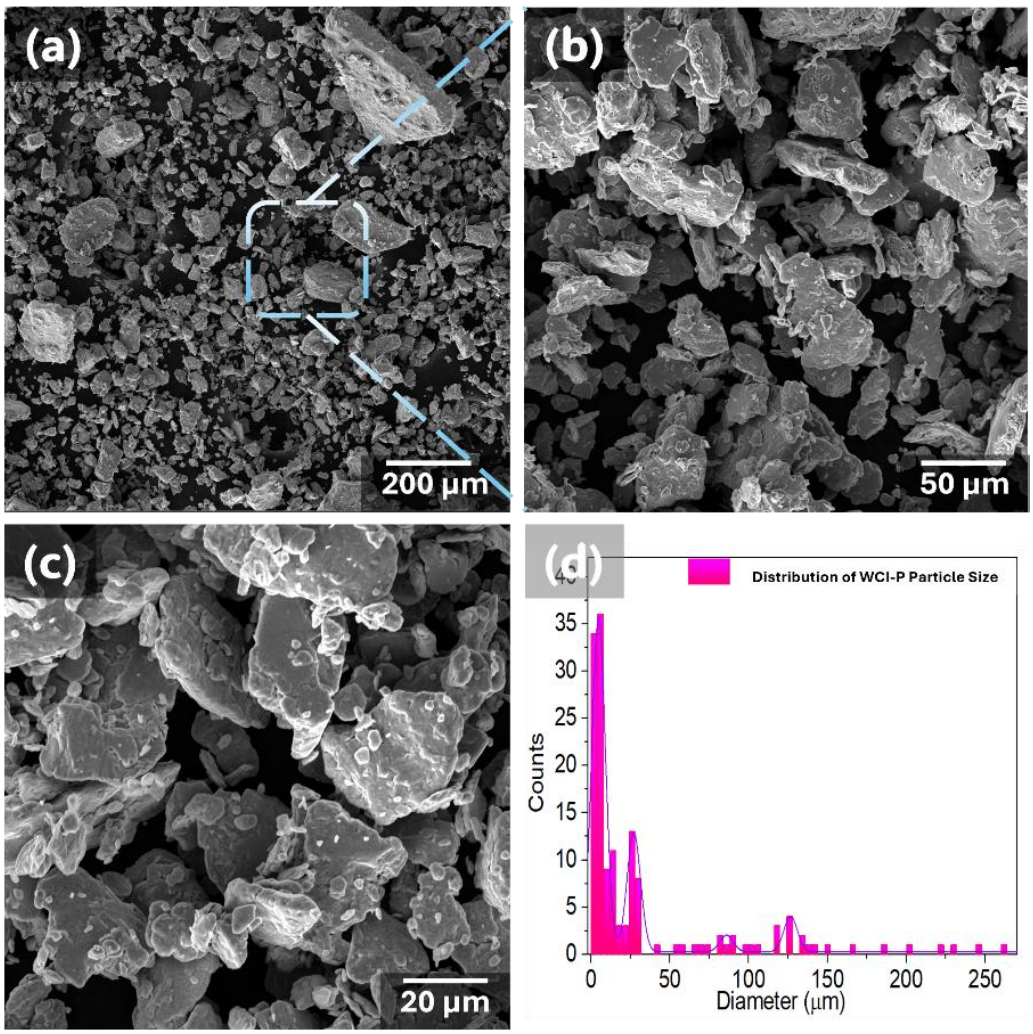

Figure 7.3: *SEM analysis of WCI-P: (a) morphology, (b, c) detailed views, and (d) particle size distribution.*

Following the dye degradation, the surface structure of WCI-P is analyzed and shown in Fig. 7.4. Fig. 7.4 (a, b) illustrates the deposition of RR195A dye and its byproducts on the WCI-P surface. Additionally, the structural morphology of WCI-P was analyzed across multiple reuse cycles. Fig. 7.4 (c) and (d) show the WCI-P surface after the seven reused cycles, revealing a transformation from initially smooth and irregular structural features to a noticeably rougher surface. These figures illustrate that the surface has changed from having smooth and uneven structural features to having a different surface texture. The reduction in degradation effectiveness after the 7^{th} cycle is likely due to oxide formation from ferrite oxidation and the accumulation of RR195A dye residues on the WCI-P surface during the degradation process.

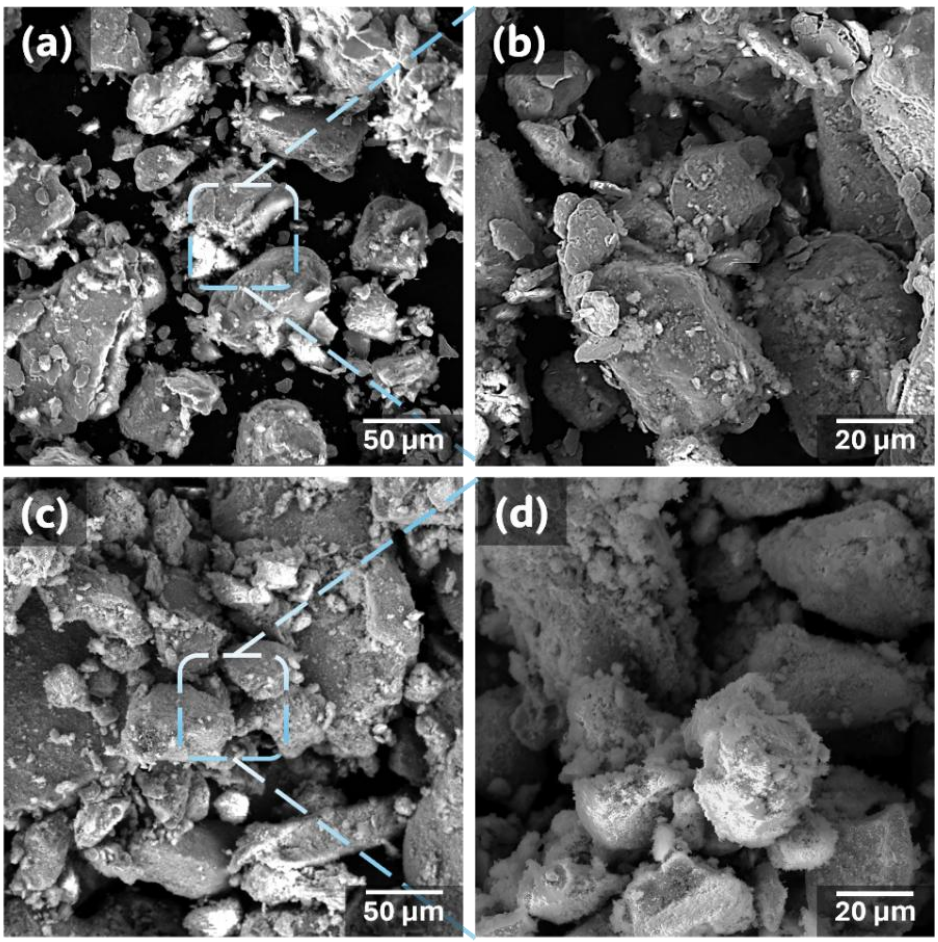

Figure 7.4: *SEM of WCI-Powder after the dye degradation: at 50°C (a, b), after 7th cycle at 70°C (c, d).*

The XRD pattern of WCI-P after the seventh cycle of dye degradation, as shown in Fig. 7.1 c, highlights the crucial role of α-Fe^0 in breaking down the azo bond in reactive red 195A dye. Fe^0 serves as an electron donor, providing electrons to the electron-deficient -N=N- group, thus facilitating the decomposition of RR 195A [26].

7.3.1 Optimization of dye degradation by Absorbance concentration standard curve

A standard curve of absorbance versus concentration was developed to evaluate the dye degradation efficiency accurately, as shown in Fig. 7.5. A primary solution of RR 195A dye served as the basis for subsequent dilutions, prepared from a stock solution of 100 ppm. This will ensure precision for later measurements. Ten dilutions were prepared with concentrations ranging from 0.5 ppm to 100 ppm, creating a broad spectrum of known concentrations that are essential for constructing a detailed standard curve to define the relationship between absorbance and concentration. Absorbance measurements for each dilution were taken using a UV-visible spectrometer. Fig. 7.5(a) visually represents the absorbance spectra of reactive red 195A dye solutions at varying concentrations. The absorbance values, plotted against their corresponding concentrations, are visually represented in Fig. 7.5(a) and clearly illustrate the correlation between absorbance and reactive red 195A dye concentrations. The standard curve,

shown in Fig. 7.5 (b), was constructed by plotting the absorbance of each solution measured at the maximum wavelength of 540 nm.

The calibration curve shows a clear linear relationship between absorbance and concentration, with an adjusted R^2 value of 0.998. This high R^2 indicates a strong fit with the experimental data, aligning well with Beer's Law, which establishes that absorbance is directly proportional to concentration. This result highlights the accuracy of the spectrophotometric analysis and its applicability in environmental monitoring and remediation.

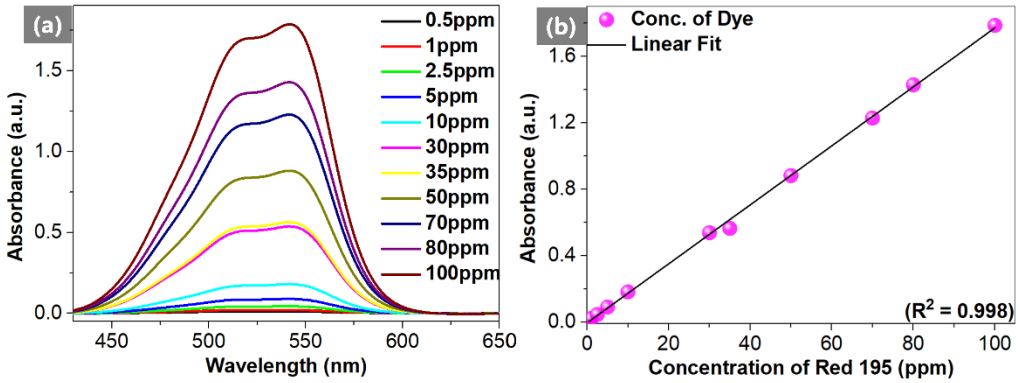

***Figure 7.5**: the absorbance-Concentration curve: (a) UV-Vis analysis of RR 195A, (b) standard curve conc. Vs Absor.*

7.3.2 Effect of Reaction Temperature

The temperature of the dye solution significantly influenced the degradation reaction and provided valuable information about the degradation mechanism. This study evaluated the degradation efficiency by varying the reaction temperature from 25 °C to 50 °C, and 70 °C using 0.1 g of WCI-P and a 0.01 g/L reactive red 195A dye solution and stirred at 200 r/min. Fig 7.6 illustrates the effect of temperature on dye concentration and degradation rate. The UV-visible analysis of 10 ppm dye degradation, presented in Fig. 7.6 (a, c, and e), shows a significant increase in degradation efficiency from 68% at 25 °C to 93.88% at 70 °C. This increase notably reduced the time required for complete degradation, from 24 hours at 25 °C to just 30 minutes at 50 °C. These results highlight a clear relationship between temperature and degradation rate, as depicted in Fig. 7.6 (b, d, and f).

This acceleration aligns with the Arrhenius equation, explaining that higher temperatures increase atomic activity, creating more reactive sites and enhancing the degradation rate [27]. Previous studies have supported this finding. Dizge et al. reported that increasing the temperature from 293 K to 323 K raised the adsorption capacity of Remazol red 133 dyes from 42.4 mg/g to 80.1 mg/g [28]. Similarly, Fan et al. studied that increasing the temperature from 293 K to 313 K enhanced the degradation rate of methylene orange dye from 72% to 98% [29]. Consistent with previous results, this experiment showed that a 10 ppm dye solution concentration dropped to 0.3 ppm after 30 min. of treatment at 50 °C and 0.62 ppm after just 15 min. at 70 °C. These results support a favorable relationship between temperature and the dye degradation rate.

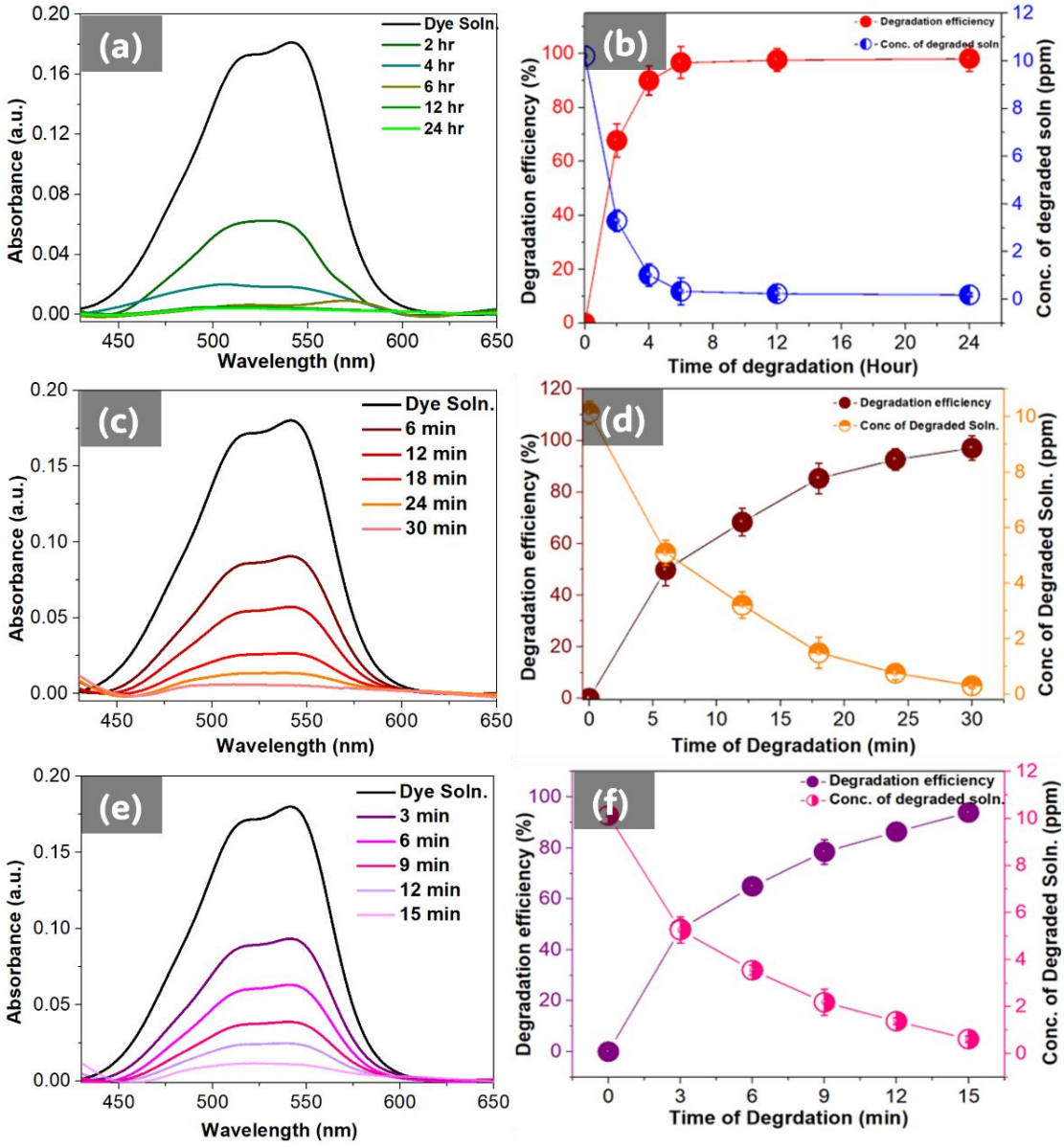

Figure 7.6: *Effect of temperature on dye degradation: (a, c, e) UV-Vis at 25°C, 50°C, and 70°C , (b, d, f) degradation efficiency and concentration*

7.3.3 Effect of dye Concentration

The degradation rate of RR 195A dye was analyzed at different concentrations of 10 ppm, 30 ppm, and 50 ppm under constant conditions: 0.1 g WCI-P, 70 °C reaction temperature, and 200 r/min stirring speed. Fig. 7.7 displays the UV-visible analysis, solution concentration, and degradation efficiency data. The results indicate a gradual decrease in degradation rate as dye concentration increased from 10 ppm to 50 ppm, likely due to the limited number of reactive sites on WCI-P. The available reactive sites were sufficient at 10 ppm for dye adsorption, leading to faster degradation. Complete degradation was achieved for 30 ppm and 50 ppm solutions within 60 and 120 minutes with efficiencies of 98.9% and 99.8%, respectively, over extended reaction times. Additionally, the dye concentration of solutions was tracked, and as shown in Fig. 7.7 (b, d, and e), concentrations decreased to 0.1 ppm with an increase in reaction

time [30]. These findings suggest that WCI-P requires a longer time to break down RR 195A dye as the concentration increases. At higher dye concentrations, without a proportional increase in reactive sites or reaction time, the availability of sites for dye adsorption becomes restricted. This limitation results in stronger repulsive interactions between the adsorbent surface and the already adsorbed dye molecules, ultimately lowering the degradation rate [31]. Supporting these findings, Natarajan et al. observed in another study that as the initial concentration of Rhodamine Blue dye increased, the degradation efficiency of bismuth-doped TiO_2 nanotubes dropped from 96% to 51%. This decrease is attributed to stronger adsorption forces at higher dye concentrations, which aid in overcoming the mass transfer resistance between the liquid and solid phases [32].

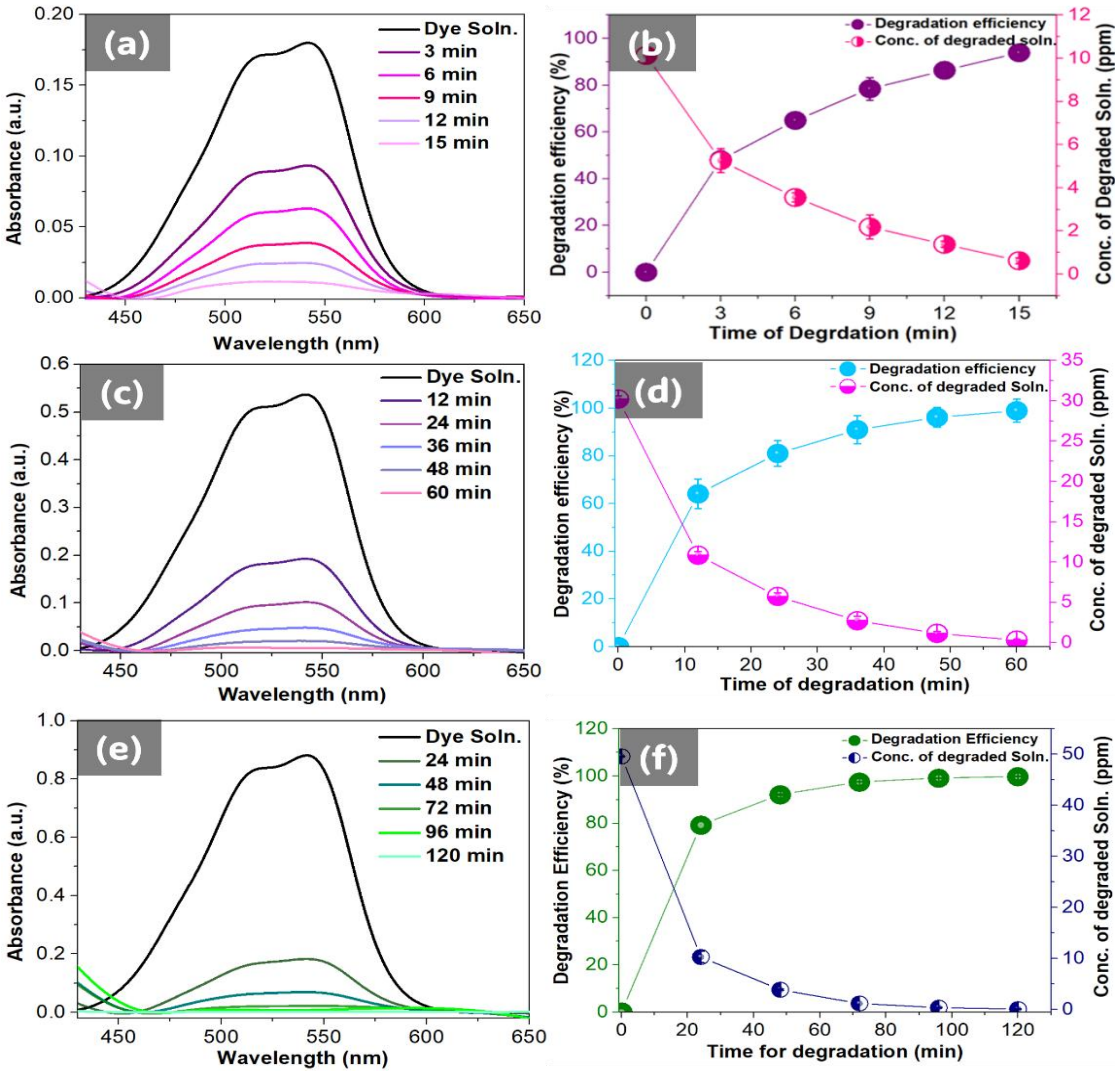

Figure 7.7: *Effect of concentrations on dye degradation: (a, c, e) UV-Vis for 10 ppm, 30 ppm, and 50 ppm dye at 70°C, (b, d, f) degradation efficiency and concentration.*

7.3.4 Reusability and stability of WCI-P

The reusability and stability of WCI-P were assessed for the degradation of reactive red 195A dye through multiple degradation cycles. Each cycle utilized a fixed amount i.e., 0.1 g of WCI-

P in a 10 ppm (0.01 g/L) dye solution at a maintained temperature of 70 °C, with a reaction time of 15 minutes per cycle. The UV-visible analysis of the recycled dye solution was presented in Fig. 7.8 (a). After each cycle, WCI-P was recovered from the reaction solution using magnetic separation, washed with MilliQ water, dried, and stored in an Eppendorf tube for reuse. As shown in Fig. 7.8 (b), a complete dye degradation of the RR 195A solution was achieved within 15 minutes, even after seven cycles. This confirms that WCI-P can be reused effectively for at least seven cycles without significant loss in degradation efficiency. Furthermore, a 10-minute sonication step was incorporated to enhance degradation efficiency and improve the stability of WCI-P.

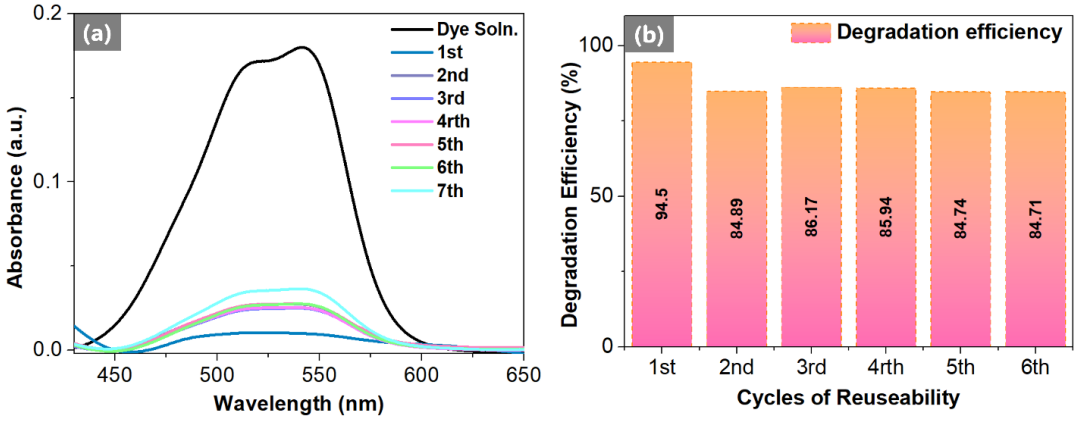

Figure 7.8: *Reusability of WCI-P: (a) UV-Vis analysis, (b) efficiency degradation.*

The sonication process facilitated the release of all dye molecules adsorbed onto the powder, effectively demonstrating the desorption phenomenon, as shown in Fig. 7.9. This ensured that there were empty reactive sites available for further reactions. The remarkable efficiency of WCI-P in removing azo dyes is widely attributed to its exceptional ability to integrate both the initial adsorption and subsequent reduction processes. This is made possible by the iron's distinctive electron configuration and magnetic characteristics [33]. Additionally, the reduction mechanism of azo dyes involves a redox interaction between the Fe atoms in WCI-P and the (N=N)– bonds in the dye molecules [34]. This reaction breaks the dye molecule into aromatic amines [35] and other byproducts such as aniline [36].

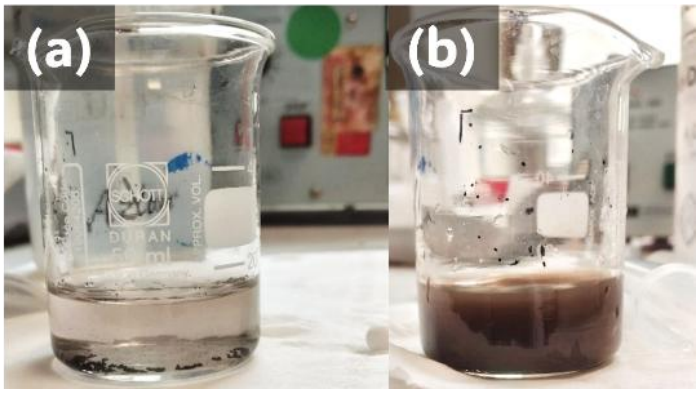

Figure 7.9: *(a) Before Sonication and (b) After sonication*

7.3.5 Proposed mechanism of dye degradation

Metastable white cast iron has a distinct microstructure, allowing it to catalyze a range of chemical processes, including oxidation. Its magnetic features improve electron transport processes, making it more reactive in moist or hot environments. The dye degradation process using white cast iron may be described in the following phases [37].

- **Electron Transfer**

The surface of WCI-P facilitates the transfer of electrons from the dye molecules to oxygen or other oxidants present in the system. This process generates free radicals, which play a critical role in breaking down the dye molecules into smaller, less harmful components.

- **Nucleophilic Attack**

Sulfonic Group Reactivity: The sulfonic groups in the dye structure can become reactive targets for nucleophilic attacks, especially when activated by reactive species generated during oxidation.

Formation of Sulfonate Radicals: These sulfonic groups can produce sulfonate radicals, which can either interact with other dye components or decompose into simpler molecules, contributing to the overall degradation of the dye.

- **Azo Bond Cleavage**

Radicals generated during the reaction can destabilize and cleave the azo bond (N=N), initiating its decomposition. The resulting fragments, being highly reactive intermediates, may undergo further degradation, ultimately breaking down into simpler, less complex molecules [38].

- **Hydrolysis**

Hydrolysis may occur in the presence of water, particularly in acidic or basic conditions, facilitating the breakdown of the dye into simpler compounds. In summary, the degradation of azo dyes containing sulfonic groups by metastable white cast iron primarily involves electron transfer, the generation of radicals, and subsequent chemical reactions that break down the dye structure. The distinctive properties of white cast iron, such as its reactive microstructure and efficient electron transfer capability, enhance its effectiveness in destabilizing dye molecules, making them more susceptible to complete degradation.

A comparative analysis was conducted to assess the efficiency of WCI-P to other materials studied in prior research, with a focus on reaction conditions and degradation performance, as summarized in Table 7.3. For example, Shein Z.Z et al., [39] investigated the degradation of basic green dye using cast iron combined with ultrasonic radiation. Their findings revealed that 10 g of cast iron at an acidic pH successfully degraded 95% of the dye solution within 10 minutes. In related studies on the degradation of orange II dye, similar methodologies have been explored to enhance degradation efficiency. Kumar et al. [40] compared the performance of cast iron particles with pure elemental iron in degrading 100 mg/L of Orange II dye. Their study showed that 28.56 g/L of cast iron filings reduced the dye within 60 minutes, achieving

over 99% decomposition. Cast iron particles demonstrated significantly higher degradation efficiency compared to pure elemental iron.

This study presents the development of a cost-effective white cast iron powder capable of efficiently degrading RR 195A, a commonly used textile dye. Notably, without lowering the pH to 3, which is typically an important factor in enhancing degradation, we achieved a 94.5% degradation rate in only 15 minutes at neutral pH using a 0.01 g/L dye solution. This efficient degradation was accomplished without the need to reduce the pH further.

Table 7.3: *Comparison of dye degradation using various zero-valent iron materials and dyes.*

Sr. #	**Type of ZVI**	**Dye**	**Shape/Size (mm)**	**Dosage (g)**	**Conc. of Dye (mg/L)**	**pH**	**Temp.**	**Time (min)**	**Deg. (%)**	**Ref.**
1	Cast Iron	2,4-DNT	Scrap/ 7	---	40	7	25	120	80	[17]
2	Cast iron	ClO^{-4}	----	50	20 – 60	7.4	20 ± 1	30 - 80	98	[18]
3	Cast iron	BG	Scrap iron/----	10-30	369.7 – 778.62	3.2-6.8	-----	10	≥ 95	[39]
4	Micron Sized Cast Iron	OII	Filling/----	28.56	50 – 500	3 - 7	25	60	≥ 99	[40]
5	Cast Iron	AR14	0.2 – 0.9	1 – 5	50 – 250	2 - 8	25	10	≤ 92	[41]
6	WCI-P ($Fe_{82}C_{15}Si_3$)	RR 195 A	0.036	0.1	10 - 50	7	25	15	≤ 95	This work

AR14: Acid Red 15, BG: Basic Green, OII: Orange II, RR195A: Reactive Red 195A, 2,4-DNT : 2,4 dinitro-toluene. Deg. Degradation rate, ClO^{-4}*: perchlorate*

In conclusion, the results on the effects of temperature, reactive red 195A dye concentration, and degraded solution concentration, as shown in Fig. 7.10, confirm that WCI-P exhibits outstanding stability over time. These findings underscore its significant potential for applications in continuous degradation processes.

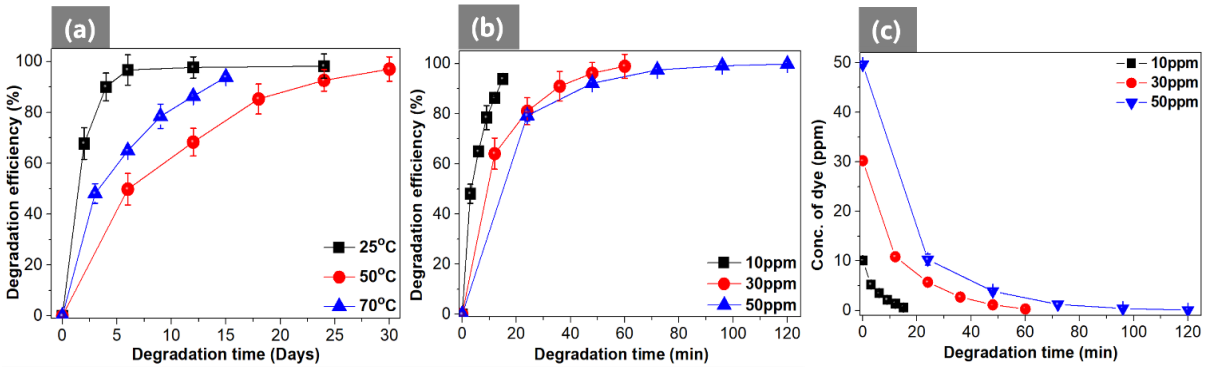

***Figure 7.10**: Effects on degradation efficiency: (a) Temperature, (b) Concentration, (c) Degraded solution.*

7.4 Conclusion

This study demonstrates that WCI-P can successfully produce an efficient and cost-effective catalyst. Throughout the study, it was referred to as WCI-P. This catalyst is created by ball-milling $Fe_{82}C_{15}Si_3$ ribbons, and demonstrates exceptional efficiency in degrading organic dyes, attributed to its metastable properties and large surface area. Its straightforward and fast synthesis process further enhances its suitability for practical applications. Our findings on the effects of temperature and dye concentration show that reactive red 195A can be completely degraded within 12 to 15 min. at 70 °C, requiring only 0.1 g of WCI-P. A degradation efficiency of 99.9% was achieved at a dye concentration of 0.1 ppm with extended reaction time and temperature. The WCI-P catalyst also displays excellent reusability and possesses a unique electronic structure that provides additional free electrons, enhancing adsorption capabilities. Its potential for rapid and efficient azo-dye degradation underscores its significance in sustainable catalysis. This innovative and economical approach to iron-based catalysts demonstrates markedly improved catalytic performance in azo dye degradation, offering a promising pathway for environmentally sustainable and effective wastewater treatment and environmental remediation solutions.

Reference

1. Abdipour, H.; Hemati, H. Sonocatalytic Process of Penicillin Removal Using-Fe2O3/Effect of Different Parameters/Degradation Mechanism/Kinetic Study/Optimisation with Response Surface Model. *Int J Environ Anal Chem* **2023**, 1–22.

2. Deng, F.; Brillas, E. Advances in the Decontamination of Wastewaters with Synthetic Organic Dyes by Electrochemical Fenton-Based Processes. *Sep Purif Technol* **2023**, 123764.

3. Kamani, H.; Hosseinzehi, M.; Ghayebzadeh, M.; Azari, A.; Ashrafi, S.D.; Abdipour, H. Degradation of Reactive Red 198 Dye from Aqueous Solutions by Combined Technology Advanced Sonofenton with Zero Valent Iron: Characteristics/Effect of Parameters/Kinetic Studies. *Heliyon* **2024**, *10*.

4. Ahmadi, A.; Hajilou, M.; Zavari, S.; Yaghmaei, S. A Comparative Review on Adsorption and Photocatalytic Degradation of Classified Dyes with Metal/Non-Metal-Based Modification of Graphitic Carbon Nitride Nanocomposites: Synthesis, Mechanism, and Affecting Parameters. *J Clean Prod* **2023**, *382*, 134967.

5. Kansal, S.K.; Kaur, N.; Singh, S. Photocatalytic Degradation of Two Commercial Reactive Dyes in Aqueous Phase Using Nanophotocatalysts. *Nanoscale Res Lett* **2009**, *4*, 709–716.

6. Lv, Z.; Yan, Y.; Yuan, C.; Huang, B.; Yang, C.; Ma, J.; Wang, J.; Huo, L.; Cui, Z.; Wang, X. Making Fe-Si-B Amorphous Powders as an Effective Catalyst for Dye Degradation by High-Energy Ultrasonic Vibration. *Mater Des* **2020**, *194*, 108876.

7. Miao, J.; Jia, Z.; Lu, H.-B.; Habibi, D.; Zhang, L.-C. Heterogeneous Photocatalytic Degradation of Mordant Black 11 with ZnO Nanoparticles under UV–Vis Light. *J Taiwan Inst Chem Eng* **2014**, *45*, 1636–1641.

8. Kalme, S.D.; Parshetti, G.K.; Jadhav, S.U.; Govindwar, S.P. Biodegradation of Benzidine Based Dye Direct Blue-6 by Pseudomonas Desmolyticum NCIM 2112. *Bioresour Technol* **2007**, *98*, 1405–1410.

9. Supaka, N.; Juntongjin, K.; Damronglerd, S.; Delia, M.-L.; Strehaiano, P. Microbial Decolorization of Reactive Azo Dyes in a Sequential Anaerobic–Aerobic System. *Chemical Engineering Journal* **2004**, *99*, 169–176.

10. Weng, C.-H.; Lin, Y.-T.; Yuan, H.-M. Rapid Decoloration of Reactive Black 5 by an Advanced Fenton Process in Conjunction with Ultrasound. *Sep Purif Technol* **2013**, *117*, 75–82.

11. Zhang, H.; Feng, Y.; Cheng, Y.; Baró, M.D.; Altube, A.; García-Lecina, E.; Alcaide, F.; Pellicer, E.; Zhang, T.; Sort, J. Nanoporous Fe-Based Alloy Prepared by Selective Dissolution: An Effective Fenton Catalyst for Water Remediation. *ACS Omega* **2017**, *2*, 653–662.

12. Hou, M.; Li, F.; Liu, X.; Wang, X.; Wan, H. The Effect of Substituent Groups on the Reductive Degradation of Azo Dyes by Zerovalent Iron. *J Hazard Mater* **2007**, *145*, 305–314.

13. Barreto-Rodrigues, M.; Silveira, J.; Zazo, J.A.; Rodriguez, J.J. Synthesis, Characterization and Application of Nanoscale Zero-Valent Iron in the Degradation of the Azo Dye Disperse Red 1. *J Environ Chem Eng* **2017**, *5*, 628–634.

14. Zhang, C.; Zhu, Z.; Zhang, H.; Hu, Z. Rapid Decolorization of Acid Orange II Aqueous Solution by Amorphous Zero-Valent Iron. *Journal of Environmental Sciences* **2012**, *24*, 1021–1026.

15. He, Y.; Gao, J.-F.; Feng, F.-Q.; Liu, C.; Peng, Y.-Z.; Wang, S.-Y. The Comparative Study on the Rapid Decolorization of Azo, Anthraquinone and Triphenylmethane Dyes by Zero-Valent Iron. *Chemical Engineering Journal* **2012**, *179*, 8–18.

16. Wanner, C.; Eggenberger, U.; Mäder, U. Reactive Transport Modelling of Cr (VI) Treatment by Cast Iron under Fast Flow Conditions. *Applied geochemistry* **2011**, *26*, 1513–1523.

17. Fan, J.; Wang, H.; Wu, D.; Liu, Z.; Ma, L. Scrap Cast Iron and Copper-modified Cast Iron for Reductive Degradation of 2, 4-dinitrotoluene. *Journal of Chemical Technology & Biotechnology* **2011**, *86*, 1295–1302.

18. Oh, S.-Y.; Chiu, P.C.; Kim, B.J.; Cha, D.K. Enhanced Reduction of Perchlorate by Elemental Iron at Elevated Temperatures. *J Hazard Mater* **2006**, *129*, 304–307.

19. Wang, P.; Wang, J.; Huo, J.; Xu, W.; Wang, X.; Wang, G. Fast Degradation of Azo Dye by Nanocrystallized Fe-Based Alloys. *Sci China Phys Mech Astron* **2017**, *60*, 1–5.

20. Chen, S.; Yang, G.; Luo, S.; Yin, S.; Jia, J.; Li, Z.; Gao, S.; Shao, Y.; Yao, K. Unexpected High Performance of Fe-Based Nanocrystallized Ribbons for Azo Dye Decomposition. *J Mater Chem A Mater* **2017**, *5*, 14230–14240.

21. Liang, S.; Jia, Z.; Liu, Y.; Zhang, W.; Wang, W.; Lu, J.; Zhang, L. Compelling Rejuvenated Catalytic Performance in Metallic Glasses. *Advanced Materials* **2018**, *30*, 1802764.

22. Scaglione, F.; Battezzati, L. Metastable Microstructures Containing Zero Valent Iron for Fast Degradation of Azo Dyes. *J Mater Sci* **2015**, *50*, 5238–5243, doi:10.1007/s10853-015-9071-4.

23. Xue, Y.; Scaglione, F.; Rizzi, P.; Battezzati, L.; Denis, P.; Fecht, H.-J. Electrodeposited Platinum on De-Alloyed Nanoporous Gold with Enhanced Electro-Catalytic Performance. *Appl Surf Sci* **2019**, *476*, 412–417.

24. Xie, Y.; Xie, S.; Yang, H.; Deng, Y.; Qian, H.; Zeng, X. A Dramatically Improved Degradation Efficiency of Azo Dyes by Zero Valent Iron Powders Decorated with In-Situ Grown Nanoscale Fe2B. *J Alloys Compd* **2020**, *842*, 155818.

25. Zhang, C.; Zhu, Z.; Zhang, H.; Hu, Z. Rapid Decolorization of Acid Orange II Aqueous Solution by Amorphous Zero-Valent Iron. *Journal of Environmental Sciences* **2012**, *24*, 1021–1026.

26. Chen, S.; Yang, G.; Luo, S.; Yin, S.; Jia, J.; Li, Z.; Gao, S.; Shao, Y.; Yao, K. Unexpected High Performance of Fe-Based Nanocrystallized Ribbons for Azo Dye Decomposition. *J Mater Chem A Mater* **2017**, *5*, 14230–14240.

27. Zhang, C.; Zhu, Z.; Zhang, H.; Hu, Z. On the Decolorization Property of Fe–Mo–Si–B Alloys with Different Structures. *J Non Cryst Solids* **2012**, *358*, 61–64.

28. Dizge, N.; Aydiner, C.; Demirbas, E.; Kobya, M.; Kara, S. Adsorption of Reactive Dyes from Aqueous Solutions by Fly Ash: Kinetic and Equilibrium Studies. *J Hazard Mater* **2008**, *150*, 737–746.

29. Fan, J.; Guo, Y.; Wang, J.; Fan, M. Rapid Decolorization of Azo Dye Methyl Orange in Aqueous Solution by Nanoscale Zerovalent Iron Particles. *J Hazard Mater* **2009**, *166*, 904–910.

30. Wang, J.-Q.; Liu, Y.-H.; Chen, M.-W.; Louzguine-Luzgin, D. V; Inoue, A.; Perepezko, J.H. Excellent Capability in Degrading Azo Dyes by MgZn-Based Metallic Glass Powders. *Sci Rep* **2012**, *2*, 418.

31. Khorramfar, S.; Mahmoodi, N.M.; Arami, M.; Gharanjig, K. Dye Removal from Colored Textile Wastewater Using Tamarindus Indica Hull: Adsorption Isotherm and Kinetics Study. *Journal of Color Science and Technology* **2009**, *3*, 81–88.

32. Natarajan, T.S.; Natarajan, K.; Bajaj, H.C.; Tayade, R.J. Enhanced Photocatalytic Activity of Bismuth-Doped TiO2 Nanotubes under Direct Sunlight Irradiation for Degradation of Rhodamine B Dye. *Journal of nanoparticle research* **2013**, *15*, 1669.

33. Zhang, C.; Sun, Q.; Liu, K. From Adsorption to Reductive Degradation: Different Decolorization Properties of Metallic Glasses Based on Different Iron-Group Elements. *J Alloys Compd* **2018**, *741*, 1040–1047.

34. Zhang, C.; Zhang, H.; Lv, M.; Hu, Z. Decolorization of Azo Dye Solution by Fe–Mo–Si–B Amorphous Alloy. *J Non Cryst Solids* **2010**, *356*, 1703–1706.

35. Pielesz, A.; Baranowska, I.; Rybak, A.; Włochowicz, A. Detection and Determination of Aromatic Amines as Products of Reductive Splitting from Selected Azo Dyes. *Ecotoxicol Environ Saf* **2002**, *53*, 42–47.

36. Samarghandi, M.R.; Zarrabi, M.; Amrane, A.; Sepehr, M.N.; Noroozi, M.; Namdari, S.; Zarei, A. Kinetic of Degradation of Two Azo Dyes from Aqueous Solutions by Zero Iron Powder: Determination of the Optimal Conditions. *Desalination Water Treat* **2012**, *40*, 137–143.

37. Selvaraj, V.; Karthika, T.S.; Mansiya, C.; Alagar, M. An over Review on Recently Developed Techniques, Mechanisms and Intermediate Involved in the Advanced Azo Dye Degradation for Industrial Applications. *J Mol Struct* **2021**, *1224*, 129195.

38. Kamenická, B. Chemical Degradation of Azo Dyes Using Different Reducing Agents: A Review. *Journal of Water Process Engineering* **2024**, *61*, 105350.

39. Shen, Z.; Shen, J. The Use of Ultrasound to Enhance the Degradation of the Basic Green by Cast Iron. *Ultrasonics* **2006**, *44*, e353–e356.

40. Kumar, R.; Sinha, A. *DEGRADATION OF MONO-AZO DYE IN AQUEOUS SOLUTION USING CAST IRON FILINGS*;

41. Lin, J. jie; Zhao, X. song; Liu, D.; Yu, Z. guo; Zhang, Y.; Xu, H. The Decoloration and Mineralization of Azo Dye C.I. Acid Red 14 by Sonochemical Process: Rate Improvement via Fenton's Reactions. *J Hazard Mater* **2008**, *157*, 541–546, doi:10.1016/j.jhazmat.2008.01.050.

CHAPTER VIII

Final Remarks: Achievements and Pathways Ahead

This research introduces an innovative approach to fabricating nanostructured metals, focusing on their roles in environmental remediation and sensing technologies. Each chapter highlights a specific material, examining its fabrication, optimization, applications, and advancements in sensing and degradation methods. The main objective is to develop cost-effective, sustainable solutions for detecting and degrading harmful dyes like malachite green isothiocyanate, methylene blue, and reactive red 195A. This was achieved by investigating nanoporous gold (NPG), nanoporous copper (np-Cu), and white cast iron powder (WCI-P).

8.1 Synthesis of Nanoporous Gold (NPG)

This study outlines a simple, effective chemical dealloying method for producing ultrafine NPG using L-cysteine. The study demonstrates the significant influence of L-cysteine concentration on the structural morphology of NPG derived from an amorphous $Au_{20}Cu_{48}Ag_7Pd_5Si_{20}$ ribbon synthesized via arc melting. From the study, it was indicated that lowering the concentrations of L-cysteine, i.e., 0.2 mM, 0.4 mM, and 0.6 mM, facilitated the formation of well-defined interconnected ligaments and pores, while higher concentrations ranging from 4 mM, 8 mM, and 16 mM led to surface defects that hinder the desired nanoporous structure. Notably, the cleaning process to eliminate residual L-cysteine was ineffective, indicating that high concentrations may cause irreversible alterations in the NPG's morphology and catalytic properties. The optimal concentrations for achieving ultrafine NPG structures with ultra-fine structures are between 0.2 mM and 0.6 mM, as demonstrated by reduced ligament sizes and enhanced structural integrity. EDS and XRD analyses further confirm effective dealloying and crystallization, underscoring the importance of concentration optimization in synthesizing NPG for various applications. This method is cost-effective and compatible with large-scale production, paving the way for high-performance nanoporous metal frameworks. In another study, NPG was synthesized using a longer dealloying time of 5 hours to assess its effect on structural optimization. This extended dealloying process further improved the NPG's surface area with an average ligament size of 65.0 ± 7.5 nm, exhibited exceptional SERS performance due to the abundance of active sites on its surface, facilitated by nanosized pores and ligaments. An enhancement factor of 7.9 × 109 and a detection limit of 10-16 M were achieved that successfully meeting the EU standards for detecting toxic contaminants. These findings indicate that the NPG-5h substrate, which serves as an active SERS substrate, provides a simple, rapid, and versatile approach to identifying MGITC. This provides a pathway for the ultrasensitive detection of toxic effluents.

8.1.1 Future Implications

In the case of NPG, future research may focus on developing other surfactants or additives to replace L-cysteine, which might be helpful in changing the surface morphology of NPG. Furthermore, introducing NPG into portable devices may broaden its uses in environmental monitoring.

8.2 Synthesis of Nanoporous Copper (np-Cu/ NPC-films)

Using the NPG-5h as an active SERS substrate and producing the NPG surface morphology, we turned our focus to copper, which is a more readily available and cost-effective alternative to gold. We used a chemical dealloying process to produce porous copper from a commercial brass bar. In this work, different parameters were investigated to maximize pore morphology and achieve a porous structure, including hydrochloric acid concentration, reaction duration, and temperature. Our findings demonstrated that increasing the concentration of HCl and extending the dealloying time resulted in homogeneous, linked structures. Along this, three-dimensional porous copper films were also fabricated using dynamic hydrogen bubbling technology (DHBT). The addition of cetyltrimethylammonium bromide as a surfactant effectively stabilized the hydrogen bubbles, enhancing pore uniformity and resulting in smaller, more consistent structures. The copper films produced through this method demonstrated impressive surface-enhanced Raman scattering (SERS) performance, successfully detecting methylene blue at a concentration of 10^{-6} M. These findings highlight the potential of DHBT for producing porous copper films that can be applied in environmental sensing and other fields.

8.2.1 Future Implications

To further improve the sensitivity of nanoporous copper, future work may be concentrated on exploring different approaches or using different electrolytes. Different alloys that contain copper and other metals may be employed, followed by dealloying to modify the surface feature of nanoporous copper. These methods will help in accelerating the catalytic properties of nanoporous copper. Additionally, there is an opportunity to find alternative surfactants that could improve performance. The DHBT method can be applied to industrial production. Beyond dye detection, porous copper films can be applied in electrocatalysis, energy storage, and other fields.

8.3 Synthesis and Application of White Cast Iron Powder (WCI-P)

In addition to synthesizing NPG and Cu, we also synthesized white cast iron powder (WCI-P) from metastable iron ribbons using the ball milling method. This process resulted in WCI-P with a high surface area and unique metastable properties, which effectively degraded Reactive Red 195A dye. Remarkably, complete degradation was achieved within just 15 minutes at a temperature of 70 °C. We assessed the stability and effectiveness of WCI-P through reusability tests, which demonstrated its reliable performance over seven cycles.

8.3.1 Future Directions

To enhance the catalytic efficiency and broaden the applications of WCI-P, future studies will concentrate on modifying its surface and structural properties. Various materials, including pharmaceuticals and heavy metals, can be used for degradation alongside dye molecules

From the overall finding, this thesis is based on different fabrication methods aimed at modifying the structural morphology of nanostructured metals for dye detection and degradation. The findings establish sustainable solutions for environmental monitoring. However, challenges related to sensitivity and stability remain. Future research should concentrate on broadening the applications of these materials and investigating their potential uses in catalysis, energy storage, and biomedical applications.